

**APPLICATION OF MAGNETIC HYSTERESIS MODELING TO THE DESIGN  
AND ANALYSIS OF ELECTRICAL MACHINES**

Maged Ibrahim

A Thesis

In the Department

of

Electrical and Computer Engineering

Presented in Partial Fulfillment of the Requirements

for the Degree of

Doctor of Philosophy (Electrical and Computer Engineering) at

Concordia University

Montreal, Quebec, Canada

November 2014

© Maged Ibrahim, 2014

**CONCORDIA UNIVERSITY**  
**SCHOOL OF GRADUATE STUDIES**

This is to certify that the thesis prepared

By: Maged Ibrahim

Entitled: Application of Magnetic Hysteresis Modeling to the Design and Analysis of Electrical Machines

and submitted in partial fulfillment of the requirements for the degree of

Doctor of Philosophy (Electrical and Computer Engineering)

complies with the regulations of the University and meets the accepted standards with respect to originality and quality.

Signed by the final examining committee:

_____	Chair
Dr. R. Ganesan	
_____	External Examiner
Dr. J. O. Ojo	
_____	External to Program
Dr. R. Sedaghati	
_____	Examiner
Dr. A. Sebak	
_____	Examiner
Dr. L. A. C. Lopes	
_____	Thesis Supervisor
Dr. P. Pillay	

Approved by

\_\_\_\_\_

Dr. A. Sebak, Graduate Program Director

November 25, 2014

\_\_\_\_\_

Dr. A. Asif, Dean  
Faculty of Engineering and Computer Science

# ABSTRACT

Application of Magnetic Hysteresis Modeling to the Design and Analysis of Electrical Machines

Maged Ibrahim, Ph.D.

Concordia University, 2014

Permanent magnet synchronous machines (PMSMs) with rare-earth magnets are widely used in the traction drives of electrical and hybrid electrical vehicles, as they can provide high efficiency and torque density. Due to the possibility of future shortage of rare-earth materials, it is essential for electric vehicle industry to find alternative magnet technologies that can provide a substitute for rare-earth PMSMs. Permanent magnet machines with Alnico magnets can theoretically provide torque densities comparable to rare-earth PMSMs, due to their high remnant flux density. However, these magnets are rarely used in the conventional designs of PMSMs, as they can be demagnetized by the armature field.

The thesis presents a novel design for permanent magnet machines with Alnico magnets. The proposed design can provide high air gap flux density at no-load, and the armature field at full load tends to enhance the magnet flux. Therefore, the machine can operate with high torque density even under severe loading conditions. The demagnetization characteristics of Alnico magnets are also utilized to achieve high efficiency at a wide speed range, as the magnet flux is reduced at high speeds by armature current pulses that

dissipate negligible losses, thus avoiding the additional copper losses of the continuous flux weakening current in conventional rare-earth PMSMs.

The simulation of the demagnetization and magnetization dynamics of the proposed machine design requires considering the hysteresis characteristics of the permanent magnets. Therefore, finite element analysis (FEA) simulations for the designed machine are performed using a linearized hysteresis model for Alnico magnets. The thesis also aims to improve the design and modeling of electrical machines by developing computationally efficient methods for incorporating the hysteresis characteristics of electrical steel into electrical machine models.

## **ACKNOWLEDGMENTS**

I would like to express my deep appreciation to my supervisor Dr. Pragasen Pillay for his invaluable guidance and continuous support throughout my MA.Sc and Ph.D studies. I am really grateful to work with such a visionary professor and such a caring person.

Many thanks to all of the other professors and colleagues in the Power Electronics and Energy Research (PEER) group for their help and insightful discussions.

I also would like to express my deepest gratitude to my parents for their unconditional support throughout my whole life.

My sincere gratitude extends to my beloved fiancée, Rodaina El-Sarraf, for her emotional support and continuous encouragement.

# TABLE OF CONTENTS

List of Figures.....	x
List of Tables .....	xx
Nomenclature.....	xx
List of Symbols.....	xxiii
1. Introduction.....	1
1.1 Background.....	1
1.2 Objective.....	3
1.3 Thesis Outline.....	4
2. Hysteresis of Magnetic Materials .....	5
2.1 Introduction .....	5
2.2 Modeling of Magnetic Materials .....	7
2.2.1 Hard Magnetic Materials.....	7
2.2.2 Soft Magnetic Materials .....	12
3. Design of Variable Flux Permanent Magnet Machine Using Alnico Magnets .....	14

3.1	Review of Variable Flux Machines .....	14
3.2	Analytical Machine Design.....	17
3.2.1	Magnet Orientation.....	17
3.2.2	Magnet Type.....	18
3.2.3	Magnet Dimensions.....	20
3.3	Finite Element Based Machine Design .....	21
3.3.1	Hysteresis Based Finite Element Stimulation.....	22
3.3.2	Number of Poles.....	29
3.3.3	Stator Design.....	31
3.3.4	Rotor Design.....	44
3.4	Analysis of the Machine Performance.....	57
3.4.1	Torque-Speed Characteristics .....	57
3.4.2	Efficiency Analysis .....	62
3.5	Experimental Validation .....	71
3.6	Summary.....	75

4.	Hysteresis Loss Prediction In Electrical Machines .....	76
4.1	Introduction .....	76
4.2	Hysteresis Loss Measurement .....	77
4.3	Hysteresis Loss Modeling .....	81
4.3.1	Analytical Model .....	81
4.3.2	Energetic Model .....	85
4.3.3	Hybrid Model .....	92
4.4	Prediction of Hysteresis Loss in Switched Reluctance Machines .....	95
4.5	Summary .....	102
5.	Hysteresis Dependent Model for the Brushless Exciter of Synchronous Generators.....	103
5.1	Introduction .....	103
5.2	Hysteresis Effect on the Brushless Exciter Transient Response .....	105
5.3	Hysteretic Model .....	107
5.4	Identification of the Hysteretic Model Parameters .....	108
5.5	Brushless Exciter Model .....	113

5.6	Measurements of the Exciter Parameters.....	117
5.7	Experimental Validation.....	121
5.8	Summary.....	124
6.	Conclusions and Recommendations.....	125
6.1	Conclusions.....	125
6.2	Proposed Future Research.....	128
6.3	Contributions.....	129
	References.....	131

## LIST OF FIGURES

Fig. 2.1 Random domain orientation of a ferromagnetic material.....	5
Fig. 2.2 Typical hysteresis loop of a soft magnetic material. ....	6
Fig. 2.3 Electric equivalent circuit of a permanent magnet . ....	8
Fig. 2.4 Illustration of a permanent magnet flux paths.....	8
Fig. 2.5 Graphical representation of the magnet operation with an external magnetic field .....	9
Fig. 2.6 Illustration of irreversible magnet demagnetization.....	11
Fig. 2.7 Linearized hysteresis model for Alnico magnets. ....	12
Fig. 3.1 Variable flux memory motor [24]. ....	15
Fig. 3.2 Radial variable flux machine with inverted saliency [30].....	17
Fig. 3.3 Illustration of $d$ and $q$ axes flux paths in tangentially magnetized PMSM.....	18
Fig. 3.4 Demagnetization curves of different Alnico grades showing the magnet operating points at no load . ....	19
Fig. 3.5 Key dimensions of tangentially magnetized PMSM rotor . ....	21
Fig. 3.6 Cross section of the preliminary 4-pole rotor design. ....	22

Fig. 3.7 Flux density distribution when the magnet is aligned with a slot at no load .....	24
Fig. 3.8 Flux density distribution when the magnet is aligned with a tooth at no load. ..	24
Fig. 3.9 Illustration of the variation of magnet operating point due to stator slotting ....	25
Fig. 3.10 Effect of irreversible demagnetization on the simulated magnet flux density at full load .....	26
Fig. 3.11 Simulated waveforms in FEA when a demagnetizing pulse is applied.....	27
Fig. 3.12 Simulated back EMF after releasing demagnetization current pulses of different magnitudes.....	28
Fig. 3.13 Cross section of the 6-pole rotor design.....	30
Fig. 3.14 Cross section of the 8-pole rotor design.....	30
Fig. 3.15 Flux distribution of the 18-slot design during magnetization.....	33
Fig. 3.16 Flux distribution of the 36-slot design during magnetization.....	33
Fig. 3.17 Comparison of the simulated output torque of the 18-slot and 36-slot machines. ....	34
Fig. 3.18 Comparison of the simulated output torque of the skewed and un-skewed 18-slot machines.....	35
Fig. 3.19 Simulated flux distribution at the front edge of the skewed machine. ....	36

Fig. 3.20 Simulated flux distribution at the rear edge.of the skewed machine.....	37
Fig. 3.21 Simulated magnet flux density for the skewed machine at different parts of the machine axial length. ....	37
Fig. 3.22 Simulated magnet flux density for the 6-pole 9-slot machine at full load ... ..	39
Fig. 3.23 Simulated full magnetization current for machines with different tooth width .....	42
Fig. 3.24 Simulated full magnetization current for machines with different yoke width .....	42
Fig. 3.25 Simulated magnetization current for machines with different teeth to yoke ratio .....	43
Fig. 3.26 Simulated back EMF for the 27-slots machine with the preliminary rotor design .....	44
Fig. 3.27 Illustration of pole arc reduction in tangentially magnetized PMSM. ....	45
Fig. 3.28 Effect of the effective pole arc angle on the back EMF waveform.....	47
Fig. 3.29 Effect of the effective pole arc angle on the back EMF harmonics. ....	47
Fig. 3.30 Illustration of the uneven air gap design. ....	48

Fig. 3.31 Comparison of the simulated air gap flux density for a rotor with uniform air gap and a rotor with $\Delta L_g = 0.35 \text{ mm}$ .....	49
Fig. 3.32 Rotor design with additional barriers. ....	50
Fig. 3.33 Proposed modified rotor design.....	51
Fig. 3.34 Comparison of the simulated back EMF for the initial and modified rotor designs .....	52
Fig. 3.35 Magnetization characteristics for machines with different magnet thickness...53	
Fig. 3.36 Simulated full magnetization current and output torque for machines designed with different magnet lengths . ....	54
Fig. 3.37 Rotor stress distribution at 10,000 rpm . ....	55
Fig. 3.38 Maximum stress in the rotor as a function of speed .....	55
Fig. 3.39 Scaled rotor deformation at 10,000 rpm (scale = 1:100) .....	56
Fig. 3.40 Maximum displacement in the rotor as a function of speed .....	56
Fig. 3.41 Torque-speed curves for different magnetization levels . ....	60
Fig. 3.42 Variation of voltage components with the magnetization level .....	60

Fig. 3.43 Simulated power-speed curves for different magnetization levels.....	61
Fig. 3.44 Simulated armature currents for different magnetization levels .....	61
Fig. 3.45 Efficiency map at 100% magnetization .....	63
Fig. 3.46 Efficiency map at 75% magnetization.....	63
Fig. 3.47 Efficiency map at 50% magnetization.....	64
Fig. 3.48 Efficiency map at 25% magnetization.....	64
Fig. 3.49 Total machine loss distribution at 100% magnetization .....	65
Fig. 3.50 Total machine loss distribution at 75% magnetization.....	65
Fig. 3.51 Total machine loss distribution at 50% magnetization.....	66
Fig. 3.52 Total machine loss distribution at 25% magnetization.....	66
Fig. 3.53 Iron loss distribution at 100% magnetization .....	67
Fig. 3.54 Iron loss distribution at 75% magnetization .....	67
Fig. 3.55 Iron loss distribution at 50% magnetization .....	68
Fig. 3.56 Iron loss distribution at 25% magnetization .....	68

Fig. 3.57 Distribution of the optimum magnetization level.....	69
Fig. 3.58 Efficiency map when the optimum magnetization level is used. ....	70
Fig. 3.59 Improvement in the machine efficiency at low torque when the optimum magnetization level is used.....	70
Fig. 3.60 Machine prototyping.....	71
Fig. 3.61 Measured machine flux linkage after applying magnetizing current pulses ...	72
Fig. 3.62 Comparison of measured and simulated back EMF at 1000 rpm.....	73
Fig. 3.63 Comparison of measured and simulated output torque at different torque angles .....	74
Fig. 3.64 Comparison of measured and simulated flux linkage after applying demagnetizing current pulses.....	75
Fig. 4.1 Measured major and minor hysteresis loops. ....	78
Fig. 4.2 The required flux density waveform to generate a certain minor loop. ....	80
Fig. 4.3 Test system schematic diagram. ....	80
Fig. 4.4 Comparison between measured symmetric major loop hysteresis energy losses with the losses calculated by equation (4.2). ....	82

Fig. 4.5 Comparison between measured minor loop losses at different positions with the losses calculated by equation (4.3) for $B_p = 1.4$ T. ....	84
Fig. 4.6 Errors in the minor loop hysteresis loss calculation using equation (4.3) for $B_p = 1.2$ T. ....	84
Fig. 4.7 Errors in the minor loop hysteresis loss calculation using equation (4.3) for $B_p = 1.6$ T. ....	85
Fig. 4.8 Comparison of measured and simulated loops for $\Delta B = 0.4B_p$ , $B_o = B_p$ and $B_p = 1.4$ T. ....	89
Fig. 4.9 Comparison of measured and simulated loops for $\Delta B = B_p$ , $B_o = B_p$ and $B_p = 1.4$ T. ....	90
Fig. 4.10 Comparison of measured and simulated loops for $\Delta B = 0.2B_p$ , $B_o = 0.4B_p$ and $B_p = 1.4$ T. ....	90
Fig. 4.11 Comparison of measured and simulated loops for $\Delta B = 0.4B_p$ , $B_o = B_p$ and $B_p = 1.6$ T. ....	91
Fig. 4.12 Errors in the minor loop hysteresis losses calculation using the Energetic model for $B_p = 1.2$ T. ....	91

Fig. 4.13 Errors in the minor loop hysteresis loss calculation using the Energetic model for $B_p = 1.6$ T.....	92
Fig. 4.14 Comparison of the errors of symmetric major hysteresis loop calculation by the energetic model and the modified Steinmtz equation.....	93
Fig. 4.15 Hybrid model flow chart.....	94
Fig. 4.16 Comparison of the errors of the Energetic model and the modified Steinmetz equation for different DC components. ....	95
Fig. 4.17 Cross section of the simulated 6/4 SRM .....	96
Fig. 4.18 Simulated flux density waveform in the stator pole of the SRM .....	96
Fig. 4.19 Simulated flux density waveform in the stator core of the SRM .....	97
Fig. 4.20 Simulated flux density waveform in the rotor pole of the SRM .....	97
Fig. 4.21 Simulated flux density waveform in the rotor core of the SRM .....	98
Fig. 4.22 Simulated hysteresis loop in the stator pole of the SRM.....	98
Fig. 4.23 Simulated hysteresis loop in the stator yoke of the SRM.....	99
Fig. 4.24 Simulated hysteresis loop in the rotor pole of the SRM.....	99
Fig. 4.25 Simulated hysteresis loop in the rotor core of the SRM.....	100

Fig. 4.26 Spatial distribution of different calculation techniques used by the hybrid model.....	101
Fig. 5.1 Schematic diagram of a brushless synchronous generator system.....	103
Fig. 5.2 Simplified construction of a 2-pole brushless exciter. ....	105
Fig. 5.3 Illustration of the exciter flux linkage variation during transient.....	106
Fig. 5.4 Illustration of magnetization flux linkage - current loops during transient.....	106
Fig. 5.5 Simplified machine magnetic equivalent circuit. ....	108
Fig. 5.6 Flux linkage-current characteristics for the steel and air gap.....	109
Fig. 5.7 Typical magnetization flux linkage-current loop. ....	110
Fig. 5.8 Modified magnetic equivalent circuit at remnance. ....	111
Fig. 5.9 Illustration of the steel operating point at zero current.....	112
Fig. 5.10 Brushless exciter $dq$ -axes model .....	114
Fig. 5.11 Implementation of the hysteretic magnetization branch.....	114
Fig. 5.12 Implementation of the brushless exciter model.....	115
Fig. 5.13 Comparison of the flux linkage - current loops measured from the stator and rotor sides with a turns-ratio of 0.02.....	118

Fig. 5.14 Comparison of the measured and simulated flux linkage -current loops .....	120
Fig. 5.15 Measured exciter field current after a step change in the excitation voltage ..	121
Fig. 5.16 Simulated exciter field current after a step change in the excitation voltage ..	122
Fig. 5.17 Comparison of the measured and simulated generator output voltage after a step change in the excitation voltage.....	123
Fig. 5.18 Simulated flux linkage-current trajectory during transient.....	123

## LIST OF TABLES

Table 3.1 Effect of pole number on the machine performance.....	30
Table 3.2 Comparison of the 6-pole machine performance for different integral windings.....	32
Table 3.3 Comparison of the 6-pole machine performance for different integral windings.....	38
Table 3.4 Comparison of the 4-pole machine performance for different winding designs.....	40
Table 3.5 Comparison of the machine performance with different pole arc angles.....	46
Table 3.6 Effect of the additional barriers on the machine performance.....	50
Table 3.7 Evaluation of the machine performance after each of the proposed rotor modifications.....	52
Table 3.8 Final machine design specifications .....	57
Table 4.1 Extracted coefficients for M45G26 steel .....	82
Table 4.2 Extracted Energetic model parameters for M45G26 steel.....	88

Table 4.3 Comparison between the machine hysteresis losses calculated by the analytical, Energetic and hybrid models .....	102
Table 5.1 Measured exciter parameters .....	120

## NOMENCLATURE

PMSM	Permanent Magnet Synchronous Machine
FEA	Finite Element Analysis
SRM	Switched Reluctance Machine
MMF	Magnetomotive Force
PC	Permeance Coefficient
EMF	Electromotive Force
PWM	Pulse Width Modulation
IEEE	Institute of Electrical and Electronics Engineers
GA	Genetic Algorithm

## LIST OF SYMBOLS

$d$	Direct
$q$	Quadrature
$B$	Flux density
$H$	Magnetic field
$B_r$	Remnant flux density
$H_c$	Coercive magnetic field
$R_m$	Magnet internal reluctance
$R_g$	Air gap reluctance
$R_s$	Steel reluctance
$R_l$	Leakage flux path reluctance
$\phi_l$	Leakage flux
$F_a$	External magneto motive force
$H_m$	Operating field intensity of the magnet
$B_m$	Operating flux density of the magnet
$\mu_0$	Magnetic permeability of free space
$\mu_r$	Relative magnetic permeability
$A_m$	Magnet area
$l_m$	Magnet length
$A_g$	Air gap area
$l_g$	Air gap length
$H_a$	External magnetic field
$B_i$	Intrinsic flux density
$H_d$	Demagnetizing magnetic field
$H_s$	Saturation magnetic field
$B_s$	Saturation flux density
$L_d$	Direct-axis inductance
$L_q$	Quadrature-axis inductance

$B_g$	Air gap flux density
$D_r$	Rotor outer diameter
$P$	Number of poles
$K_{sl}$	Fundamental skew factor
$\sigma_s$	Electrical skew angle
$W_T$	Tooth width
$W_Y$	Yoke width
$S$	Number of slots
$E_q$	Quadrature axis voltage
$I$	Armature current
$X_s$	Synchronous reactance
$V_i$	Input voltage
$\Delta B$	Minor loop magnitude
$B_m$	Minor loop position
$B_p$	Major loop peak flux density
$P_e$	Eddy current loss
$K_e$	Eddy current loss coefficient
$W_h$	Hysteresis energy loss per cycle
$mf$	Modulation frequency
$ma$	Modulation index
$m$	Relative magnetization
$M_s$	Saturation magnetization
$N_e$	Demagnetization factor
$h$	Energetic model parameter relating to saturation
$g$	Energetic model parameter relating to anisotropy
$k$	Energetic model parameter relating to hysteresis loss
$q$	Energetic model parameter relating to pinning sites
$C_r$	Energetic model parameter relating to grain geometry

$H_r$	Reversible field function
$M_p$	Peak magnetization
$\kappa$	Field reversal function
$M_r$	Remnant magnetization
$X_0$	Slope of the initial magnetization curve
$X_c$	Slope of the hysteresis loop at coercivity
$M_m$	Maximum magnetization
$H_m$	Maximum magnetic field
$M_g$	Magnetization at the hysteresis loop knee
$H_g$	Magnetic field at the hysteresis loop knee
$\lambda_m$	Magnetization flux linkage
$i_m$	Magnetization current
$i_a$	Current required to overcome the air gap reluctance
$i_s$	Current required to overcome the steel reluctance
$K_H$	Ratio between the steel magnetization current and the steel magnetic field
$K_B$	Ratio between the magnetization flux linkage and the steel flux density
$L_a$	Air gap inductance
$L_s$	Steel inductance
$L_{cs}$	Steel inductance at coercivity
$I_{cm}$	Current required to bring the magnetization flux down to zero
$F_c$	Steel coercive magnetomotive force
$\lambda_{rm}$	Flux linkage at zero current
$X_c$	Steel susceptibility at coercivity
$B_r'$	Fictitious remnant flux density for the steel
$v_{md}$	Magnetization direct-axis voltage

$\lambda_{md}$	Magnetization direct-axis flux linkage
$i_{md}$	Magnetization direct-axis current
$\lambda_d$	Direct-axis flux linkage
$\lambda_q$	Quadrature-axis flux linkage
$L_{la}$	Armature leakage inductance
$L_{md}$	Magnetization direct-axis inductance
$L_{mq}$	Magnetization quadrature-axis inductance
$i_{ad}$	Armature direct-axis current
$i_{aq}$	Armature quadrature-axis current
$i'_{fd}$	Field d-axis current referred to the armature
$i_a$	Armature phase $a$ current
$i_b$	Armature phase $b$ current
$i_c$	Armature phase $c$ current
$i_d$	Direct-axis current
$i_q$	Quadrature-axis current
$K$	Transformation matrix from $abc$ to $dq$ reference frames
$\theta_r$	Rotor position
$\omega_r$	Rotor speed
$TR$	Turns-ratio
$Z_i$	Measured input impedance
$R_a$	Armature phase resistance
$R_f$	Field resistance

# 1. INTRODUCTION

## 1.1 Background

Permanent magnet synchronous machines (PMSMs) with rare-earth magnets are widely used in the traction drives of electric and hybrid electric vehicles, due to their high efficiency and torque density. However, there is now a possibility of limited supply or uneconomical prices of rare-earth magnets, as China controls the global supply of rare-earth production, supplying over 97% of the world's rare-earth magnets, and consuming most of its production locally [1]. Therefore, it is essential to find alternative motor technologies that do not depend on rare-earth magnets. Induction machines are very reliable, but they have low torque densities compared to rare-earth PMSMs, and since the induction machine is such a mature technology, there is a slim chance of significant performance improvement in the future. Recently, synchronous reluctance machines gained more interest in traction applications [2-4], as they have a robust rotor and they can operate at efficiencies higher than induction machines, due to the absence of rotor copper losses [5]. However, these machines cannot provide the same torque density of rare-earth PMSMs, as they have no field source on the rotor. Switched reluctance machines (SRMs) also have a very robust rotor and they can provide torque densities higher than induction machines [6]. However, there are serious concerns about the application of these machines in electric vehicles, due to their high torque ripple and acoustic noise [7- 9].

Ferrite magnets are inexpensive, thus they are widely used in low cost appliances. However, the Ferrite magnet has about third of the remnant flux density of rare-earth

magnets. Therefore, it is quite difficult to design a Ferrite PMSM with a comparable torque density to rare-earth machines [10-15]. Alnico magnets can operate at flux densities close to rare-earth permanent magnets. However, they are rarely used in electrical machines nowadays, as the magnets can be easily demagnetized by the armature field in the conventional designs of PMSMs. If Alnico PMSMs are designed in such a way that the demagnetization effects are controlled, they can theoretically provide efficiencies and torque densities comparable to rare-earth PMSMs. In addition, the ease of Alnico demagnetization can be utilized to improve the machine efficiency at the high speeds, as the magnet flux can be reduced by demagnetizing armature current pulses that dissipate negligible losses. This eliminates the additional copper losses of the flux weakening current in rare-earth PMSMs.

The simulation of Alnico permanent magnet machines requires special characterization of the magnet properties, as the magnet operating point is sensitive to variations in the armature current and the magnetic circuit reluctance. For the simulation of conventional rare-earth PMSMs, it is sufficient to represent the magnetic characteristics of the permanent magnet by the second quadrant demagnetization curve. On the other hand, for Alnico PMSMs, the magnet operating point can be at any of the four quadrants of the magnet hysteresis loop depending on the magnitude and direction of the armature field. The design and simulation of Alnico permanent magnet machines requires a good understanding and advanced modelling of the magnet hysteretic characteristics.

The hysteresis characteristics of electrical steels also plays an important role in the design and analysis of electrical machines, as the area enclosed by the steel hysteresis loop

represents the core losses in the steel. Core losses in electrical machines account for a large portion of the total losses ranging from 15-25% in induction machines operating with sinusoidal supplies [16] and even higher for PMSMs and SRMs. Therefore, improving the machine efficiency by design optimization requires accurate quantification of core losses during the machine design stage. The currently adopted core loss models in commercial FEA (Finite Element Analysis) electric machine design programs are based on calculating the machine core losses using curve fitting techniques that utilize core loss data provided by steel manufacturers under sinusoidal excitations. These models cannot predict the behavior of electrical steel under distorted flux waveforms, which can be found in electrical machines operating with non-sinusoidal excitation waveforms, such as SRMs. The flux distortion can also be found in conventional electrical machines operating with power electronics converters, which introduces switching harmonic frequencies into the machine driving voltage. Accurate core loss prediction in these machines requires adopting a physics based core loss model that accounts for the steel hysteresis characteristics. The adopted core loss model should also maintain efficient FEA simulation, as the machine optimization process may require simulating thousands of candidate designs. In order to find the optimum design within a convenient simulation time, it is important to have an accurate and computationally efficient core loss model.

## **1.2 Objective**

The objectives of this thesis are:

- Design a high torque density permanent magnet machine using Alnico magnets and utilize the magnet hysteresis characteristics to demagnetize and magnetize the

magnets at different speeds in order to achieve high efficiency throughout a wide speed range.

- Develop a core loss model for electrical machines that can achieve accurate and computationally efficient calculation of the steel hysteresis losses even under distorted flux waveforms.
- Investigate the effects of the steel hysteresis characteristics on the transient response of electrical machines and develop a computationally efficient method to incorporate the hysteresis effects into the machine model.

### **1.3 Thesis Outline**

The thesis is divided into six chapters. Chapter two explains the operation of magnetic materials and introduces the adopted hysteresis models for permanent magnets and electrical steels. Chapter three presents the design procedure for a high torque density variable flux machine with Alnico magnets followed by experimental results of the machine prototype. Chapter four presents a model for calculating the hysteresis loss in electrical machines. The model utilizes both analytical equations and the Energetic hysteresis model in order to provide accurate and computationally efficient loss calculation. In chapter five, a model is developed to incorporate the steel hysteresis effects into the  $dq$ -axes model of brushless excited synchronous generators in order to accurately predict the generator's transient response. Chapter six concludes the thesis and proposes future research work.

## 2. HYSTERESIS OF MAGNETIC MATERIALS

### 2.1 Introduction

The rotation of electrons around the atom nucleus creates a magnetic field that is known as the orbital magnetic moment. The electrons are also spinning around their own axis. This spinning motion creates another magnetic field called the spin magnetic moment. The net magnetic moment of an atom is the addition of the orbital and spinning magnetic moments of all electrons. For most materials, the magnetic moments of the electrons cancel each other. On the other hand, for ferromagnetic materials such as Iron, Cobalt and Nickel, the electrons are arranged so that their magnetic moments add up and create a net magnetic field. In this case, the atom can be viewed as a tiny permanent magnet, which is known as the magnetic dipole [17].

The magnetic domain theory can be adopted to explain the behavior of ferromagnetic materials. A magnetic domain is a small region in which all the magnetic dipoles are aligned in a certain direction. As illustrated in Fig. 2.1, the direction of the magnetic dipoles varies from one domain to another. Therefore, the material is normally in a non-magnetized state, due to the random dipole distribution.

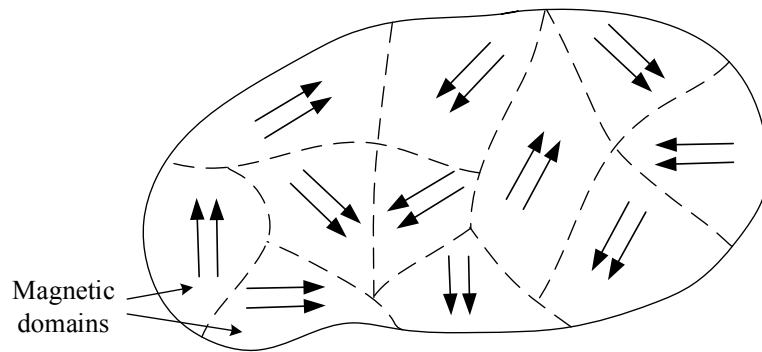


Fig. 2.1 Random domain orientation of a ferromagnetic material

When an external magnetic field ( $H$ ) is applied, the domains that are already in the direction of the applied field tend to grow at the expense of the neighboring ones. This causes the magnetic flux density ( $B$ ) inside the material to increase. As the magnetic field is further increased, other domains rotate their dipoles in the direction of the applied magnetic field. When all the magnetic dipoles are aligned, the material is said to be magnetically saturated, and the  $B$ - $H$  curve behaves in a similar fashion to a non-magnetic material. If the magnetic field is reduced, the  $B$ - $H$  curve does not retrace itself, but it rather follows another path, as shown in the  $B$ - $H$  loop in Fig. 2.2. This irreversibility is known as the magnetic hysteresis. When the magnetic field is reduced back to zero, some of the magnetic domains tend to retain their original magnetization direction. Therefore, the flux density exists in the material even though there is no applied field. This flux density is called the remnant flux density ( $B_r$ ). In order to reduce the flux density to zero, the applied magnetic field has to be reversed. The magnetic field required to bring the magnetic flux density to zero is known as the coercive magnetic field ( $H_c$ ).

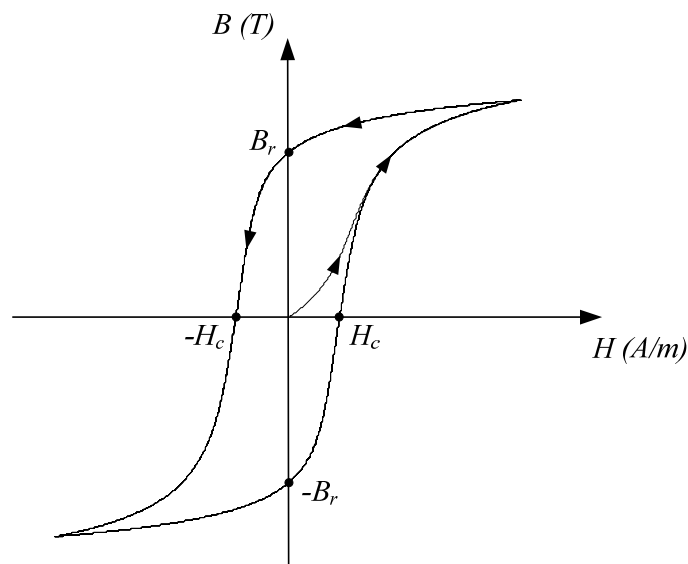


Fig. 2.2 Typical hysteresis loop of a soft magnetic material

Ferromagnetic materials can be classified by their coercivity. Materials with high coercive field are known as hard magnetic materials, while soft magnetic materials have low coercive field. Hard magnetic materials are used in PMSMs as the source of rotor flux, since they can retain their magnetization under high demagnetizing fields. The stator and rotor cores of electrical machines are built with soft magnetic materials, as their high magnetic permeability is utilized to achieve the flux multiplication in the machine core.

## **2.2 Modeling of Magnetic Materials**

### **2.2.1 Hard Magnetic Materials**

The operation of permanent magnets in electrical machines can be simulated by electric circuit analysis, where the magnet is regarded as a flux source, and it can be represented by a Norton equivalent circuit with a current source of the remnant flux  $\phi_r$  in parallel with the magnet internal reluctance  $R_m$ , as shown in Fig. 2.3. The external reluctance of the magnet flux path consists of the air gap reluctance  $R_g$  in series with the steel reluctance  $R_s$ . The leakage reluctance branch represents the leakage flux  $\phi_l$  that emerges from the magnet pole face but does not cross the air gap, as illustrated in Fig. 2.4. In PMSMs, the magnets are also exposed to an external magnetic field produced by the armature current. This external field is represented by a voltage source of the external magneto motive force (MMF)  $F_a$ .

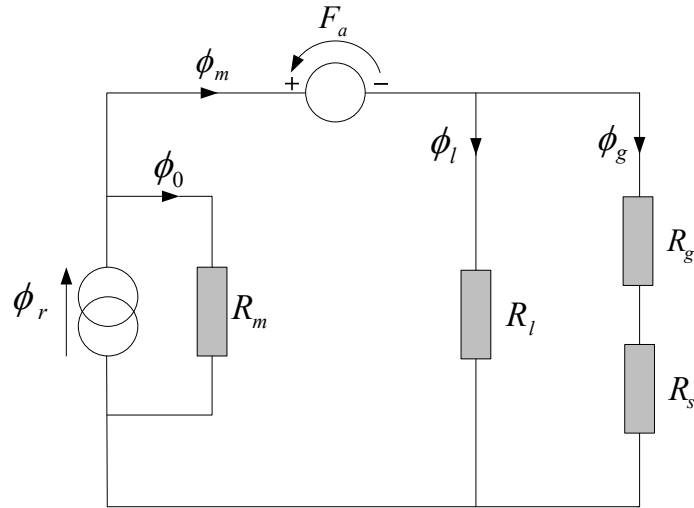


Fig. 2.3 Electric equivalent circuit of a permanent magnet

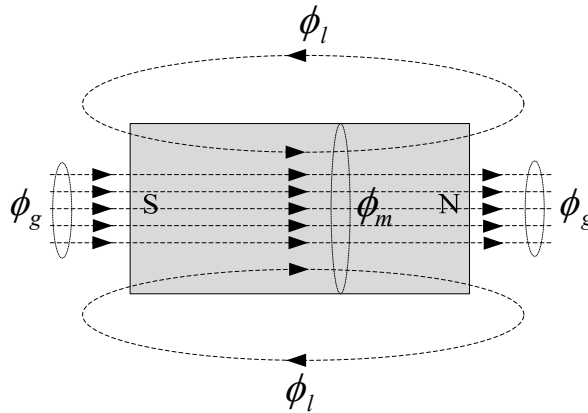


Fig. 2.4 Illustration of permanent magnet flux paths

The magnet operating flux density can be obtained by solving the electric circuit in Fig 2.3. In order to simplify the analytical solution, the leakage flux and steel reluctance are considered negligible. The magnet operating point occurs when the MMF generated by the magnet equates the MMF field required to overcome the air gap reluctance and the applied external field. From the analysis of the magnetic circuit in Fig. 2.3, the field generated by the magnet  $H_m$  can be represented by,

$$H_m = \frac{B_m - B_r}{\mu_0 \mu_r} \quad (2.1)$$

This equation represents the demagnetization curve of the magnet, where the remnant flux density  $B_r$  can be physically interpreted by the intrinsic field produced by the alignment of the magnet domains in the magnetization direction. If the magnet intrinsic field is considered constant, the magnet demagnetization curve can be represented graphically by a line with a slope of the magnet permeability  $\mu_0 \mu_r$ , as shown in Fig. 2.5.

By calculating the MMF across the external field and the air gap reluctance, the magnetic field across the magnet can also be obtained by,

$$H_m = -B_m \frac{l_g A_m \mu_r}{l_m A_g} - H_a \quad (2.2)$$

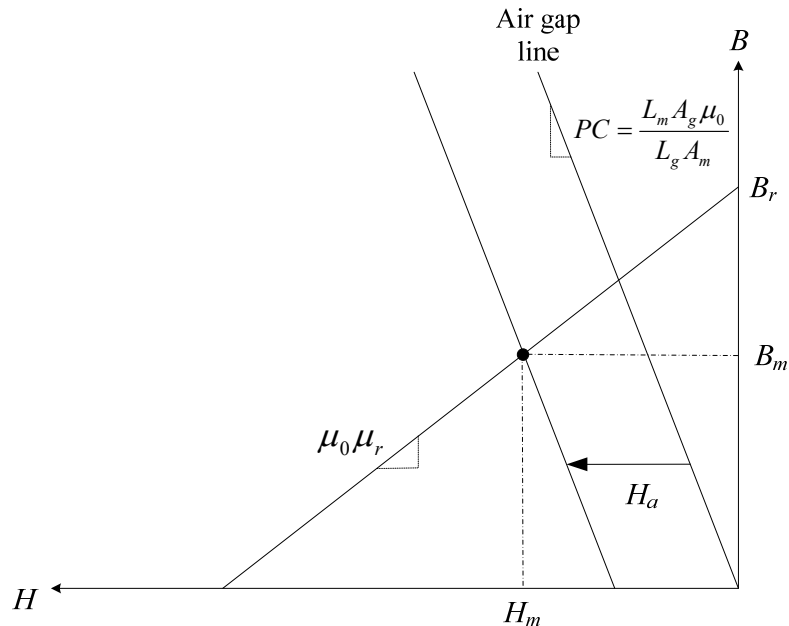


Fig. 2.5 Graphical representation of the magnet operation with an external magnetic field

$l_g$ ,  $l_m$ ,  $A_g$ ,  $A_m$  and  $\mu_r$  are the air gap length, magnet length, air gap area, magnet area and magnet relative permeability, respectively. Equation (2.2) can be represented graphically by the air gap line with slope of the magnet permeance coefficient ( $PC$ ). This line is shifted from the origin when an external magnetic field  $H_a$  is applied, as shown in Fig. 2.5. The magnet operating point occurs at the intersection of the air gap line with the magnet demagnetization curve.

The preceding circuit analysis is based on assuming a constant intrinsic field. This assumption can be valid for ferrite and rare-earth magnets, where the magnet intrinsic field at ambient temperature is mostly constant throughout the second quadrant. Therefore, the resulting demagnetization curve becomes a straight line. If the magnet is operating at a lower point in this linear region due to an external demagnetizing field, the magnet will still retain its intrinsic magnetization and if this field is released, the magnet will recoil along its original demagnetization curve. On the other hand, the Alnico magnet can retain its intrinsic field under a limited magnetic field range, if the magnetic field exceeds this range, the magnet intrinsic flux density  $B_i$  decreases, as shown in Fig. 2.6. As a result, the demagnetization curve becomes non-linear in the second quadrant, as a knee in the demagnetization curve appears when the magnet begins to lose its intrinsic magnetization.

Fig. 2.6 illustrates the operation of an Alnico magnet under a demagnetization field. The magnet is first operating under no external field at point  $A$  due to the reluctance of the magnet flux path. If a demagnetization field  $H_a$  is applied, the operating point will shift

beyond the knee to operating point  $B$ . At this point, the intrinsic flux density of the magnet is reduced by  $\Delta B_i$  and the new remnant flux density is equal to  $B_r - \Delta B_i$ . If this demagnetization field is released, the magnet will recover its magnetization along the line parallel to the original demagnetization curve vertically shifted by  $\Delta B_i$ , and the magnet operating point will be shifted to the intersection of the air gap line and the new demagnetization curve (point  $C$ ).

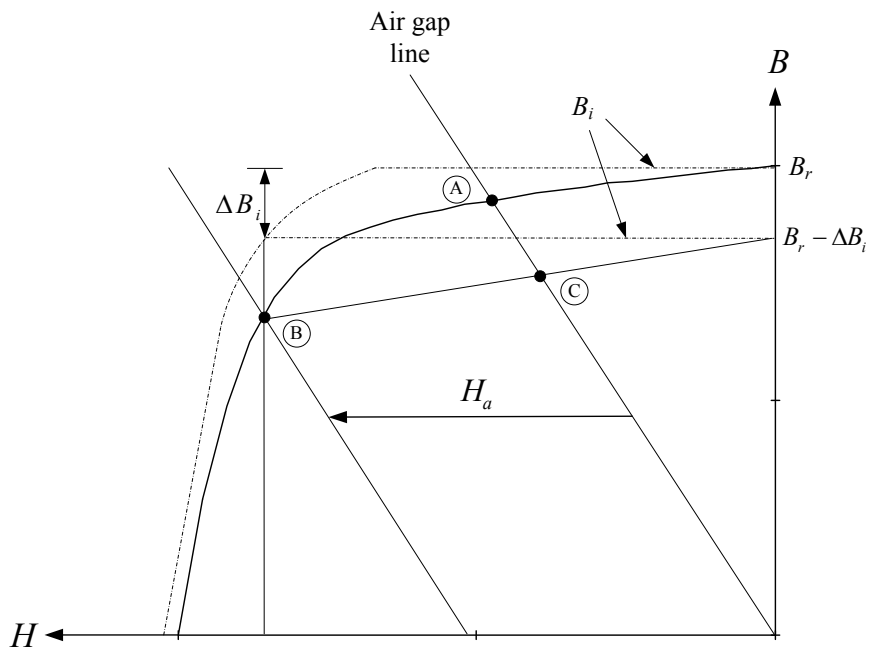


Fig. 2.6 Illustration of irreversible magnet demagnetization

The hysteresis characteristics of Alnico magnet can be simplified by the linearized model illustrated in Fig 2.7. The magnet operates along its main demagnetization curves in the second or fourth quadrants depending on the magnetization direction. If the operating point is shifted below the demagnetization curve knee by a demagnetizing field, the magnet hysteresis curve will be renewed, as it will include a recoil line from the operating point with a slope of the magnet permeability. If the applied external field

reaches  $H_d$ , the magnet will be completely demagnetized. In order to re-magnetize the magnet, a magnetizing field  $H_s$  has to shift the magnet operating point beyond the hysteresis loop knee in the first or third quadrants to reach the saturation flux density  $B_s$ , so that when the magnetizing field is released, the magnet would recoil to its original operating point along the main demagnetization curve.

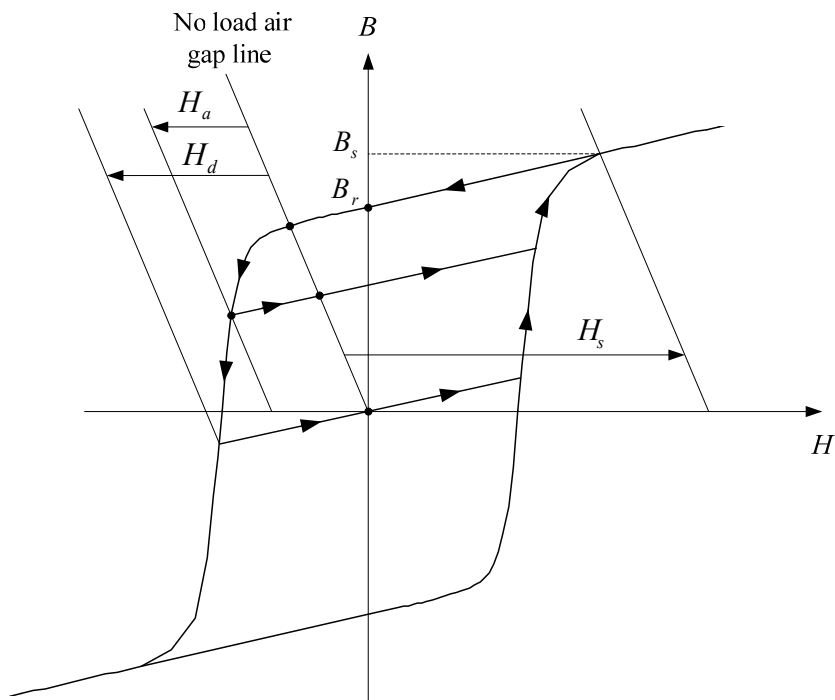


Fig. 2.7 Linearized hysteresis model for Alnico magnets

### 2.2.2 Soft Magnetic Materials

Since the hysteresis characteristics of soft magnet materials are extremely non-linear, the hysteresis process cannot be simulated using a linearized model as in the case of hard magnetic materials. Therefore, a hysteresis model has to be adopted in order to simulate the steel hysteresis loop. Many models are available for the simulation of the magnetic

hysteresis process, ranging from purely mathematical models [18] to physics-based models such as the Preisach model [19, 20], the Jiles-Atherton model [21], and the Energetic model [22]. The accuracy of the mathematical models depends on the availability of experimental data. Therefore, a large data base of measured loops is required for accurate simulation of the hysteresis loops at different magnetization levels and waveforms. Therefore, it is preferred to use the physics based models that can simulate the magnetization process using a set of extracted parameters from the experiment. The Preisach model can accurately simulate the major and minor hysteresis loops by a properly designed Preisach function [23]. However, the model identification requires a complex procedure, and the hysteresis simulation is computationally intensive, as the simulation requires calculating the domain distribution. The Jiles-Atherton model is easier to implement and can achieve faster simulation than the Preisach model. However, the simulation still requires integration over  $dH$ . In addition, the Jiles-Atherton model does not offer closed minor hysteresis loops. The Energetic model is based on considerations of energy balance and statistical domain behavior. The model simulation of major and minor hysteresis loops agrees well with experimental data. The model can also provide fast hysteresis simulation, as the magnetic field can be calculated directly by one equation from the flux density waveforms, which are available in the post-processing stage of the FEA simulation. In addition, the Energetic model is capable of considering the dependence of magnetization on temperature, stress, and magnetization direction. These parameters are obtainable by FEA simulation, and their influence on the steel core magnetic properties can be considered by the model. Consequently, the Energetic model is chosen for the simulation of the steel hysteresis characteristics.

### 3. DESIGN OF VARIABLE FLUX PERMANENT MAGNET MACHINE USING ALNICO MAGNETS

#### 3.1 Review of Variable Flux Machines

A well designed permanent magnet synchronous machine (PMSM) should guarantee that the magnets remain fully magnetized throughout the machine lifetime. This requires the magnet thickness to be large enough to prevent demagnetization by fault currents at the highest rotor operating temperature for rare-earth magnets and the lowest operating temperature for ferrite magnets. Since the rotor magnets can be considered a constant source of flux, the induced armature back EMF is proportional to the rotor speed. When the machine exceeds its base speed, the back EMF becomes larger than the drive capability. Therefore, a demagnetizing  $d$ -axis current has to be applied in order to limit the magnet flux. This current increases the machine losses and reduces the efficiency at high speeds. The concept of variable flux machines is proposed in [24] to provide high efficiency over a wide speed range. In the proposed memory motor, the magnet flux is reduced at high speeds by applying demagnetizing stator current pulses in the  $d$ -axis to control the magnet magnetization level. These pulses dissipate negligible losses, thus avoiding the additional losses of the flux weakening current in conventional PMSMs. In order to re-magnetize the magnets when the motor slows down, a magnetizing  $d$ -axis current pulse has to be applied to achieve full magnetization. The current required to fully magnetize the magnets is usually larger than the machine rated current. While this may not affect the machine thermal rating, as the current has to be applied for only a few milliseconds, the machine inverter should be rated to withstand the full magnetization

current. This may require oversizing the machine inverter.

The design of a memory motor is shown in Fig. 2.1. While this design can provide the magnet flux controllability that can lead to efficiency improvements at high speeds, the proposed machine design has several problems:

1) The rotor is built as a sandwich of permanent magnets, electrical steel and a non-magnetic material, all of which are fixed to a non-magnetic shaft. The manufacturing of the sandwich rotor design is quite complex and the rotor mechanical strength is low compared to interior PMSMs built with magnets buried in one piece of iron core.

2) The trapezoidal magnet design aims to reduce the current required to demagnetize the magnets. However, the machine inverter should also be able to magnetize the magnets even if they were entirely demagnetized by a fault current. Memory motors usually require large magnetization current, as the magnetization pulse should be able to magnetize the wider part of the magnet near the rotor surface.

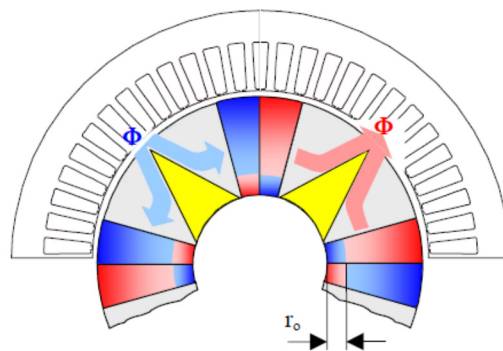


Fig. 3.1 Variable flux memory motor [24]

3) The trapezoidal magnet design forces some of the magnet flux near the shaft to circulate through the rotor [25]. This flux does not cross the machine air gap and it results in a reduction of the machine torque density.

Several alternative designs are proposed in [26-29]. These motors utilize both rare-earth magnets as a constant source of flux and low coercive field magnets to vary the air gap flux density. The torque densities of these machines are still lower than interior PMSMs, as they have lower air gap flux densities. In addition, they can only utilize the magnet torque component. Even if these machines are designed with  $d$  and  $q$  axes inductances ( $L_d$  and  $L_q$ ) similar to interior PMSMs, they will not be able to operate at the optimum torque angle, as it requires applying a demagnetizing  $d$ -axis current component. This will cause irreversible demagnetization of the low coercive field magnets.

A radial design of a variable flux machine is proposed in [30]. The proposed machine design is shown in Fig. 3.2. The rotor barriers can provide inverted saliency ( $L_d > L_q$ ), so that a positive reluctance torque can be produced with a magnetizing  $d$ -axis current component that stabilizes the operation of the low coercive field magnets. However, this machine is built with custom made Samarium Cobalt magnets. These magnets are quite expensive and they contain rare-earth elements. In addition, the proposed radial magnetization pattern makes the magnet susceptible to demagnetization by the armature  $q$ -axis current. To limit the demagnetization effects, the magnet arc is reduced to 35 degrees. As a result, the machine torque density is reduced and even the produced reluctance torque cannot compensate for the significant reduction of the magnet torque component.

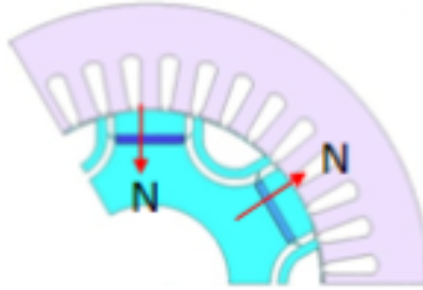


Fig. 3.2 Radial variable flux machine with inverted saliency [30]

## 3.2 Analytical Machine Design

This section provides an analytical design procedure for variable flux machines. The target is to determine an initial rotor design for a machine that can provide torque density comparable to rare-earth PMSMs, while only using Alnico magnets.

### 3.2.1 Magnet Orientation

In order to design a high torque density permanent magnet motor, the magnets should be able to provide high air gap flux densities at no-load and maintain their magnetization state under high armature currents. For radial flux PMSMs, the armature MMF is sinusoidally distributed along the rotor surface. This causes the magnet rear edge to be subjected to a demagnetizing field. For rare-earth PMSMs, the magnets can retain their intrinsic flux under high demagnetizing fields. However, for radial variable flux machines with low coercive field magnets, the magnets are demagnetized by the load armature field. This can be avoided by designing the machine with smaller magnet arc, which leads to a reduction in the machine torque density. On the other hand, for the tangentially magnetized configuration shown in Fig. 3.3, the armature  $q$ -axis flux

primarily passes along the magnet face instead of going through the magnets as in conventional radial designs. Therefore, the magnet length can be increased to achieve a high air gap flux density without exposing the magnets to a demagnetizing field. In addition, the magnet length is uniformly exposed to the armature  $d$ -axis flux. This facilitates the demagnetization and magnetization processes. Therefore, the tangentially magnetized configuration is chosen for the design of a variable flux machine in order to increase the machine torque density and to reduce the magnetization current.

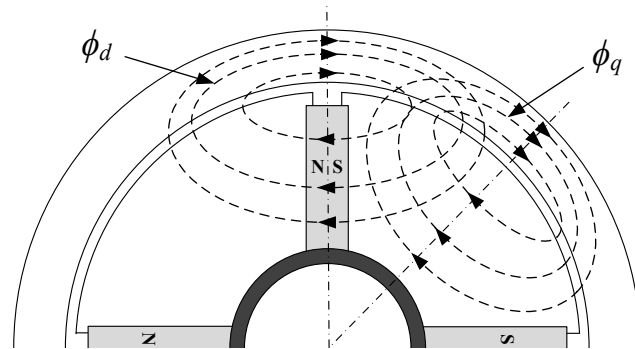


Fig. 3.3 Illustration of  $d$  and  $q$  axes flux paths in tangentially magnetized PMSM

### 3.2.2 Magnet Type

Alnico magnets are a suitable choice for variable flux machines as they have high remnant flux density and low coercive field, thus allowing the machine to achieve the high torque density of rare-earth PMSMs and the flux controllability of variable flux machines. In addition, Alnico magnets are stable at high temperatures, as they can withstand temperatures up to  $500^{\circ}\text{C}$  without being demagnetized.

Fig. 3.4 shows the demagnetization curves for different grades of Alnico magnets and their respective no-load operating points with different permeance coefficients ( $PC$ s). It

can be seen from Fig. 3.4 that operation at high flux densities is possible with Alnico 9 and Alnico 5. In order to operate Alnico 5 at high flux density, a permeance coefficient of more than 20 is required. This requires using very wide magnets, which makes the re-magnetization process more difficult. In addition, the flux density provided by Alnico 5 is sensitive to variations in the permeance coefficient. Therefore, any increase in the steel reluctance due to the additional armature flux can cause a significant drop in the magnet flux density and therefore the machine torque capability. On the other hand, more stable operation can be provided by Alnico 9, which has linear demagnetization characteristics throughout a wider magnetic field range. Operation in this stable region can be achieved with a permeance coefficient around 10, which corresponds to smaller magnet thickness. Therefore, grade 9 magnet is chosen for the design of the Alnico variable flux machine.

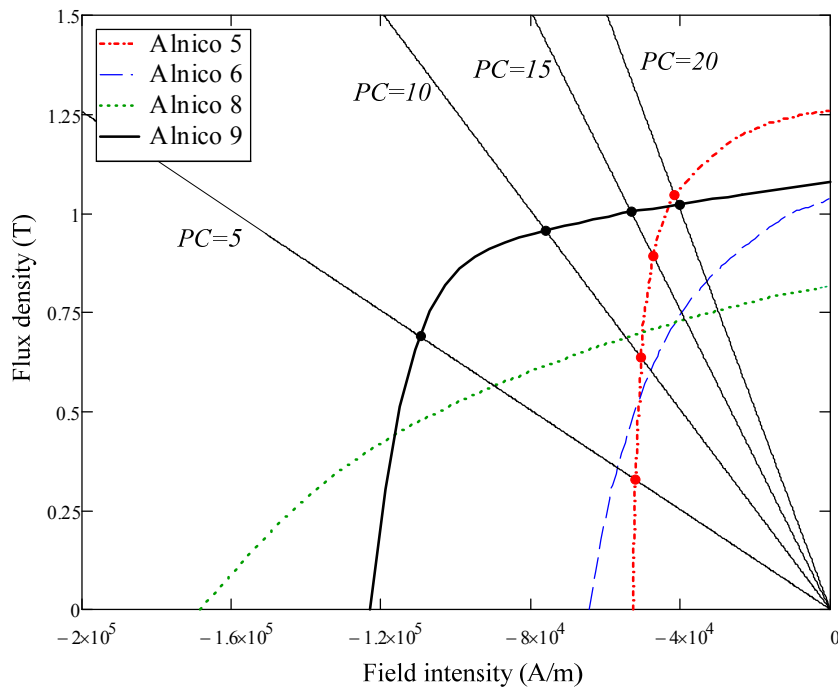


Fig. 3.4 Demagnetization curves of different Alnico grades showing the magnet operating points at no load

### 3.2.3 Magnet Dimensions

A magnetic circuit analysis of the tangentially magnetized rotor in Fig. 3.5 is conducted in order to calculate the initial magnet dimensions. The magnet permeance coefficient ( $PC$ ) is first determined from the demagnetization curve and the desired magnet operating point, as discussed in the previous section. The magnet thickness is then calculated by,

$$w_m = 2l_g \times \frac{B_g}{B_r} \times (PC + \mu_r) \quad (3.1)$$

Where  $B_r$ ,  $B_g$ ,  $\mu_r$  and  $l_g$  are the magnet remnant flux density, the desired air gap flux density, the magnet recoil permeability and the air gap length, respectively. An initial target value for the air gap flux density is set to 0.8 T in order to reduce the effects of stator teeth saturation. The air gap length has to be minimized in order to reduce the required magnet thickness and the re-magnetization current. Therefore, the mechanical and manufacturing constrains are considered for the calculation of the minimum allowable air gap length. The initial air gap length is set to 0.4 mm, which is similar to a commercial induction machine of a similar rotor size. The magnet length required to deliver the desired air gap flux density can then be calculated from the magnetic circuit analysis by,

$$l_m = \frac{B_g}{2B_m} \left( \frac{\pi D_r}{p} - w_m \right) \quad (3.2)$$

$D_r$  and  $p$  are the rotor diameter and the number of machine poles.

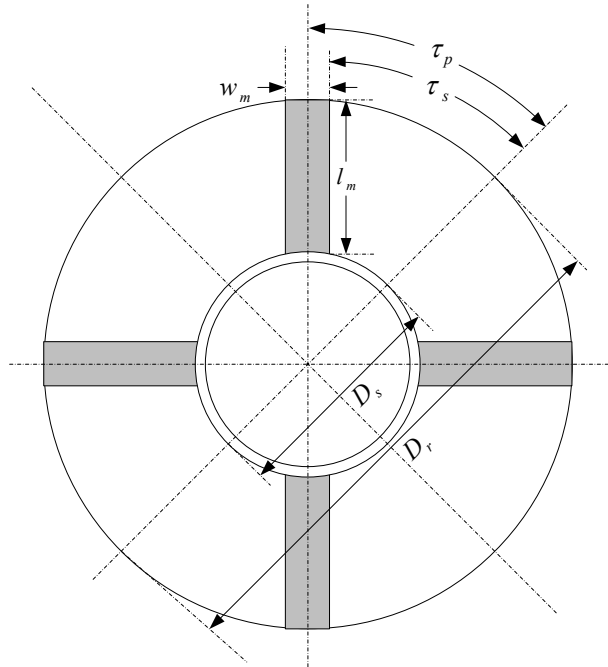


Fig. 3.5 Key dimensions of tangentially magnetized PMSM rotor

### 3.3 Finite Element Based Machine Design

The analytical design procedure presented in section 3.2 is first adopted to obtain the initial design parameter for a variable flux machine. The initial machine design for the 4-pole machine in Fig. 3.5 is then implemented in JMAG FEA software in order to account for the steel saturation effects, which is essential for accurate calculation of the machine magnetization and demagnetization characteristics. As expected, the analytical results agree well with the FEA results when the stator core is designed with enough stator yoke and teeth width to avoid steel saturation, and the simulated magnet operating point at no-load is close to its target value. However, when the machine operates at full load, the armature  $q$ -axis current drives the stator steel to saturation. This increases the magnet flux path reluctance, thus shifting the magnet operating point beyond the demagnetization

curve knee. In order to limit the stator steel saturation caused by the load  $q$ -axis flux, a barrier is carved in the rotor steel along the  $d$  axis, as shown in Fig. 3.6. The added barrier also reduces the  $q$ -axis inductance to a lower value than the  $d$ -axis inductance. This allows the machine to produce a positive reluctance torque while applying a magnetizing  $d$ -axis current component that shifts the magnet operating point at full load towards the linear region, thus avoiding demagnetization. A rib is also inserted above the magnet to improve the machine saliency and to facilitate the rotor manufacturing process.

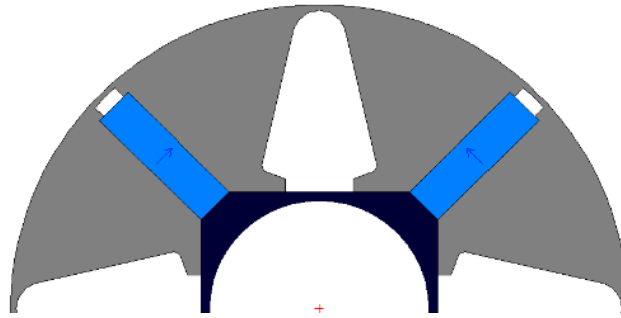


Fig. 3.6 Cross section of the preliminary 4-pole rotor design

### 3.3.1 Hysteresis Based Finite Element Simulation

For conventional rare-earth PMSMs, the machine should be designed so that the magnet would operate at the linear region of the demagnetization curve even under fault conditions. Therefore, it is sufficient to represent the magnet in the FEA simulation by the second quadrant demagnetization curve. On the other hand, for variable flux machines with low coercive field magnets, the magnet operating point can be at any of the four quadrants of the hysteresis loop depending on the magnitude and direction of the armature field. Therefore, the hysteresis characteristics of the magnet have to be considered throughout the FEA simulations. The following section explains how the

magnet demagnetization and magnetization dynamics are considered for different operating conditions.

*1) Loading conditions*

Since the linear region of the demagnetization curve of Alnico is limited compared to rare-earth magnets, the magnet operating point can be shifted below the demagnetization curve knee during normal machine operating conditions. The magnet operating point can be either shifted by the application an armature  $d$ -axis current or by the variation of the magnetic circuit reluctance.

When the machine is rotating, the magnet flux path reluctance changes due to the stator slotting. Figs. 3.7 and 3.8 show the flux density distribution of a 24-slot 4-pole machine when the magnets are aligned with a slot and a tooth, respectively. When the magnet is aligned with a slot, the flux is distributed through six of the stator teeth. When it moves towards the next tooth, the magnet flux becomes concentrated within only five of the stator teeth, as shown in Fig. 3.8. This causes the teeth flux density level to increase, thus increasing the magnet flux path reluctance. As a consequence, the magnet operating point changes with the rotor position. However, this variation is negligible at no-load, as the stator flux density level is low and the stator teeth are far from the saturation region. On the other hand, when the machine is operating at full load, the additional armature flux increases the flux density level in the stator. Therefore, a small rise in the steel flux density can affect the magnet flux path reluctance. The reluctance increase when the magnet aligns with a tooth can shift the magnet operating point below the demagnetization curve knee, as illustrated in Fig. 3.9. As a result, when the magnet

moves to the next slot, it will not recover back to the original operating point. Instead, it will recover along the recoil line parallel to the original demagnetization curve.

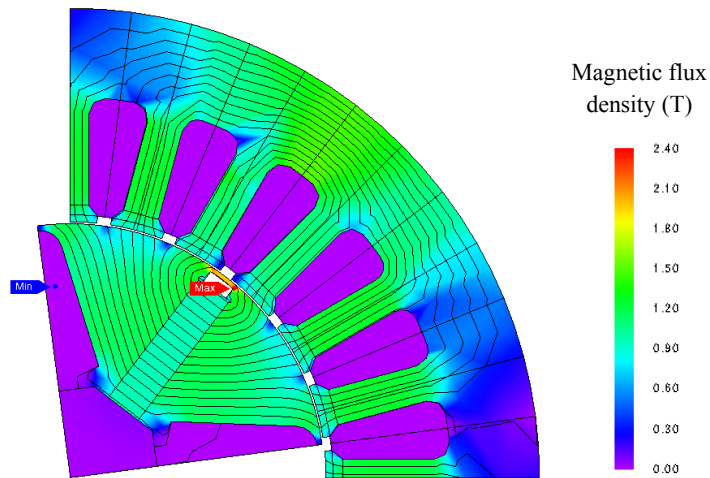


Fig. 3.7 Flux density distribution when the magnet is aligned with a slot at no-load

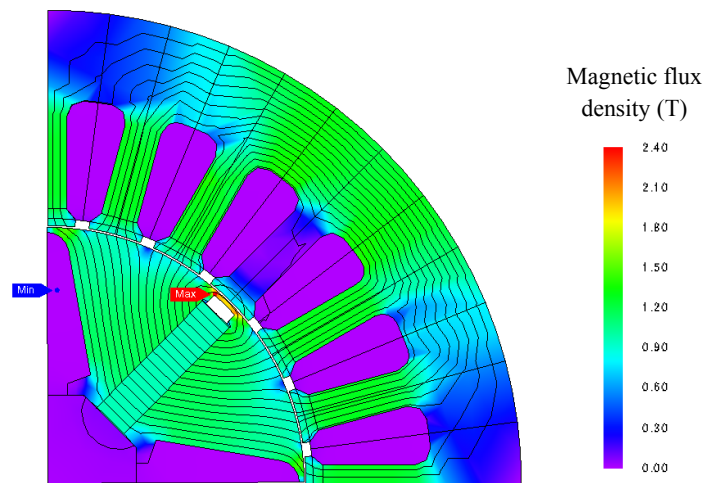


Fig. 3.8 Flux density distribution when the magnet is aligned with a tooth at no load

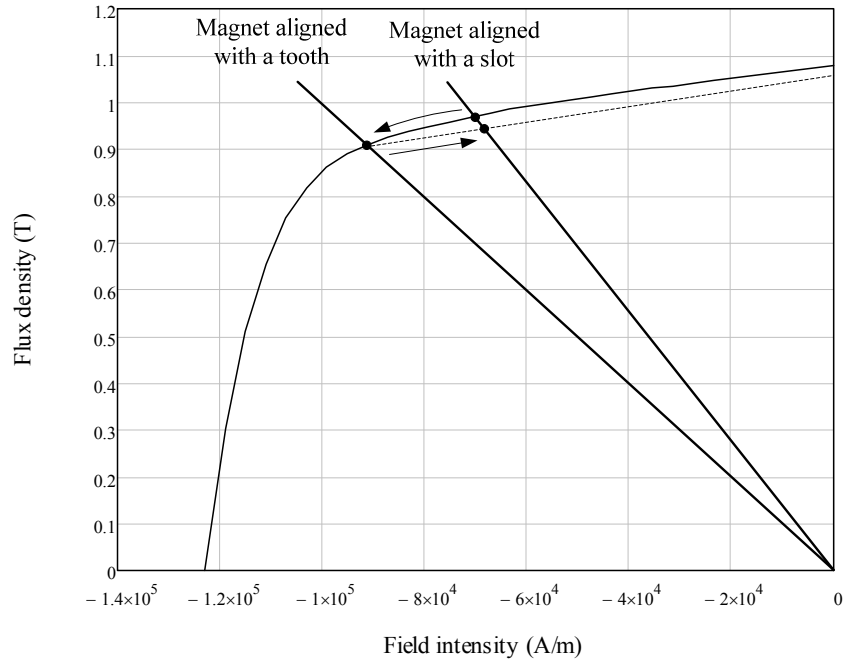


Fig. 3.9 Illustration of the variation of magnet operating point due to stator slotting

The process of irreversible demagnetization is considered throughout the FEA simulations. The magnet demagnetization curve in each element is calculated based on the operating point in the previous step. If the operating point falls below the knee, the magnet demagnetization curve will be renewed, as it will include the recoil line from the operating point in the previous step to a new remnant flux density. Fig. 3.10 compares the simulated magnet flux density at full load with and without considering the irreversible demagnetization. It can be seen that lower magnet flux density is obtained when taking the irreversible demagnetization into account.

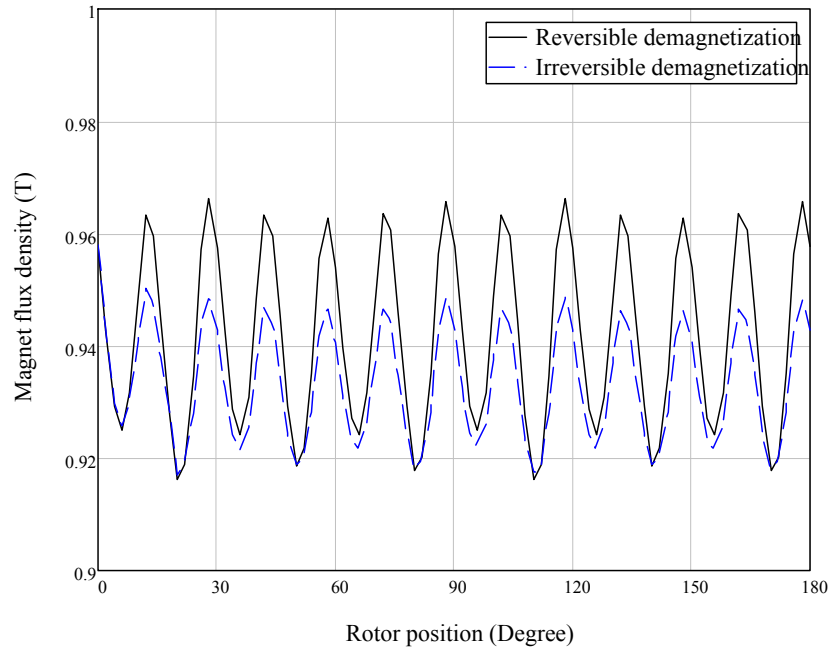


Fig. 3.10 Effect of irreversible demagnetization on the simulated magnet flux density at full load

## 2) Demagnetization

The magnet flux of variable flux machines can be controlled by armature  $d$ -axis current pulses. This is utilized when the induced back EMF reaches its upper limit at high speed, as a demagnetizing  $d$ -axis current pulse is applied to reduce the magnet flux, thus allowing the machine to operate at a wider speed range. The demagnetization dynamics of the machine are also examined using the FEA simulation that considers the magnet's irreversible demagnetization. Fig. 3.11.a shows the simulated flux linkage of a fully magnetized 4-pole machine running unloaded at 2000 rpm. At a simulation time of 0.015 seconds, a demagnetizing  $d$ -axis current pulse is applied, as shown in Fig. 3.11.b. When the current pulse is released, the magnet recoils to a lower flux density, as shown in Fig. 3.11.c. This leads to a corresponding reduction in the simulated machine flux linkage.

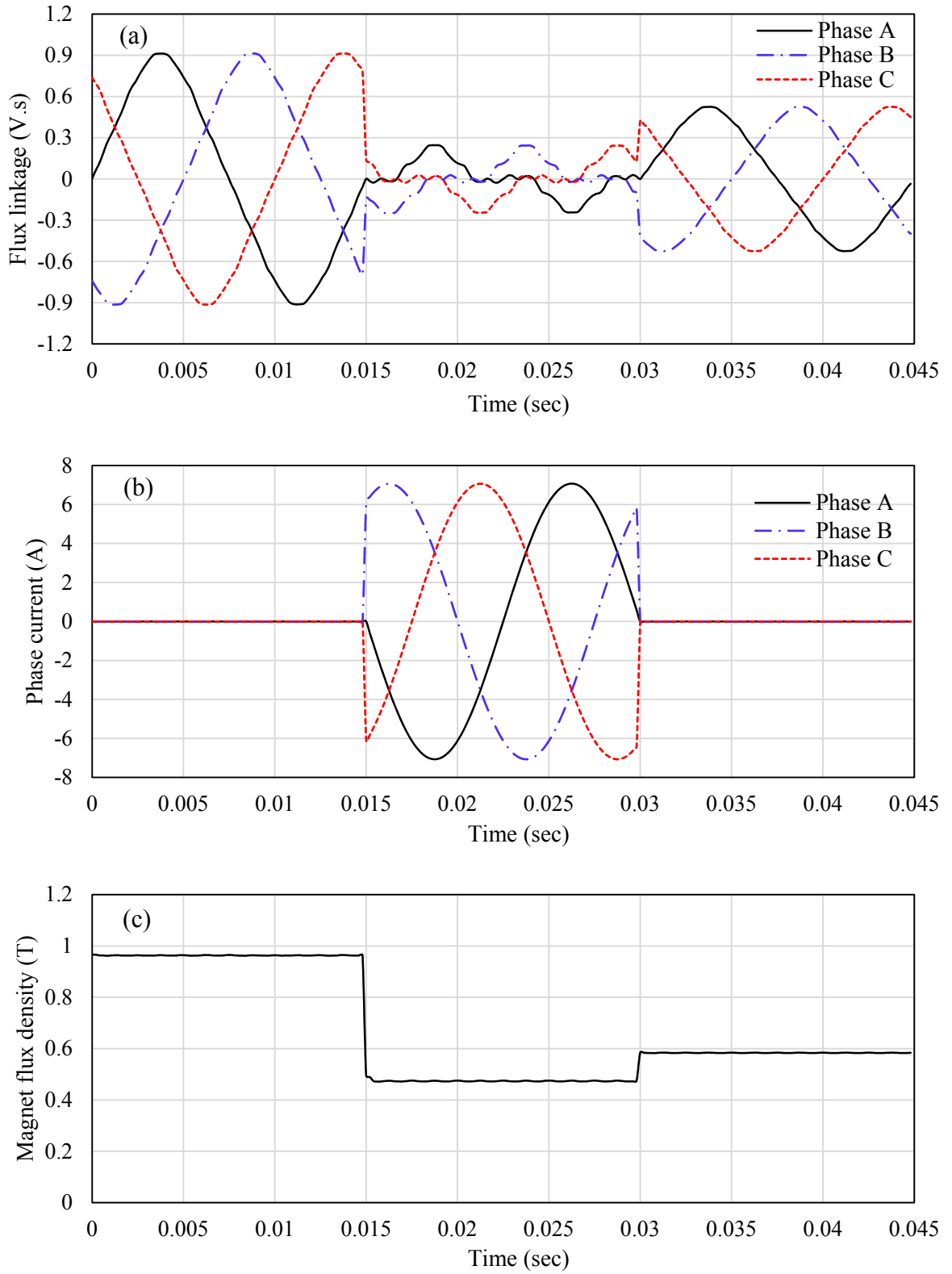


Fig. 3.11 Simulated waveforms in FEA when a demagnetizing pulse is applied

Fig. 3.12 shows the simulated induced back EMF after applying demagnetizing pulses of different magnitudes. It can be seen that the induced back EMF can be controlled by changing the magnitude of the  $d$ -axis current pulse. When the demagnetizing pulse exceeds 8A, the magnet becomes completely demagnetized. This demagnetizing current is lower than the rated machine current of 10A.

While the width of the applied pulse in the FEA simulations is 15 ms (1 electrical cycle), the magnet flux density can actually be reduced using much shorter pulses. The required pulse width for reducing the machine flux linkage mainly depends on the winding impedance, which affects the rise and fall time of the current pulse.

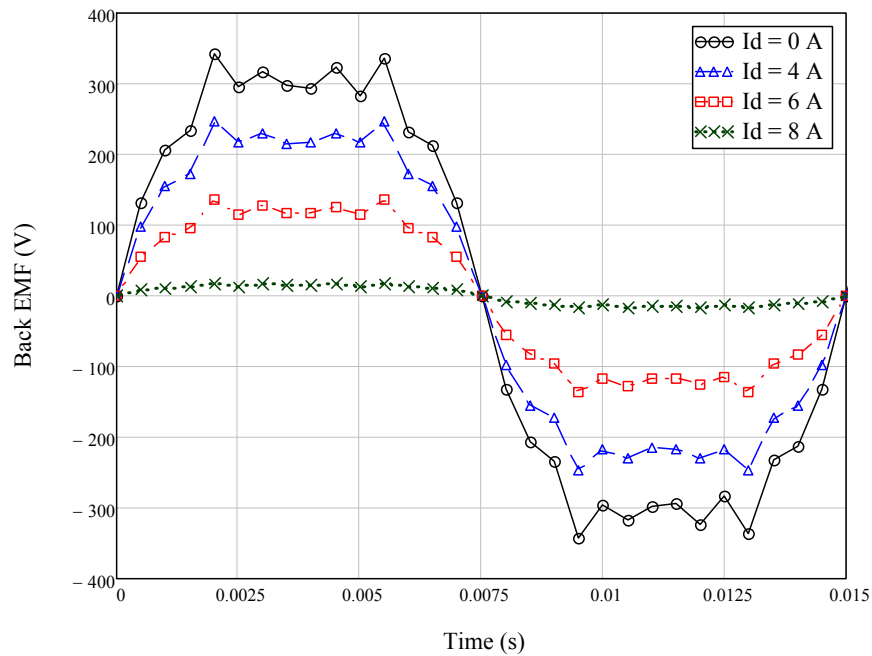


Fig. 3.12 Simulated back EMF after releasing demagnetization current pulses of different magnitudes

### 3) Magnetization

Since the operating principle of variable flux machines is based on demagnetizing the magnets at high speeds, the armature winding should also be able to re-magnetize the magnets to regain the full torque capability when the motor slows down. In order to fully magnetize the magnets, the magnet operating point has to be pushed beyond the knee of the first or third quadrants of the hysteresis loop. This process is simulated in the FEA by representing the magnet with its  $B-H$  curve in the second and third quadrants. A demagnetizing d-axis current is then increased until the magnet reverses its magnetization direction, and reaches the saturation flux density in the third quadrant. The current at which the magnet saturates is considered the full magnetization current.

In the following sections, the effect of various machine design parameter; number of poles, rotor design, winding configuration, lamination design, and machine cooling are investigated through a series of FEA based simulations. The adopted machine design procedure aims to increase the machine torque density and efficiency and to reduce the required magnetization current which leads to a reduction in the machine inverter rating.

#### **3.3.2 Number of Poles**

For variable flux machines, the number of machine poles does not only affect the machine performance, but it also affects the magnetization current requirement. Three variable flux machines of 4 poles, 6 poles and 8 poles are evaluated using FEA. The machines are designed with the same integral winding configuration of 3 slots per pole. The magnet length is varied for each design in order to maintain the same air gap flux

density. Figs. 3.6, 3.13 and 3.14 show the rotor designs of the three machines. The performance and magnetization current for the three motors are compared in table 3.1. Despite the obvious increase of iron losses for higher pole number, the overall machine efficiency improves because of the lower winding losses that results from using shorter end turns.

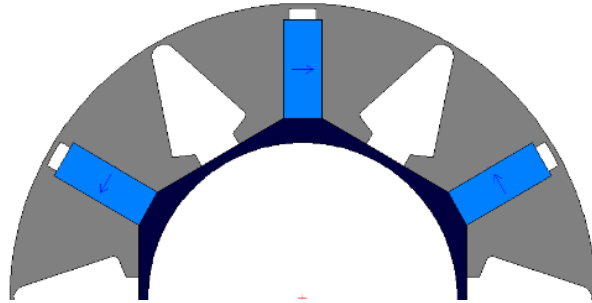


Fig. 3.13 Cross section of the 6-pole rotor design

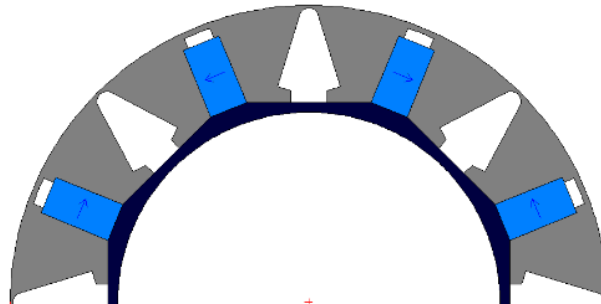


Fig. 3.14 Cross section of the 8-pole rotor design

Table 3.1 Effect of pole number on the machine performance

	4-pole	6-pole	8-pole
Iron loss (Watt)	138.6	153.4	167.5
Winding loss (Watt)	369.1	315.2	294.9
Efficiency %	93.9	94.6	95.1
Yoke flux density @ $I_d=25A$ (T)	1.99	1.56	1.20
Magnetization current (A)	19.27	23.60	37.32

The magnetization process is then simulated with the hysteresis based FEA program. It can be seen from table 3.1 that the required magnetization current increases with the pole number, as the number of armature turns for each magnet is inversely proportional to the number of machine poles. Therefore, machines with higher pole number require more current in order to deliver the same armature MMF. As shown in table 3.1, the 8-pole machine requires about double the magnetization current of the 4-pole design. On the other hand, the 6-pole machine requires only 18% higher magnetization current, as it has lower stator yoke flux density compared to the 4-pole design, thus avoiding stator yoke saturation. Therefore, lower MMF is required to overcome the stator steel reluctance. Accordingly, the 6-pole machine is chosen for further investigations as it has high efficiency compared to the 4-pole machine and it requires lower magnetization current than the 8-pole machine.

### **3.3.3 Stator Design**

The stator design is critical for the design of variable flux machines, as it impacts the machine performance as well as the magnetization current requirement. The generated armature MMF during magnetization is used to overcome the reluctance of the permanent magnet, the air gap and the electrical steel. When the stator steel is saturated during magnetization, most of the armature MMF is dissipated over the steel reluctance. Therefore, the machine stator should be designed to reduce the steel reluctance during magnetization.

### 1) Winding design

In order to assess the effect of slot number on the magnetization current, three 6-pole variable flux machines with integral winding of 18-slot, 36-slot and 54-slot are simulated in FEA. Table 3.2 shows the key simulation results for the three machines. It can be seen that the full magnetization current can be considerably reduced by using low number of slots per pole, as the 18-slot design requires about 40% lower magnetization current than the 36-slot design. Figs. 3.15 and 3.16 show the flux distribution of the two machines when the same magnetizing  $d$ -axis current is applied. For the 18-slot design in Fig. 3.15, it can be seen that all of the stator teeth are carrying the armature flux during magnetization, which results in uniform flux density distribution in the stator teeth. On the other hand, this uniform distribution is not achieved for higher slot numbers, as can be seen from flux distribution of the 36-slot design in Fig. 3.16, where two of the stator teeth above the magnet have low flux density level, thus forcing the magnetizing flux to be concentrated into the other four stator teeth. This raises the tooth flux density level. Therefore, more armature current is required to overcome the saturated teeth reluctance.

Table 3.2 Comparison of the 6-pole machine performance for different integral windings

	18 slots	36 slots	54 slots
Slots/pole	3	6	9
Winding factor	1	0.966	0.960
Torque ripple %	117	27	18.6
Efficiency %	94.6	94.7	94.7
Magnetization current (A)	23.6	33.0	33.5

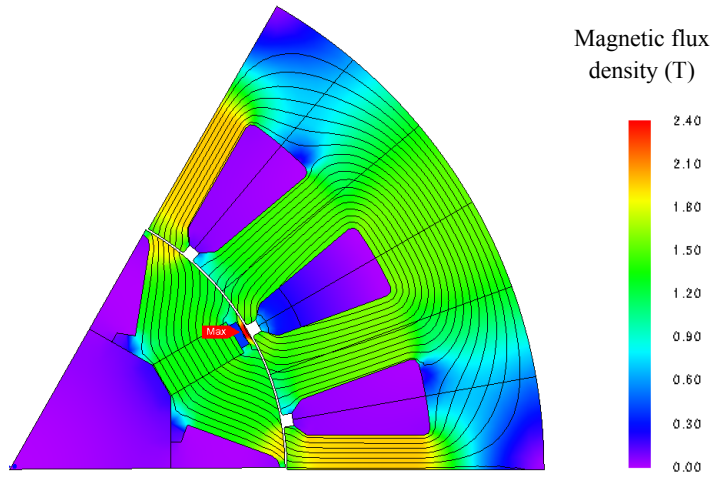


Fig. 3.15 Flux distribution of the 18-slot design during magnetization

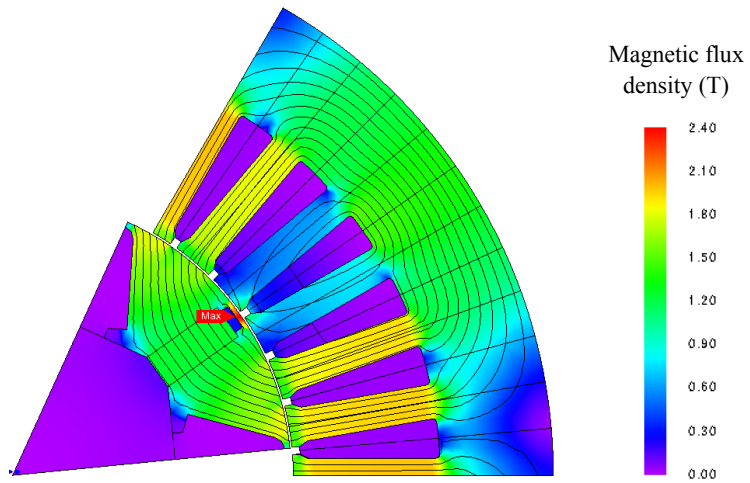


Fig. 3.16 Flux distribution of the 36-slot design during magnetization

While the reduced magnetization current of the 18-slot design can lead to a reduction in the inverter cost, the FEA simulations show that the machine suffers from high torque ripple compared to the 36-slot design, as shown in the simulated output torque of the two machines in Fig. 3.17.

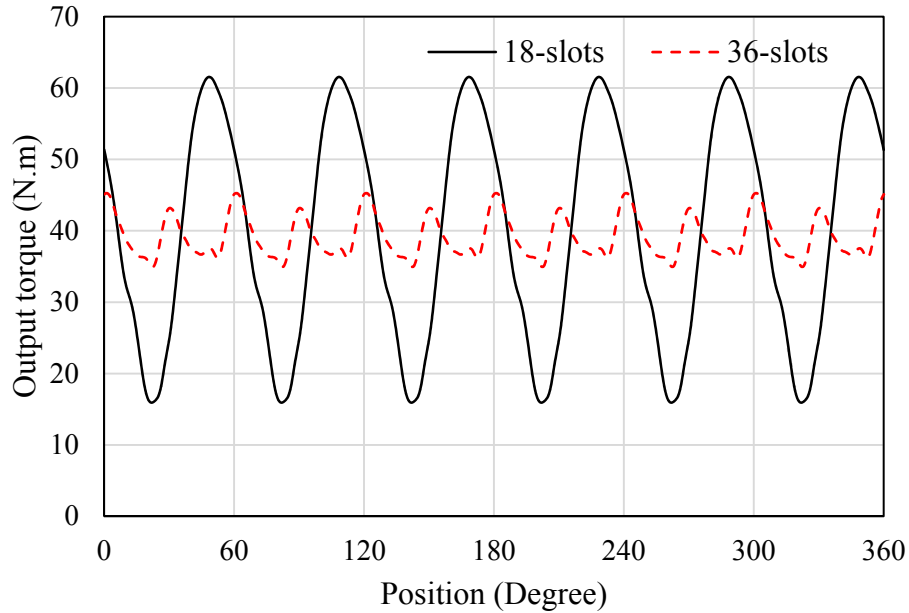


Fig. 3.17 Comparison of the simulated output torque of the 18-slot and 36-slot machines

The large torque pulsations of the 18-slot design are mainly caused by the oscillatory reluctance torque generated due to the stator slotting effects. This torque component can be theoretically eliminated by skewing the stator by 1 slot. The skewed 18-slot machine is simulated using 2D-FEA by dividing the machine into short axial sections; each section is rotated by a small amount of the skew angle [31]. Fig. 3.18 compares the simulated output torque of the skewed and un-skewed machines.

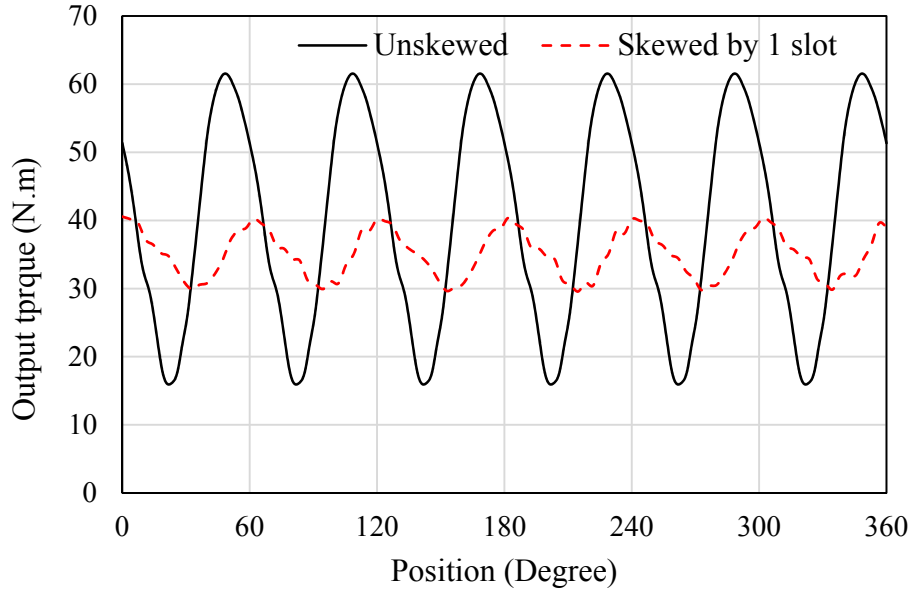


Fig. 3.18 Comparison of the simulated output torque of the skewed and un-skewed 18-slot machines

Ideally, the average output torque of the skewed motor should be reduced by the fundamental skew factor ( $K_{s1}$ ), which can be calculated by,

$$K_{s1} = \frac{\sin\left(\frac{\sigma_s}{2}\right)}{\frac{\sigma_s}{2}} \quad (3.3)$$

where  $\sigma_s$  is the electrical skew angle [32]. According to equation (3.3), skewing the stator by 1-slot should reduce the average torque by about 4.5%. However, the simulated average torque by FEA is 13% lower than the un-skewed motor. This deviation can be explained as follows; the maximum output torque for the designed variable flux machine is obtained when the angle between the armature and magnet flux equals  $77.5^\circ$ . For the skewed motor, this angle only exists at the center of the machine axial length. The front and rear edges of the stator are each electrically shifted by  $\pm 30^\circ$  from the axial length

center. Therefore, the front edge of the rotor experience a torque angle of  $47.5^\circ$ , which requires applying a magnetizing  $d$ -axis current component that stabilizes the magnet operating point. The angle between the armature and rotor fields increases along the machine axial length until it reaches  $107.5^\circ$  at the rotor rear edge. At this torque angle, the magnets are exposed to a demagnetizing  $d$ -axis current component that can cause irreversible demagnetization of the low coercive field magnets. Figs. 3.19 and 3.20 show the simulated flux density distribution at the front and rear edges of the machine at full load. It is clear that the magnet flux density is enhanced at the front edge and reduced at the rotor rear edge because of the direction of the armature  $d$ -axis current component. Fig. 3.21 shows the simulated magnet flux density of the skewed motor in different positions along the machine axial length. It can be seen that part of rotor axial length suffers from irreversible magnet demagnetization. This reduces the overall magnet flux and reduces the machine output torque. Therefore, skewing with large angles is not preferable for variable flux machine with low coercive field magnets, as it can reduce the machine torque density.

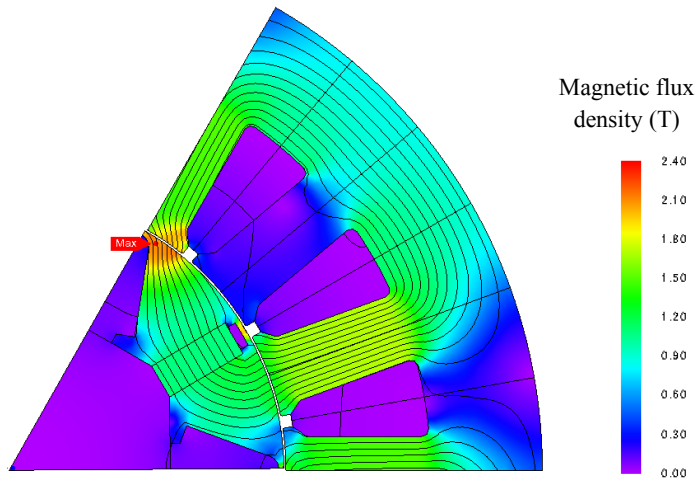


Fig. 3.19 Simulated flux distribution at the front edge of the skewed machine

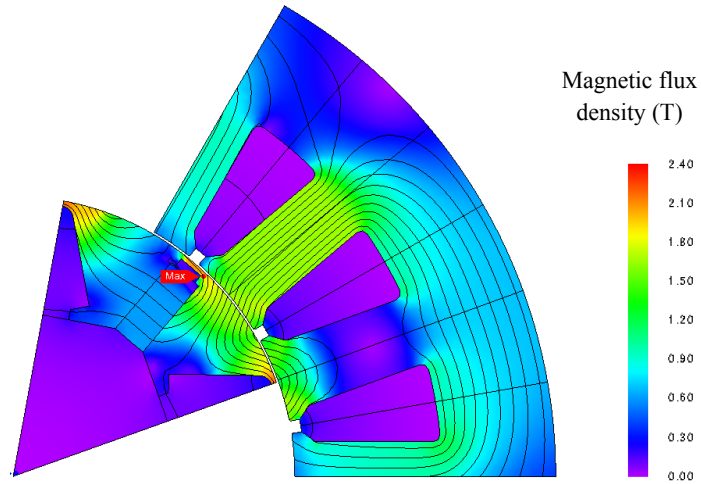


Fig. 3.20 Simulated flux distribution at the rear edge of the skewed machine

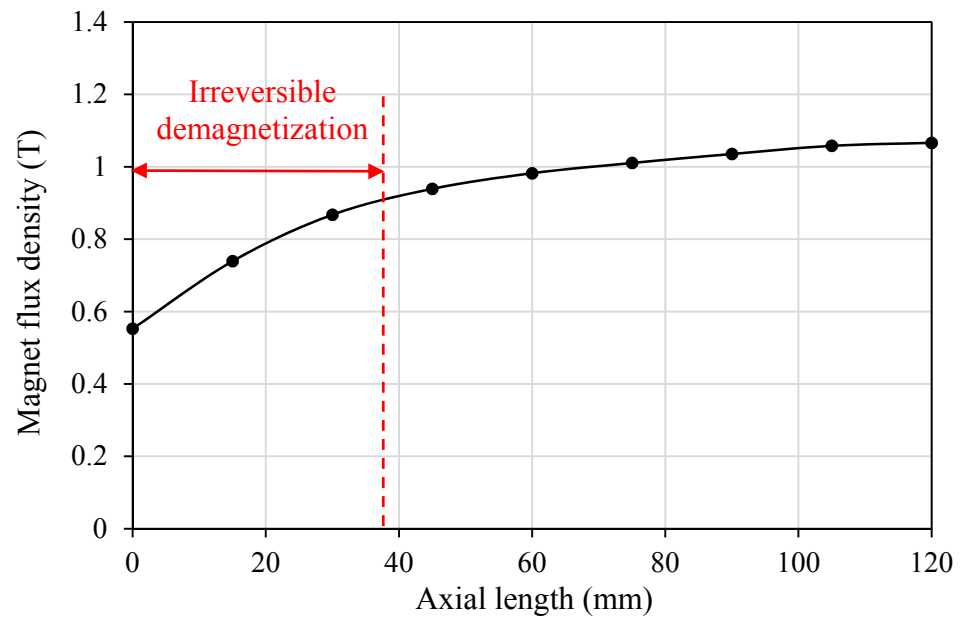


Fig. 3.21 Simulated magnet flux density for the skewed machine at different parts of the machine axial length

From the simulations of the integral winding designs, it is clear that the machine magnetization current can be reduced by using low number of slots per pole. However, there are limited possible configurations for integral windings with low slot per pole ratios. On the other hand, Fractional windings offer more flexibility in the slot number choice. Therefore, the 6-pole machine is simulated with 9-slot and 27-slot fractional windings. Table 3.3 shows the FEA simulation results of the two machines. The 9-slot design has lower magnetization current and torque ripple compared to the 18-slot integral winding design. However, the magnets experience irreversible demagnetization when the machine is operating at full load due to the slotting effects. Fig. 3.22 shows the simulated magnet flux density at full load. When the magnet is aligned with a tooth the effective stator teeth carrying the magnet flux is reduced. This leads to the saturation of the stator teeth, which shifts the magnet operating point below the demagnetization curve knee, where the magnetization loss is irreversible, so when the magnet moves to the next slot, it recoils to a lower flux density level, as shown in Fig. 3.22.

Table 3.3 Comparison of the 6-pole machine performance for different integral windings

	9 slots	27 slots
Slots/pole	1.5	4.5
Winding factor	0.866	0.945
Torque ripple %	110.1	12.5
Efficiency %	93.8	94.8
Magnetization current (A)	20.61	30.25

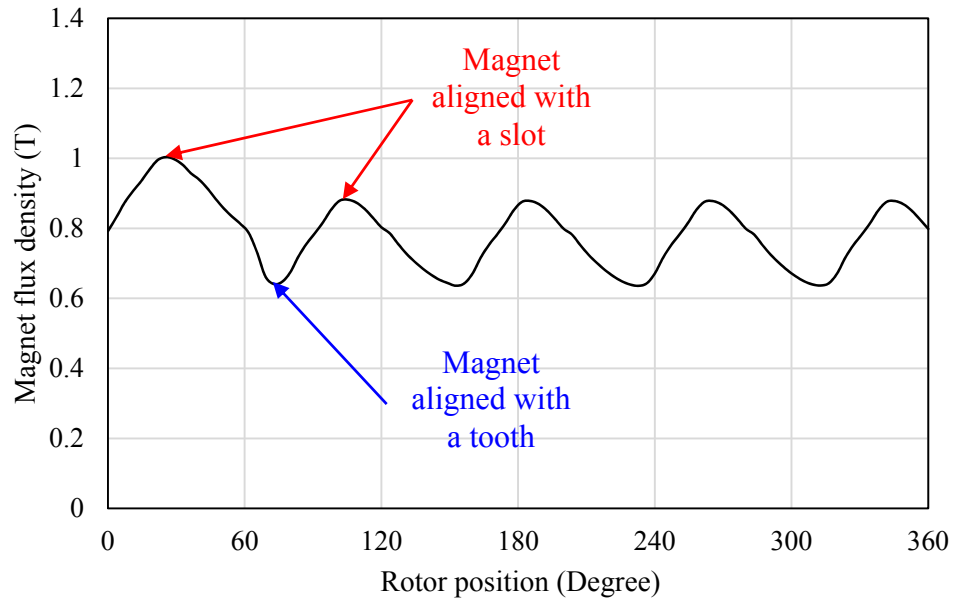


Fig. 3.22 Simulated magnet flux density for the 6-pole 9-slot machine at full load

The magnet flux density variation due to the slotting effects is more pronounced in machines with lower slot per pole ratios. For the 9-slot fractional winding design, this variation is large enough to cause irreversible magnet demagnetization at full load, which reduces the machine output torque. On the other hand, the reluctance variation does not affect the performance of the 27-slot fractional winding design, as the magnet operating points at full load lie in at the linear region of the demagnetization curve. The 27-slot design also has the lowest torque ripple and the highest efficiency among all the simulated 6-pole machines, as can be seen from tables 3.2 and 3.3. Therefore, the 27-slot fractional winding design is chosen for further investigations, as it has low torque ripple compared to the 18-slot integral winding design, and it has lower magnetization current than the 36-slot and 54-slot integral winding designs.

While fractional windings offers more flexibility in the slot number choice for machines with low slot per pole ratios, there are few configurations for 6-pole machines that can achieve balanced 3-phase windings. On the other hand, there are many configurations for the 4-pole machine with low slot/pole ratios that can have balanced windings [32]. Therefore, the performance of the 4-pole rotor design in Fig. 3.6 is also investigated with fractional windings of 15-slot, 18-slot and 21-slot. Table 3.4 shows the FEA simulation results of the 4-pole machine with different integral and fractional winding designs. It can be seen that the fractional windings can achieve smoother output torque. However, the magnetization currents of the 18-slot and the 21 slot designs are higher than the integral winding designs. These machines may require larger inverters. On the other hand, the 15-slot design has the lowest magnetization current among the simulated 4-pole machines. However, the magnets suffer from irreversible demagnetization at full load due to the machine slotting effects.

Table 3.4 Comparison of the 4-pole machine performance for different winding designs

	Integral windings			Fractional windings		
	12 slots	24 slots	36 slots	15 slots	18 slots	21 slots
Slots/pole	3	6	9	3.75	4.5	5.25
Winding factor	1	0.966	0.960	0.910	0.945	0.953
Torque ripple %	155.3	46.8	38.2	18.2	16.2	18.6
Efficiency %	93.9	94.1	94.2	94	94.1	94.1
Magnetization current (A)	19.27	24.78	24.78	22.17	27.32	24.97

## 2) Lamination design

If the stator steel is saturated during magnetization, most of the magnetization MMF will be used to overcome the steel reluctance instead of creating a magnetizing field across the magnets. Therefore, larger armature current would be required to reach the magnet saturation flux density. The effect of steel saturation on the magnetization requirements is investigated by simulating the magnetization process with different values of tooth width ( $W_T$ ) and yoke width ( $W_Y$ ). Fig. 3.23 shows the simulated full magnetization current for the 6-pole 27-slot variable flux machines with different tooth width. It is clear that the tooth width has a great impact on the magnetization current, as it can be reduced by about 40A if the tooth width is increased from 7 mm to 9 mm. Once teeth saturation is avoided, further increase of the tooth width is not beneficial as the reduction in the magnetization current is negligible and the corresponding reduction in the slot area reduces the available area for the armature copper.

The same magnetization trend can also be observed with the stator yoke width, as shown in Fig. 3.24. It is obvious from Figs. 3.23 and 3.24 that the magnetization current can be reduced by using wider stator teeth and yoke. However, the stator lamination design should maintain enough slot area for the winding. Therefore, the following procedure is used for the design of the stator lamination.

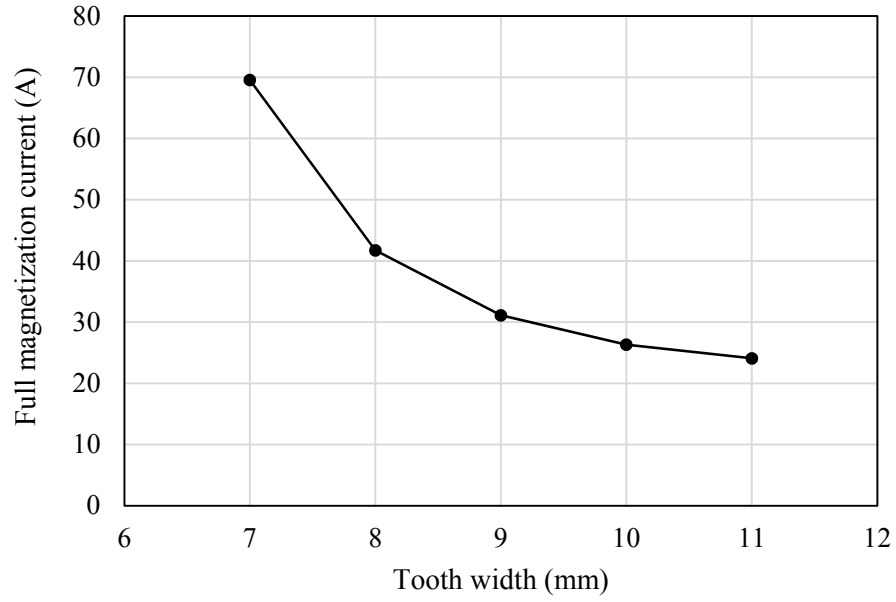


Fig. 3.23 Simulated full magnetization current for machines with different tooth width

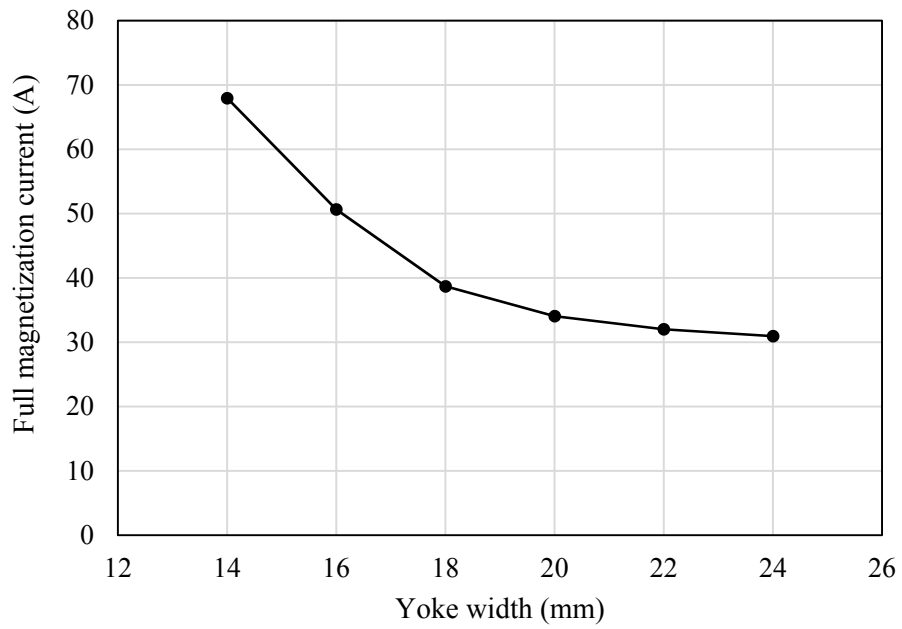


Fig. 3.24 Simulated full magnetization current for machines with different yoke width

First, the stator winding is designed and the required copper area in each slot is calculated. The slot area is then calculated based on the maximum feasible slot fill factor. The slot area and the stator outer and inner diameters are kept constant, then the stator tooth and yoke width are varied simultaneously in order to keep the slot area constant. For each design, the ratio between the teeth per pole to the yoke width is calculated by,

$$\text{Teeth/ yoke} = \frac{W_T \times S}{W_Y \times 2P} \quad (3.4)$$

$P$  and  $S$  are the number of machine poles and stator slots. When the teeth to yoke ratio approaches one, the stator core should have uniform flux density level during magnetization, but this might not result in minimized stator steel reluctance. In order to find the ratio at which the stator reluctance is minimized, the magnetization characteristics are simulated for machines with different teeth to yoke ratios. The corresponding simulated magnetization current is displayed in Fig. 3.25. It can be seen that the minimum magnetization current is obtained at a teeth to yoke ratio of 1.18.

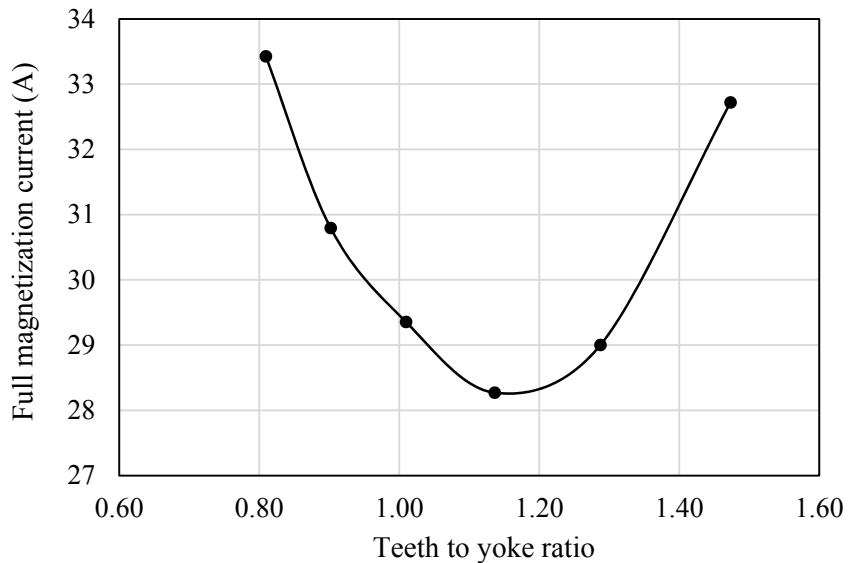


Fig. 3.25 Simulated magnetization current for machines with different teeth to yoke ratio

### *3) Stator cooling*

The cooling system design is of great importance for PMSMs in general, as it does not only affect the insulation life time, but it also affects the machine efficiency, as the copper losses increases with the winding temperature. For variable flux machines, special attention has to be paid in the cooling system design, since it also impacts the machine inverter rating. The typical permissible current density in the stator slots can range from 5 A/mm<sup>2</sup> for totally enclosed natural convection cooling to 20 A/mm<sup>2</sup> for liquid cooled machines [32]. Therefore, the rated Ampere.turns of the stator winding can be greatly increased with improved cooling. For variable flux machines with advanced cooling methods, the magnetization MMF can be obtained within the machine rated current, thus avoiding oversizing the inverter [33]. Therefore, variable flux machine is a promising option for traction motors, where the machine stator is usually cooled by the existing vehicle cooling system.

#### **3.3.4 Rotor Design**

While the 27-slot fractional winding has the best performance among the simulated 6-pole stator winding designs, the machine back EMF still contains high harmonic content, as shown in Fig. 2.26. Several modifications are applied to the tangentially magnetized rotor design in Fig. 3.13 in order to improve the back EMF quality and to increase the machine torque density and efficiency [34-36] while maintaining the magnetization current requirement.

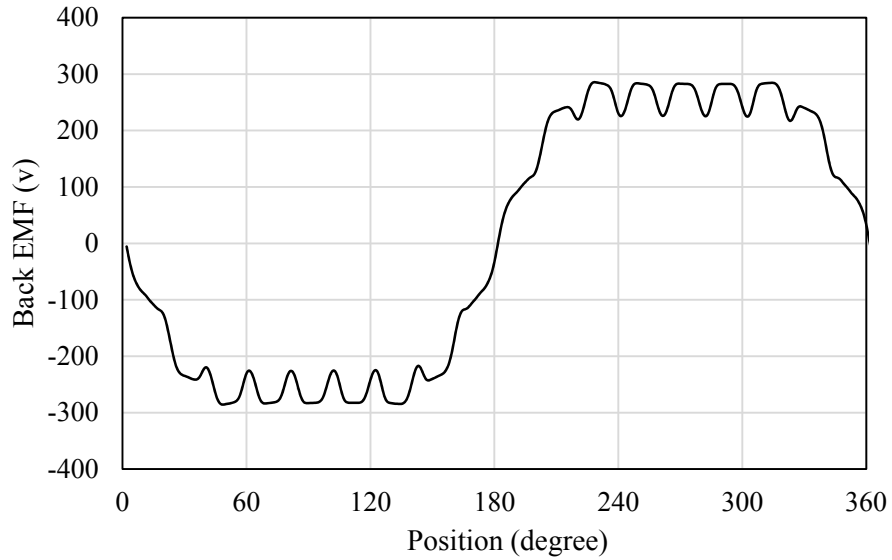


Fig. 3.26 Simulated back EMF for the 27-slots machine with the preliminary rotor design

*1) Pole arc reduction*

The back EMF harmonics in surface PMSMs can be reduced by shaping the magnet surface and optimizing the magnet pole arc angle so that the rotor magnets would produce a more sinusoidally distributed air gap flux density. For the tangentially magnetized configuration in Fig. 3.13, the effective pole arc can be also controlled by changing the width of the rib above the magnet, as illustrated in Fig. 3.27.

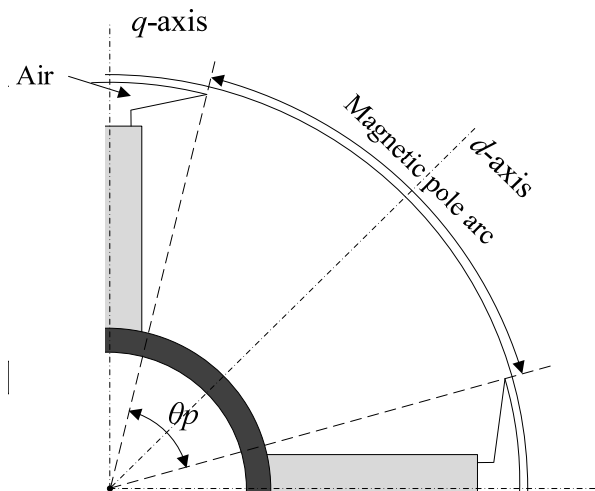


Fig. 3.27 Illustration of pole arc reduction in tangentially magnetized PMSM

Unlike the conventional radial designs, the pole arc in the tangentially magnetized configuration is reduced while keeping the magnet surface constant. Therefore, the magnet flux is squeezed through smaller area of rotor surface. This increases the air gap flux density fundamental component. Table 3.5 contains the key FEA simulation results for machines with different pole arc angles. It can be seen that reducing the magnetic pole arc led to an increase in the back EMF fundamental component. In addition, the barrier above the magnet limits the  $q$ -axis flux and improves the machine saliency ratio. Therefore, more reluctance torque can be produced.

Table 3.5 Comparison of the machine performance with different pole arc angles

	Initial design	$\theta_p = 75^\circ$	$\theta_p = 60^\circ$	$\theta_p = 45^\circ$
Fundamental Back EMF (v)	316.0	328.5	348.8	356.7
Saliency ratio ( $L_d/L_q$ )	1.48	1.48	1.60	1.88
Output torque (N.m)	38.55	40.62	43.89	46.06
Magnetization current (A)	30.25	30.68	31.30	39.19

While it clear that reducing the pole arc angle enhances the machine torque capability, the FEA simulation results in table 3.5 show that smaller pole arcs are also associated with an increase in the magnetization current requirement, as the wider barrier above the magnet obstructs the armature d axis flux. Therefore, more armature current is required to magnetize the magnets. As shown in Table 3.5, the  $45^\circ$  pole arc design requires about 30% more magnetization current compared to the initial design. This may lead to an oversized inverter. On the other hand, the  $60^\circ$  pole arc machine can deliver 14% more output torque than the initial design, and it only requires 3.5 % more magnetization current. Fig. 3.28 compares the back EMF waveform of the  $60^\circ$  pole arc rotor with the

initial rotor design, and the harmonic content of the two waveforms are shown in Fig. 3.29. It is clear that reducing the pole arc suppresses some of the higher harmonics and increases the back EMF fundamental component. Therefore, the machine pole arc is reduced to  $60^\circ$  in order to enhance the machine torque density and to reduce the back EMF harmonics.

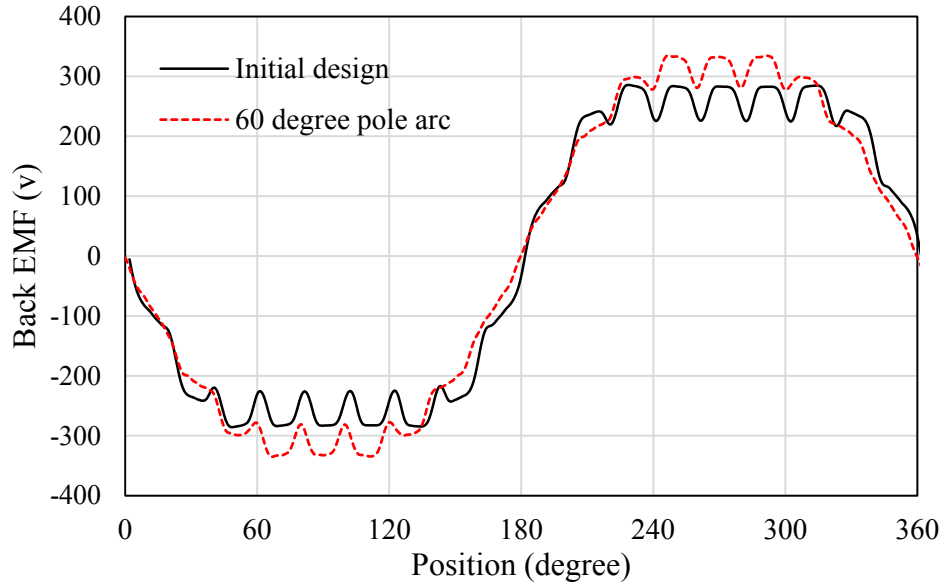


Fig. 3.28 Effect of the effective pole arc angle on the back EMF waveform

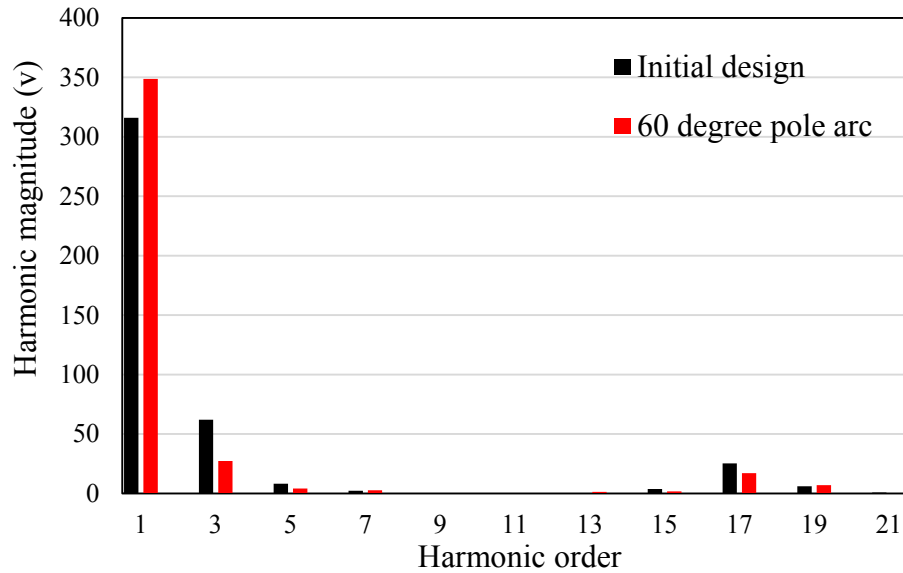


Fig. 3.29 Effect of the effective pole arc angle on the back EMF harmonics

## 2) Uneven air gap

To further reduce the back EMF harmonics, the air gap length is minimized at the  $d$ -axis and increased until it reaches its maximum length at the  $q$ -axis, as illustrated in Fig. 3.30. This is accomplished by shifting the pole arc center up towards the rotor surface. Fig. 3.31 compares the air gap flux density for a uniform air gap design with the uneven air gap rotor design. It is clear that the gradual reduction of the air gap length produces more sinusoidal air gap flux density distribution. In addition to the apparent improvement in the back EMF waveform, the reduction of rotor flux harmonics also leads to a reduction in the machine core losses and improvement in the machine efficiency.

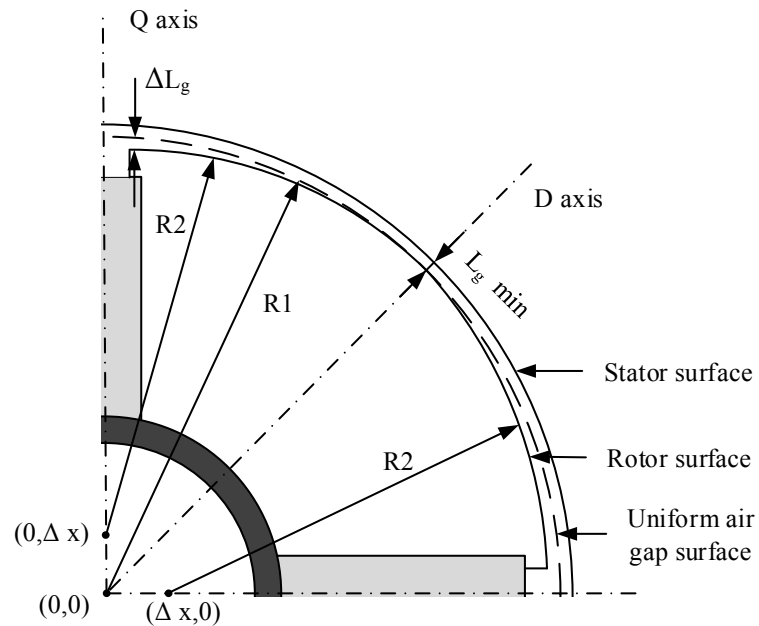


Fig. 3.30 Illustration of the uneven air gap design

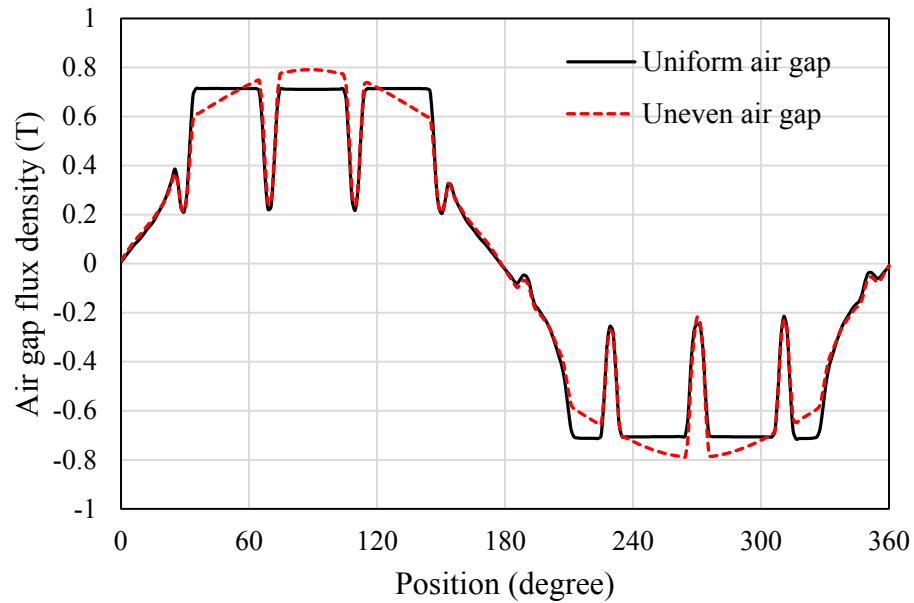


Fig. 3.31 Comparison of the simulated air gap flux density for a rotor with uniform air gap and a rotor with  $\Delta L_g = 0.35 \text{ mm}$

### 3) Additional rotor barriers

The  $q$ -axis inductance can be reduced by adding barriers in the rotor as shown in Fig. 3.32. This increases the saliency ratio, and therefore the reluctance torque component, as shown in the FEA simulations results in table 3.6. In addition, it limits the  $q$ -axis flux at full load. This reduces the machine core losses and improves the machine efficiency. On the other hand, the added barriers increase the required magnetization current, as the reduction of rotor steel increases the rotor flux density level during magnetization. Therefore, more armature current has to be applied in order to overcome the reluctance of the rotor steel. This may require increasing the machine inverter rating.

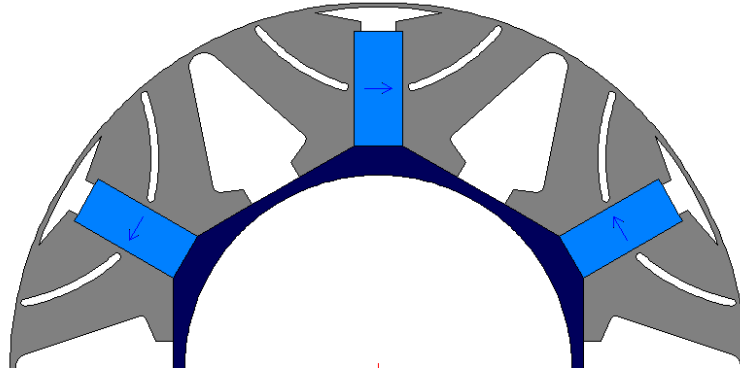


Fig. 3.32 Rotor design with additional barriers

Table 3.6 Effect of the additional barriers on the machine performance

	One barrier per pole	Three barriers per pole
$L_d$ @ full load (H)	0.0418	0.0435
$L_q$ @ full load (H)	0.0281	0.0255
Saliency ratio ( $L_d/L_q$ )	1.49	1.71
Average reluctance torque (N.m)	6.96	9.18
Iron loss (Watt)	111.80	95.31
Magnetization current (A)	32.74	34.31

#### 4) Modified barrier design

The amount of rotor steel is increased by re-shaping the main barrier so that the barrier edge would have a shape similar to the  $d$ -axis flux lines, as shown in in Fig. 3.33. Also, the width of the additional barriers is increased in order to maintain the machine saliency ratio. The modified design reduces the flux density level in the rotor steel, which leads to a reduction in the magnetization current. Fig. 3.34 compares the back EMF of the modified rotor with the original design. It is clear that the rotor modifications led to a considerable improvement in the back EMF waveform. Table 3.7 shows the evolution of

the machine performance throughout each of the rotor design modification steps. It can be seen that the machine performance is enhanced by each of the design modifications, and the modified rotor design has higher efficiency and output torque compared to the original design with a small increment in the magnetization current.

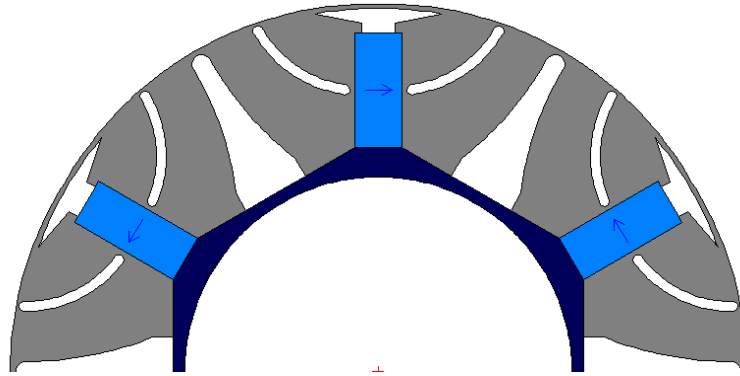


Fig. 3.33 Proposed modified rotor design

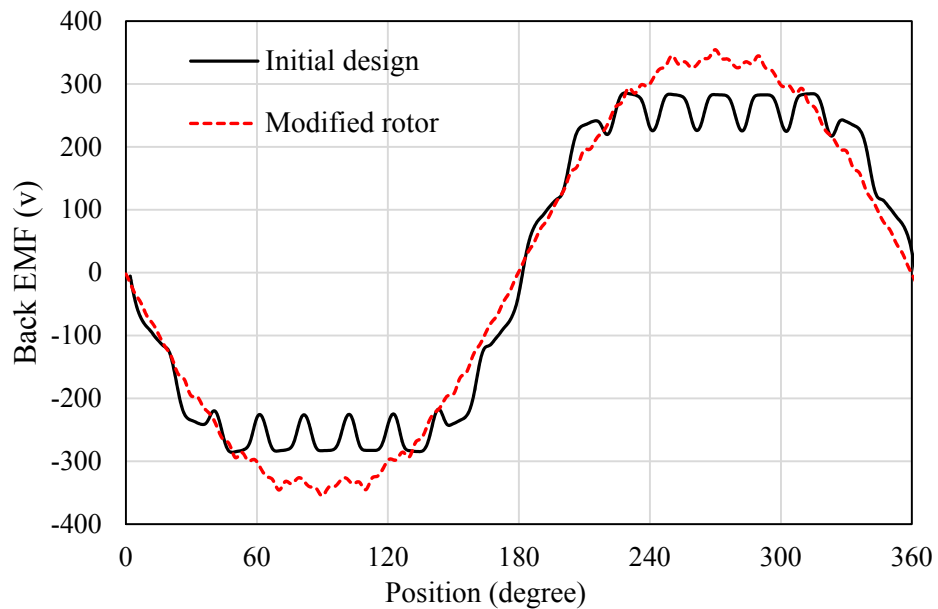


Fig. 3.34 Comparison of the simulated back EMF for the initial and modified rotor designs

Table 3.7 Evaluation of the machine performance after each of the proposed rotor modifications

	Initial design	Reduced pole arc	Uneven air gap	Additional barriers	Modified rotor
Output torque (N.m)	38.55	43.89	43.78	45.04	45.73
Iron loss (Watt)	141.08	125.93	111.8	95.31	93.42
Efficiency %	94.79	95.54	95.67	95.95	96.03
Magnetization current (A)	30.25	31.30	32.74	34.31	32.48

### 5) Magnet dimensions

The magnet in the proposed rotor configuration should be of sufficient thickness to operate above the demagnetization curve knee at no-load. The magnet length should also be designed to provide the desired air gap flux density. The required magnet dimensions can be obtained analytically, as shown in section 3.2.3. In this section, the effect of magnet dimensions on the magnetization current is analyzed.

FEA simulations are performed for machine with different magnet thickness. The magnet magnetization curves in Fig. 3.35 show that the current required to reach the magnet saturation flux density of 1.3 T is almost linearly proportional to the magnet thickness. Therefore, the magnet should be just wide enough to avoid irreversible demagnetization, but further increase of the magnet thickness will result in an undesirable increase of the magnetization current.

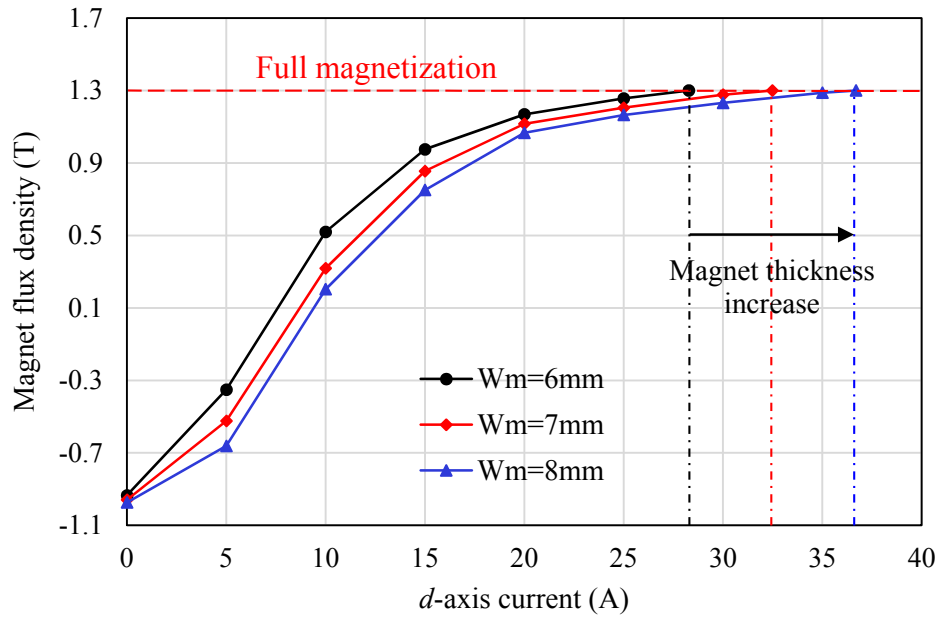


Fig. 3.35 Magnetization characteristics for machines with different magnet thickness

It is found from the previous analysis that most of the armature magnetizing MMF is utilized in the steel reluctance. The stator flux density level and therefore its reluctance can be controlled by changing the length of the magnet. However, the reduction of the magnet length leads to a corresponding reduction in the air gap flux density, which results in reducing the machine output torque. Fig. 3.36 shows the simulated output torque and magnetization current for different magnet lengths. It can be seen that the output torque decreases linearly with the magnet length reduction. On the other hand, the magnetization current decreases in a much steeper rate, almost decaying exponentially with the magnet length reduction. Therefore, changing the magnet length can be an effective way for controlling the magnetization current of variable flux machines.

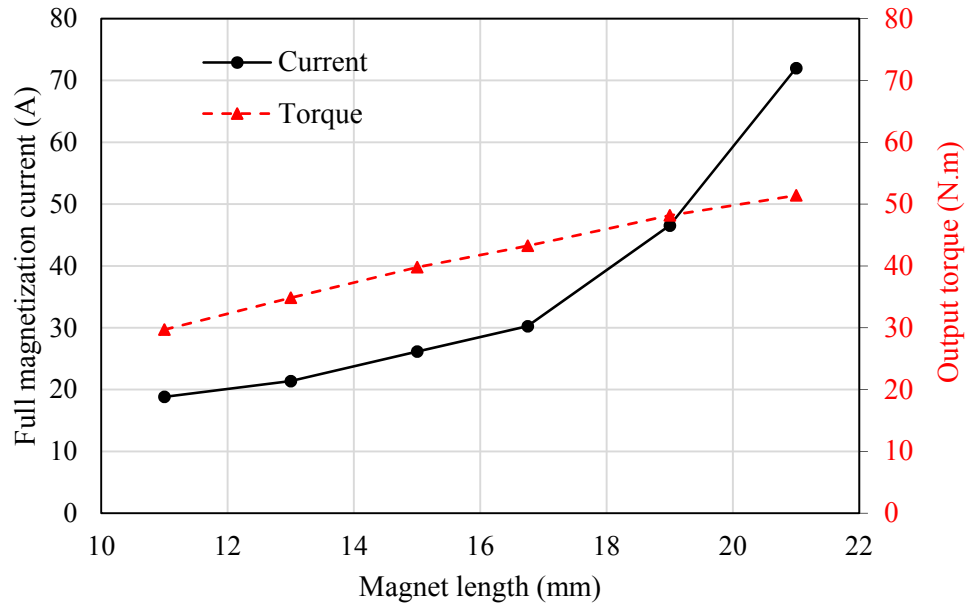


Fig. 3.36 Simulated full magnetization current and output torque for machines designed with different magnet lengths

#### 6) Rotor structural analysis

The mechanical stresses and deformation of the rotor design shown in Fig. 3.33 are investigated using structural FEA. Only mechanical centrifugal force is considered, as it is the dominant source of mechanical stress at high speeds [37-39]. Fig. 3.37 shows the mechanical stress distribution in the rotor at 10,000 rpm. It can be seen that the stress is concentrated at the bridges above the additional barriers. Fig. 3.38 shows the variation of the maximum rotor stress with the rotor speed. The maximum mechanical stress is lower than the steel yield strength for speeds lower than 11,500 rpm. Below that speed, the rotor steel will deform elastically and it will return to its original shape when the mechanical stress is removed. In order to ensure the mechanical strength of the rotor, the maximum allowable mechanical stress in the rotor steel is set to 233 Mpa, which is 1.5 times lower than the steel yield strength. This corresponds to a maximum rotor speed of 9250 rpm.

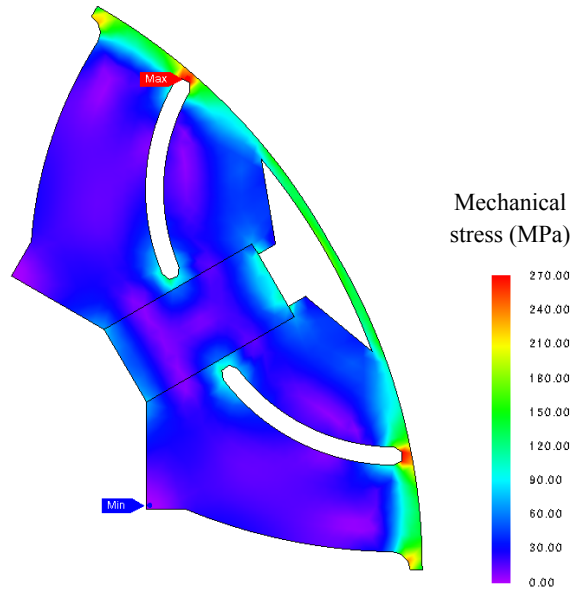


Fig. 3.37 Rotor stress distribution at 10,000 rpm

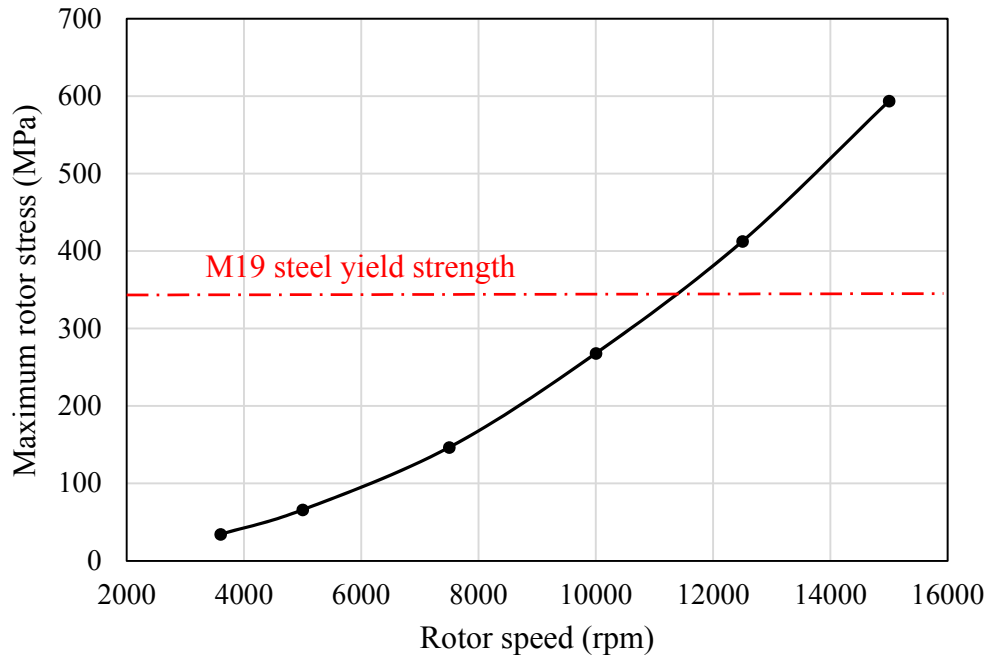


Fig. 3.38 Maximum stress in the rotor as a function of speed

The deformation of the rotor steel due to the centrifugal forces is shown in Fig. 3.39. Fig. 3.40 shows the maximum rotor displacement as a function of rotor speeds. It can be seen

that the maximum rotor displacement at the allowable speed range is much lower than the minimum air gap of 0.4 mm. Therefore, the resulting mechanical deformation will not affect the mechanical integrity of the machine.

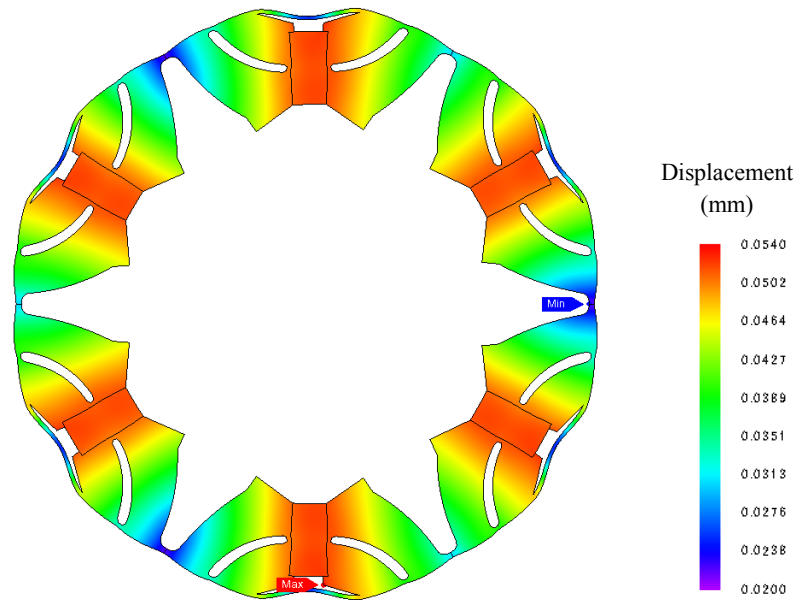


Fig. 3.39 Scaled rotor deformation at 10,000 rpm (scale = 1:100)

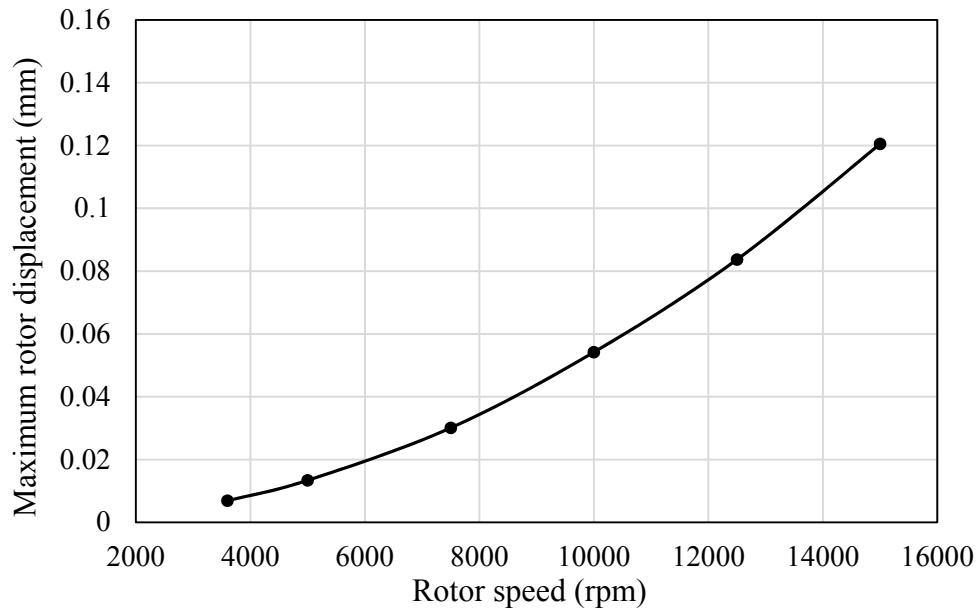


Fig. 3.40 Maximum displacement in the rotor as a function of speed

### 3.4 Analysis of the Machine Performance

#### 3.4.1 Torque-Speed Characteristics

The machine design methodology presented in the previous section is used to design a 7.5 hp variable flux machine prototype. The specifications of the designed machine are shown in table 3.8. FEA simulations are then performed in order to evaluate the machine performance over the whole speed range. One third of the designed machine is simulated in JMAG FEA software. The generated mesh for the simulated section contains 7690 mesh elements and 4284 mesh nodes.

Table 3.8 Final machine design specifications

Number of poles	6
Number of slots	27
Stator outer diameter (mm)	200
Axial length (mm)	120
Air gap length (mm)	0.4 - 0.75
Magnet width (mm)	7
Magnet length (mm)	14.2
Magnet material	Alnico 9
Steel material	M19G29
Saliency ratio ( $L_d/L_q$ )	1.6
DC bus voltage (v)	600
Rated current (A)	10
Output torque (Nm)	36.8
Demagnetization current (A)	7.07
Magnetization current (A)	19.65

The torque-speed curves are obtained at different magnetization levels using JMAG-RT. FEA simulations are first performed at various magnitudes and phase angles of the armature phase current. At each operating condition,  $L_d$ ,  $L_q$ , and the flux linkage  $\lambda$  are calculated based on the FEA results. The output torque can then be obtained by,

$$T_e = \frac{3p}{2} [\lambda I_q + (L_d - L_q) I_d I_q] \quad (3.4)$$

At low speeds, the torque-speed curves are simulated using maximum torque per Ampere technique, where the current magnitude is fixed and its phase angle is varied until maximum torque is obtained. When the machine reaches its base speed, the voltage required to deliver the rated current at the optimum torque angle becomes higher than inverter voltage capability. The required  $d$  and  $q$  axes voltages ( $V_d$  and  $V_q$ ) at a certain speed ( $\omega$ ) can be calculated by,

$$V_d = RI_d - \omega L_q I_q \quad (3.5)$$

$$V_q = \lambda \omega + RI_q + \omega L_d I_d \quad (3.6)$$

The base speed ( $\omega_{base}$ ) at which the required voltage equates the maximum inverter voltage ( $V_m$ ) can be determined analytically by,

$$\omega_{base} = \frac{V_m}{\sqrt{(L_q I_q)^2 + (\lambda + L_d I_d)^2}} \quad (3.7)$$

When the machine exceeds the base speed, the torque speed-curves are calculated using maximum power technique, where both the current magnitude and phase angle are varied in order to maximize the machine power at each speed, while maintaining the required voltage below the drive capability.

Fig. 3.41 shows the torque-speed curves of the machine when the magnet is operating at different magnetization levels. It was expected that the machine base speed would be doubled if the magnet flux is halved. However, the FEA simulation results in Fig. 3.41 show that reducing the magnetization level to 50% increases the machine base speed by only 22%. This can be explained as follows; the input armature voltage for each magnetization level is utilized to overcome the magnet induced back EMF and the voltage drop across the winding impedance. The utilization of the input voltage at different magnetization levels is shown in Fig. 3.42. It is clear that the back EMF is linearly proportional to the magnet flux. On the other hand, the winding voltage drop is almost constant for different magnetization levels with a slight reduction at the 100% magnetization due to the steel saturation effects. Even though the back EMF at 50% magnetization is half of the fully magnetized machine back EMF, the inverter still has to supply the high voltage drop across the winding impedance. The required input voltage to overcome these two components is 22% lower than the required input voltage for a fully magnetized machine. This leads to the extension of the base speed by only 22%, as shown in Fig. 3.41.

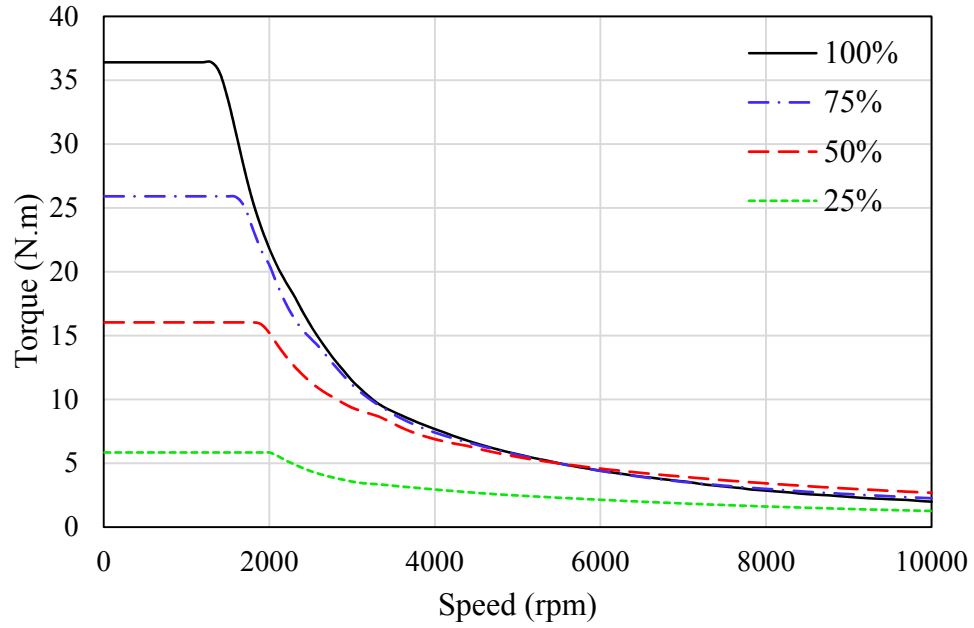


Fig. 3.41 Torque-speed curves for different magnetization levels

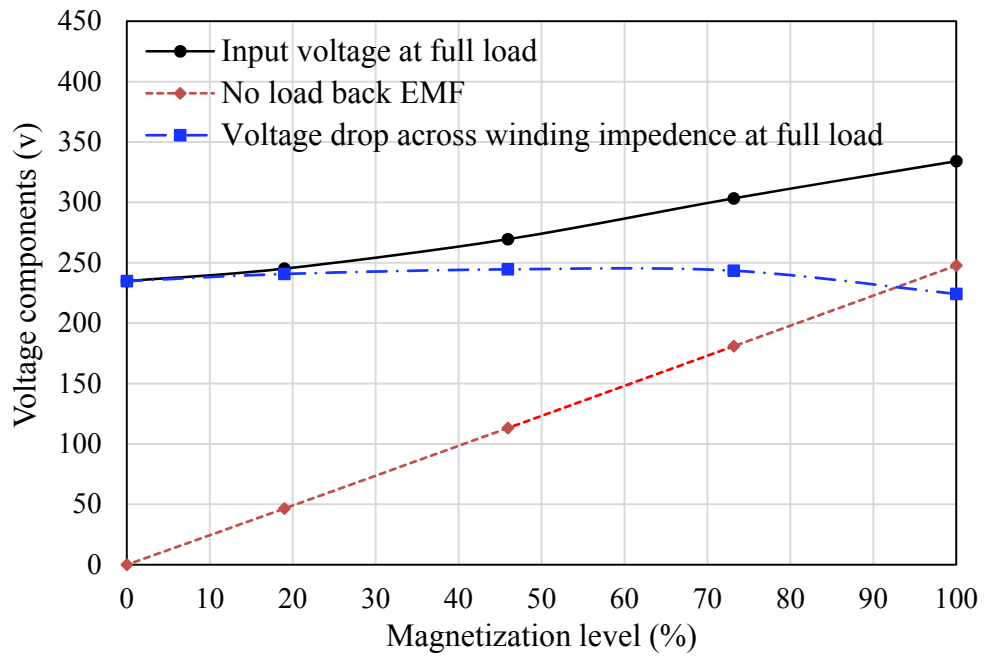


Fig. 3.42 Variation of voltage components with the magnetization level

The corresponding power-speed curves for different magnetization levels are also shown in Fig. 3.43. It can be seen that the machine power decreases beyond base speed, as the employed control technique reduces the armature current at high speeds, as shown in the simulated currents in Fig. 3.44.

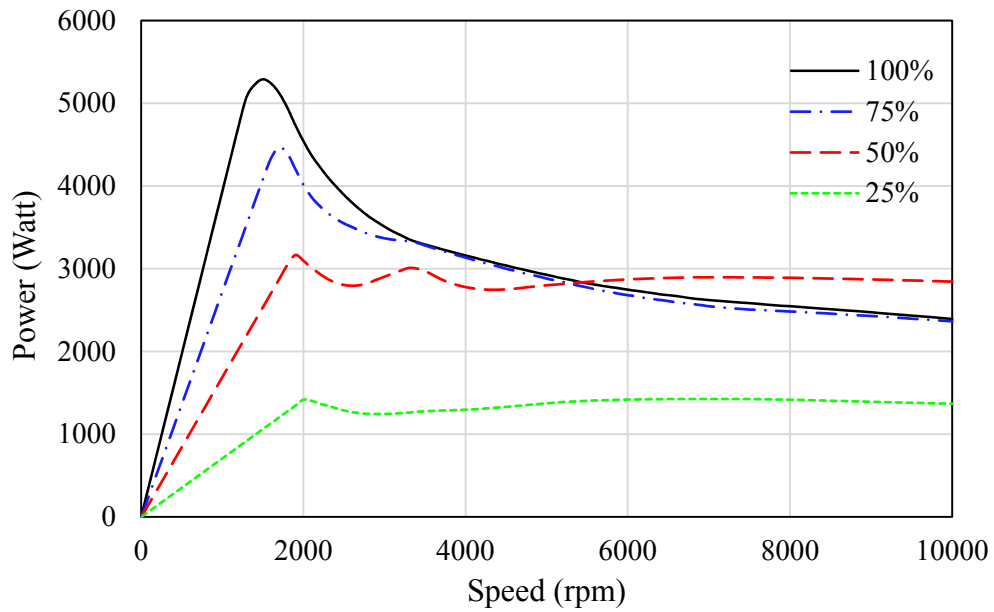


Fig. 3.43 Simulated power-speed curves for different magnetization levels

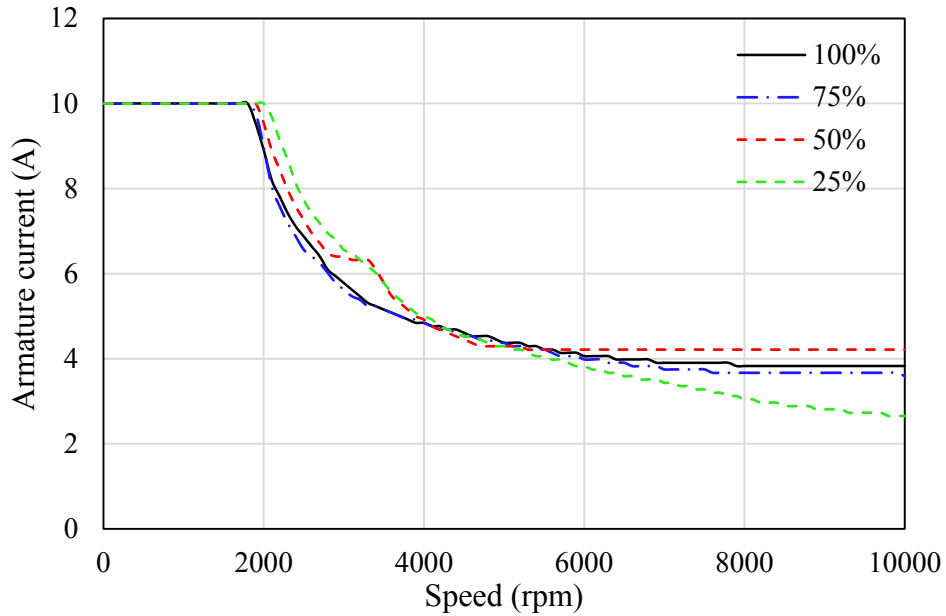


Fig. 3.44 Simulated armature currents for different magnetization levels

### 3.4.2 Efficiency Analysis

The efficiency maps for different magnetization levels are also obtained using JMAG-RT. The copper and iron losses are first calculated for each simulated current magnitude, phase angle and speed. The current magnitude and phase angle are then varied in order to maximize the efficiency at each point below the torque-speed curve. Figs. 3.45-3.48 show the simulated efficiency maps when the machine is operating at 100%, 75%, 50% and 25% magnetization. It can be seen that the high efficiency region is shifting for different magnetization levels, as the 100% magnetization can achieve high efficiency at the high torque-low speed region, while this machine has lower efficiency at high speeds. On the other hand, the high efficiency region shifts to higher speeds when the magnetization level is reduced.

The total machine loss distribution for different magnetization levels is shown in Figs 3.49-3.52. It can be seen that the machine losses at high speeds can be significantly reduced by using lower magnetization levels. This is mainly attributed to the reduction of iron loss which is the dominant loss component at high speeds. The iron loss distribution for different magnetization levels is shown in Figs. 3.53-3.56. It is clear that reducing the magnet flux at high speeds can result in significant reduction of the steel iron losses.

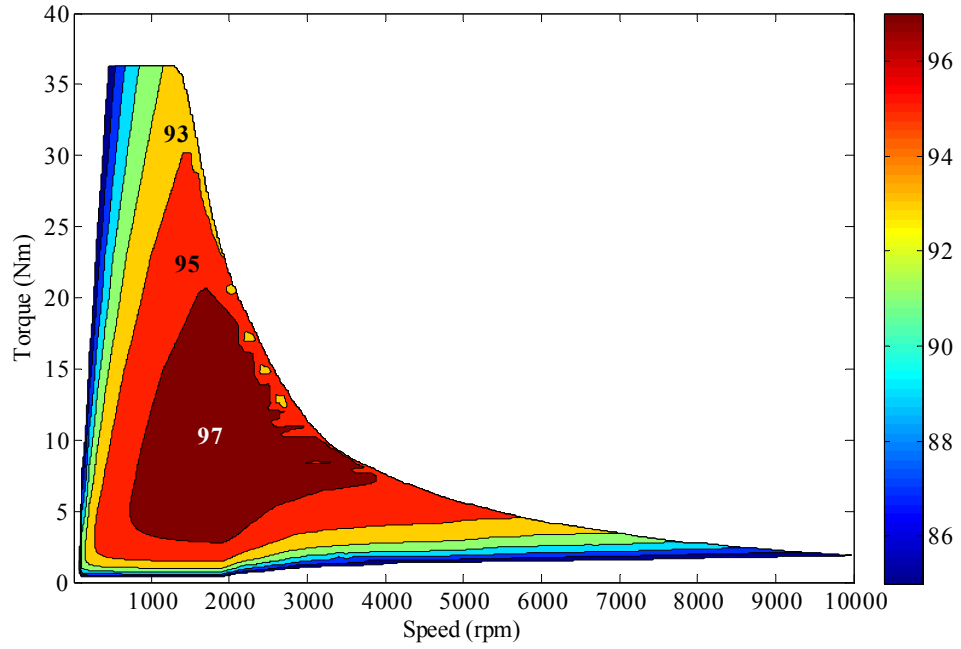


Fig. 3.45 Efficiency map at 100% magnetization

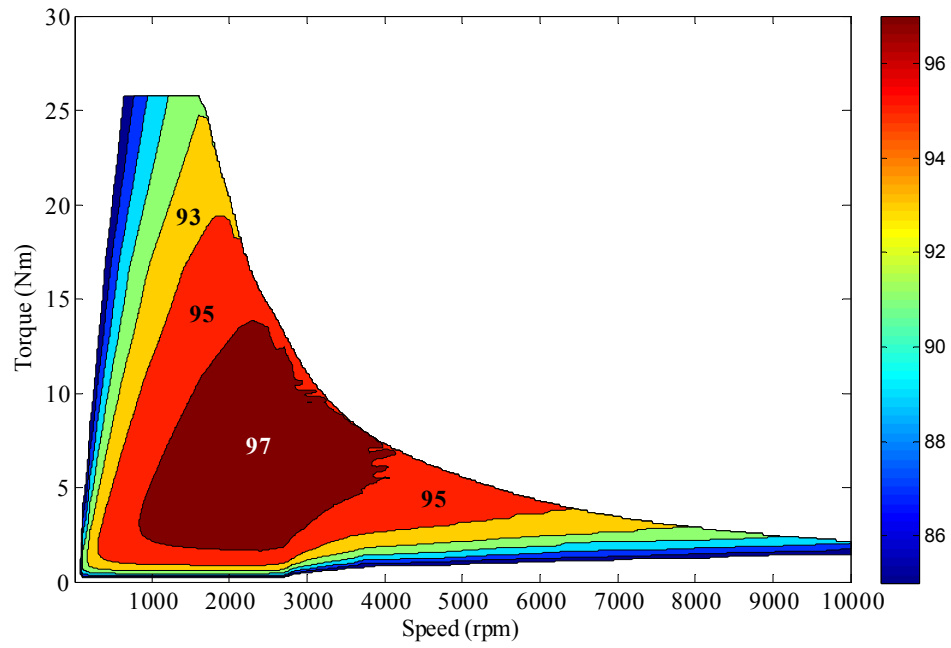


Fig. 3.46 Efficiency map at 75% magnetization

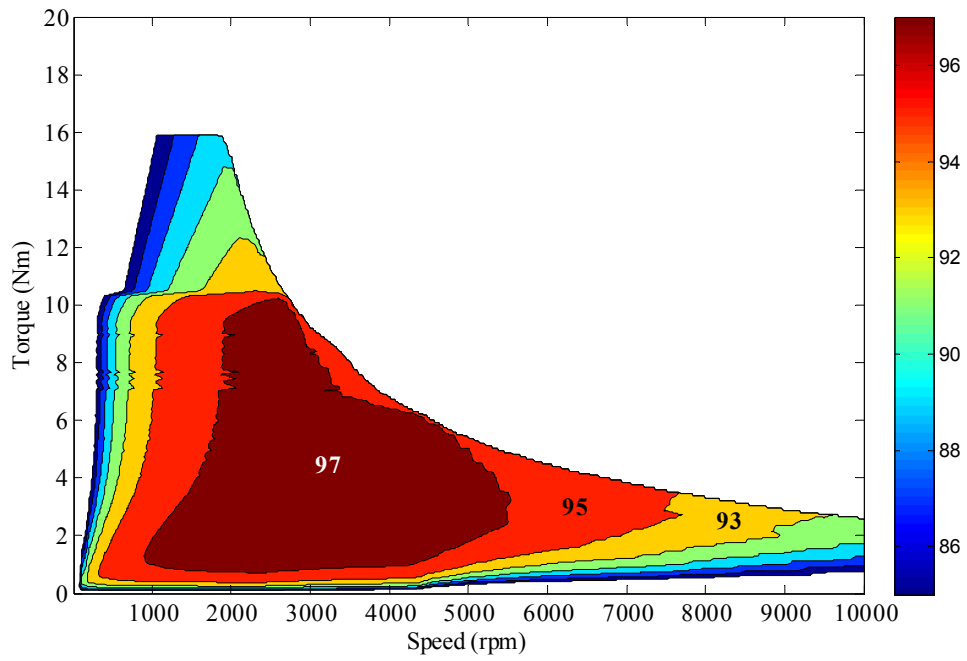


Fig. 3.47 Efficiency map at 50% magnetization

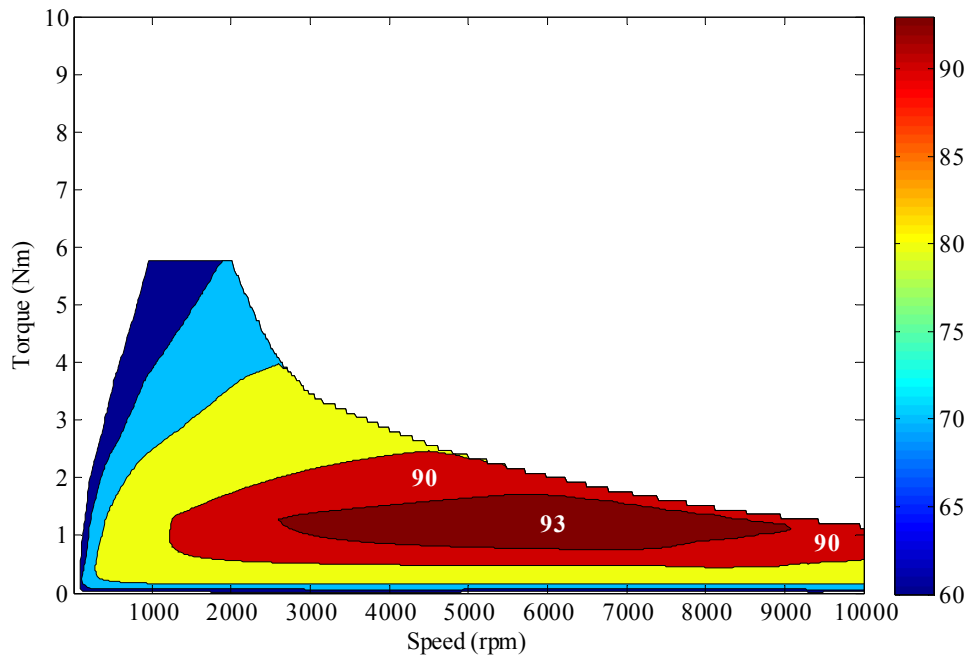


Fig. 3.48 Efficiency map at 25% magnetization

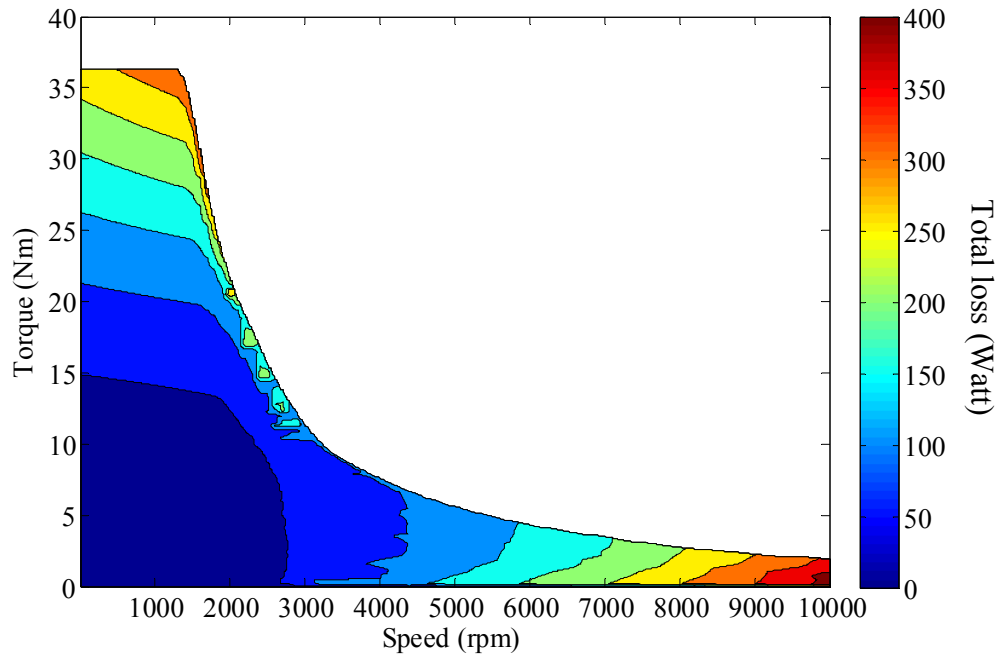


Fig. 3.49 Total machine loss distribution at 100% magnetization

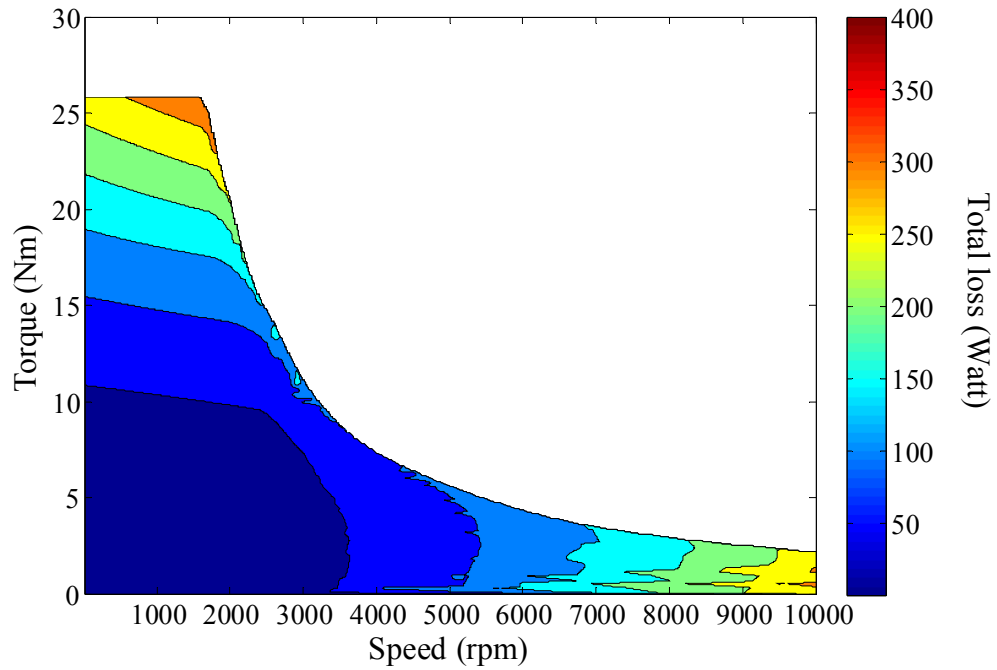


Fig. 3.50 Total machine loss distribution at 75% magnetization

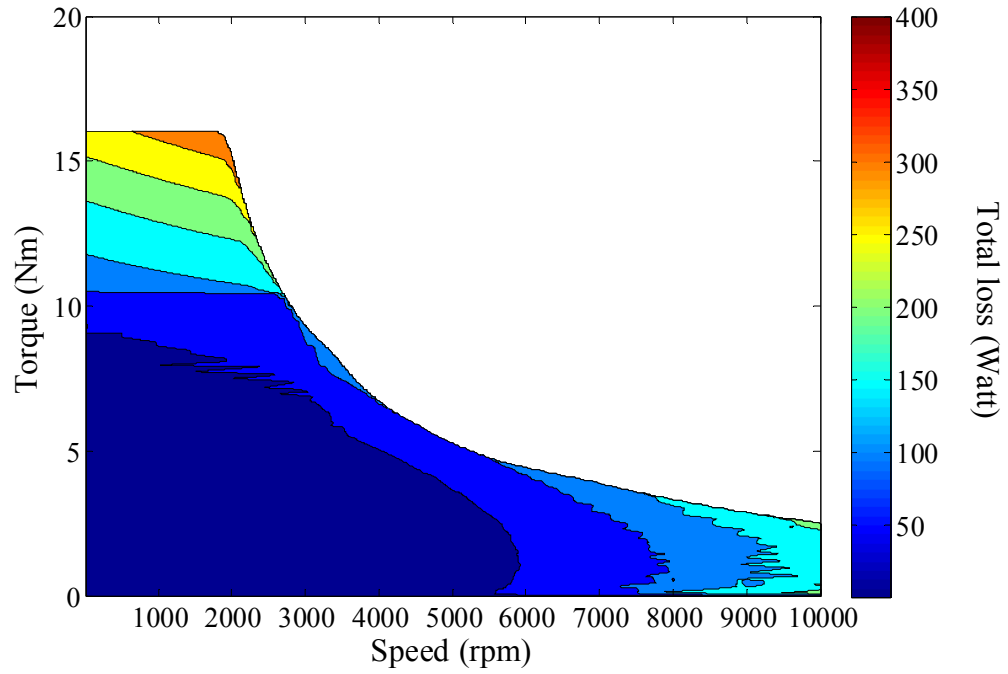


Fig. 3.51 Total machine loss distribution at 50% magnetization

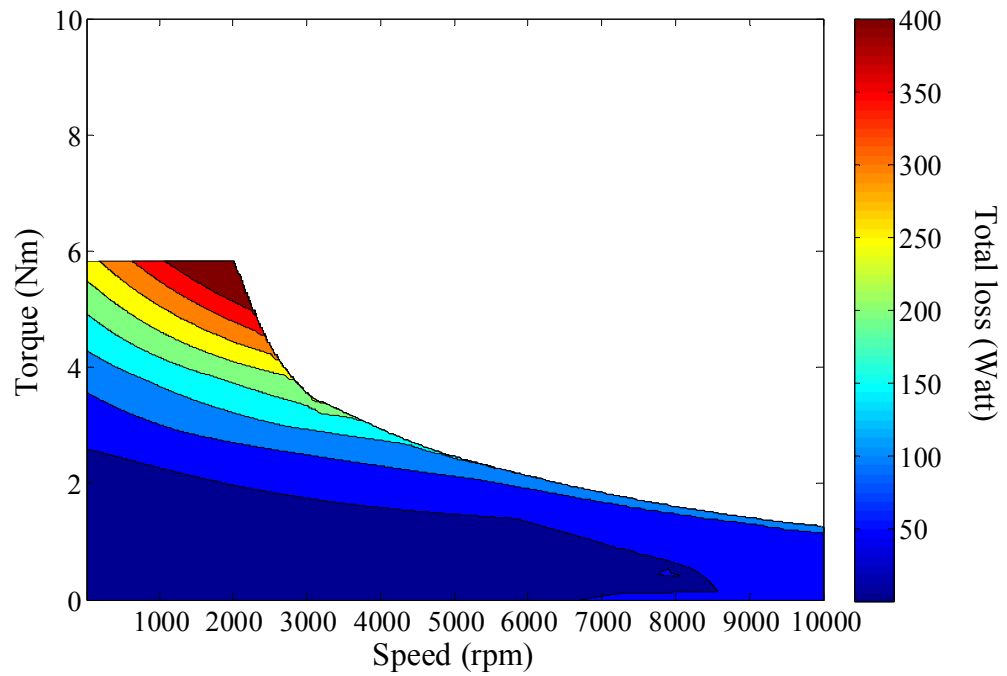


Fig. 3.52 Total machine loss distribution at 25% magnetization

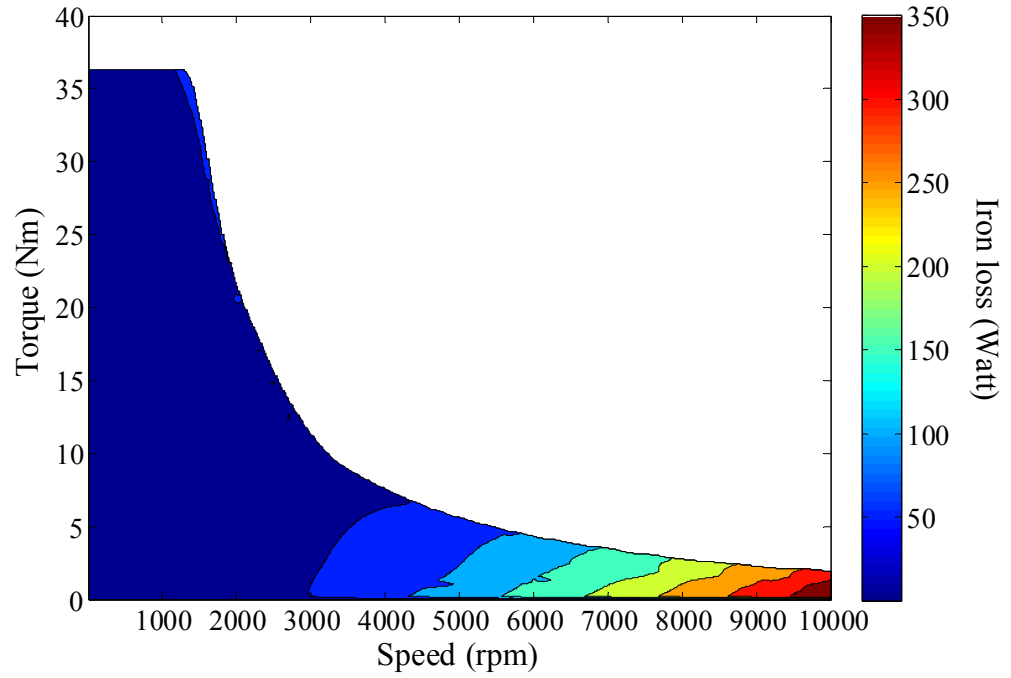


Fig. 3.53 Iron loss distribution at 100% magnetization

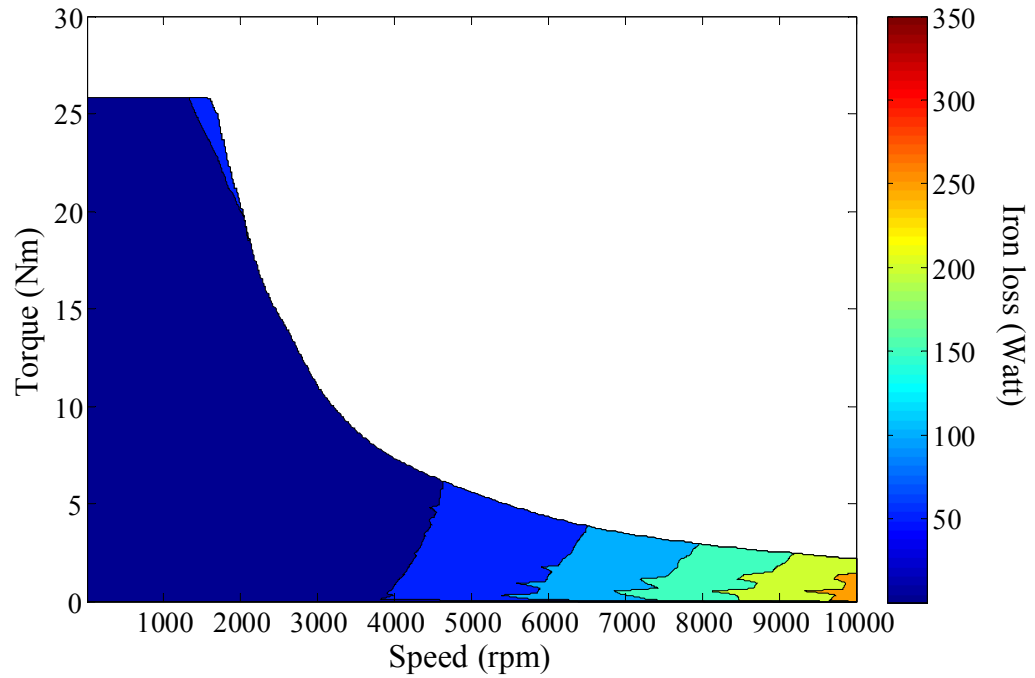


Fig. 3.54 Iron loss distribution at 75% magnetization

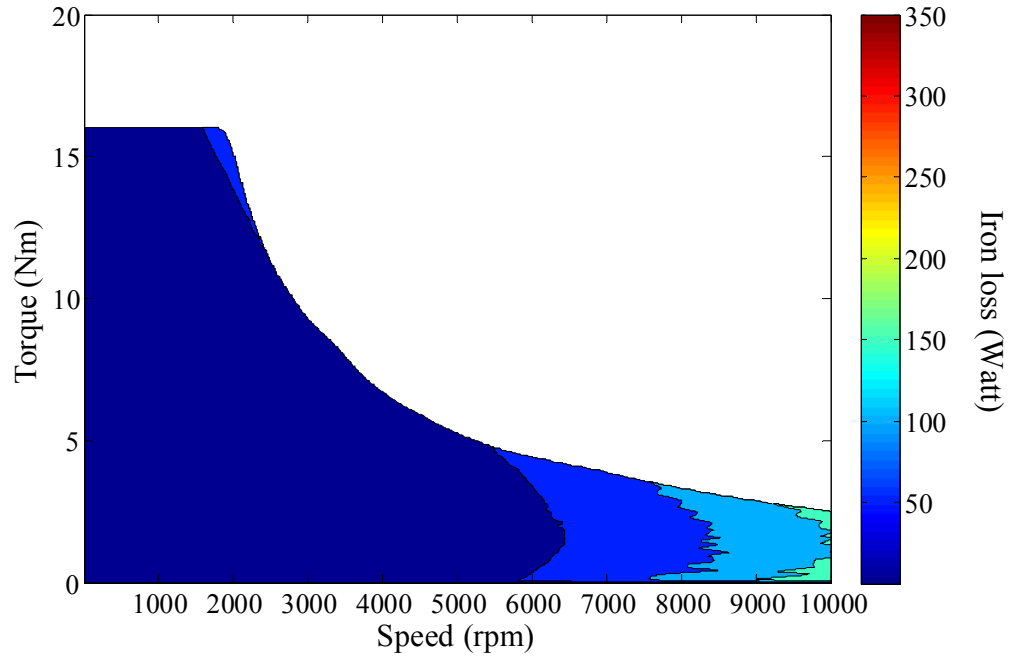


Fig. 3.55 Iron loss distribution at 50% magnetization

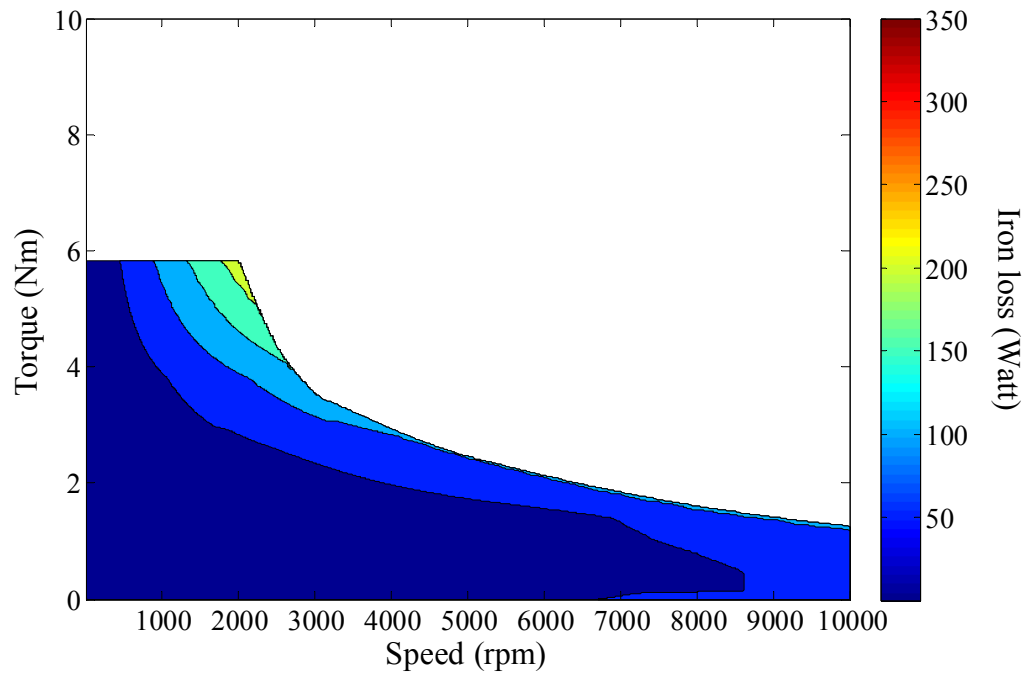


Fig. 3.56 Iron loss distribution at 25% magnetization

The efficiency maps in Figs. 3.45-3.48 are compared, and the magnetization level that can provide the highest efficiency is selected for each operating condition and considered the optimum magnetization level. Fig. 3.57 shows the regions at which each magnetization levels is used. It can be seen that the optimum magnetization level should be dependent on the operating point inside the torque-speed envelope. The efficiency map of the machine operating with the optimum magnetization levels is shown in Fig. 3.58. It is clear that this machine has high efficiency throughout a larger torque-speed region compared to the efficiency map of the constant flux permanent magnet machine in Fig. 3.45. The efficiency improvements due to the variation of the magnetization levels are shown in Fig.3.59. It is clear that changing the magnet flux can result in significant energy savings at the high speed and low torque region.

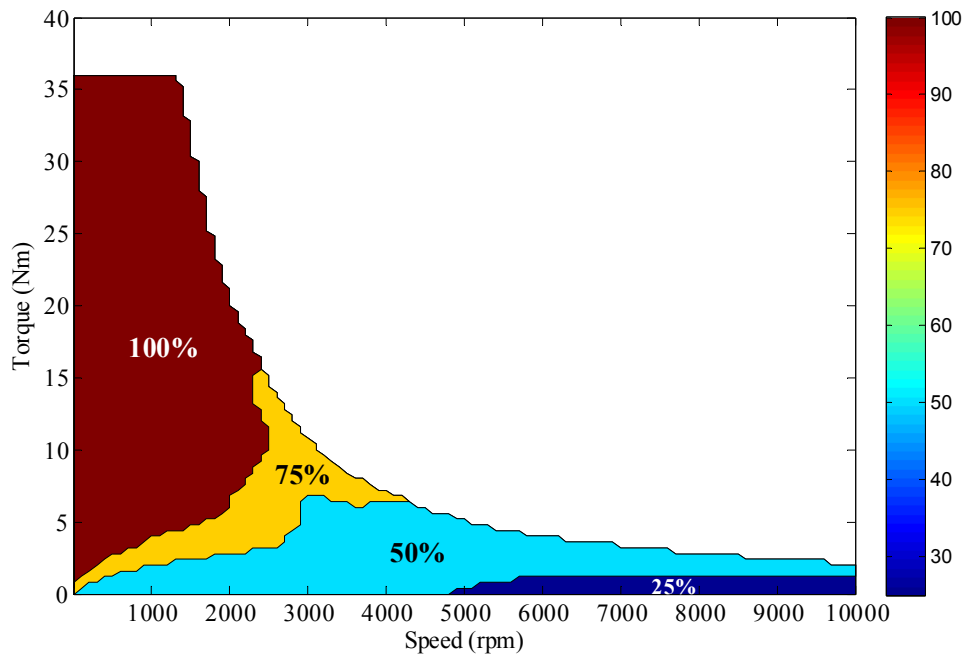


Fig. 3.57 Distribution of the optimum magnetization level

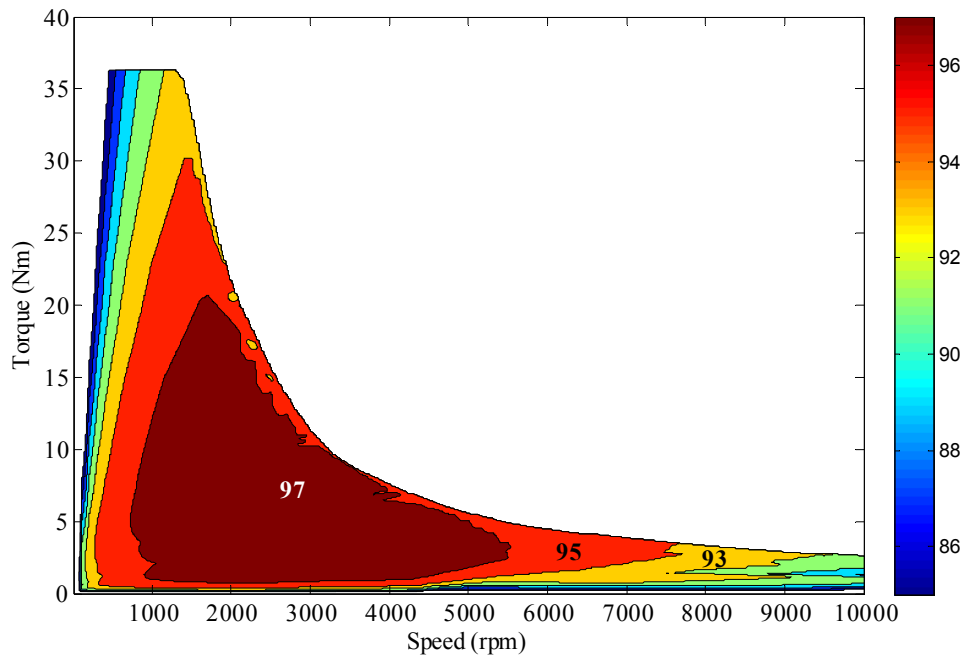


Fig. 3.58 Efficiency map when the optimum magnetization level is used

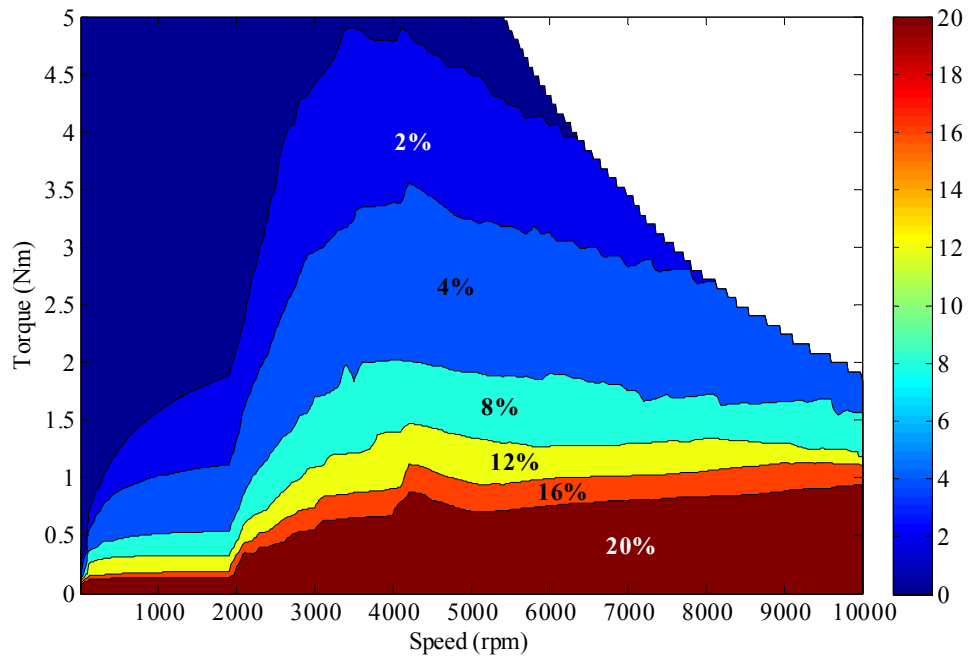


Fig. 3.59 Improvement in the machine efficiency at low torque when the optimum magnetization level is used

### 3.5 Experimental Validation

In order to verify the performance of the designed variable flux machine, a prototype of the machine specified in table 3.8 was built. Fig. 3.60 shows the machine at different stages of assembly. The magnet insertion process in the rotor steel was quite simple, as the magnets were inserted in a demagnetized state, as they can be magnetized later after the motor assembly by the armature winding.

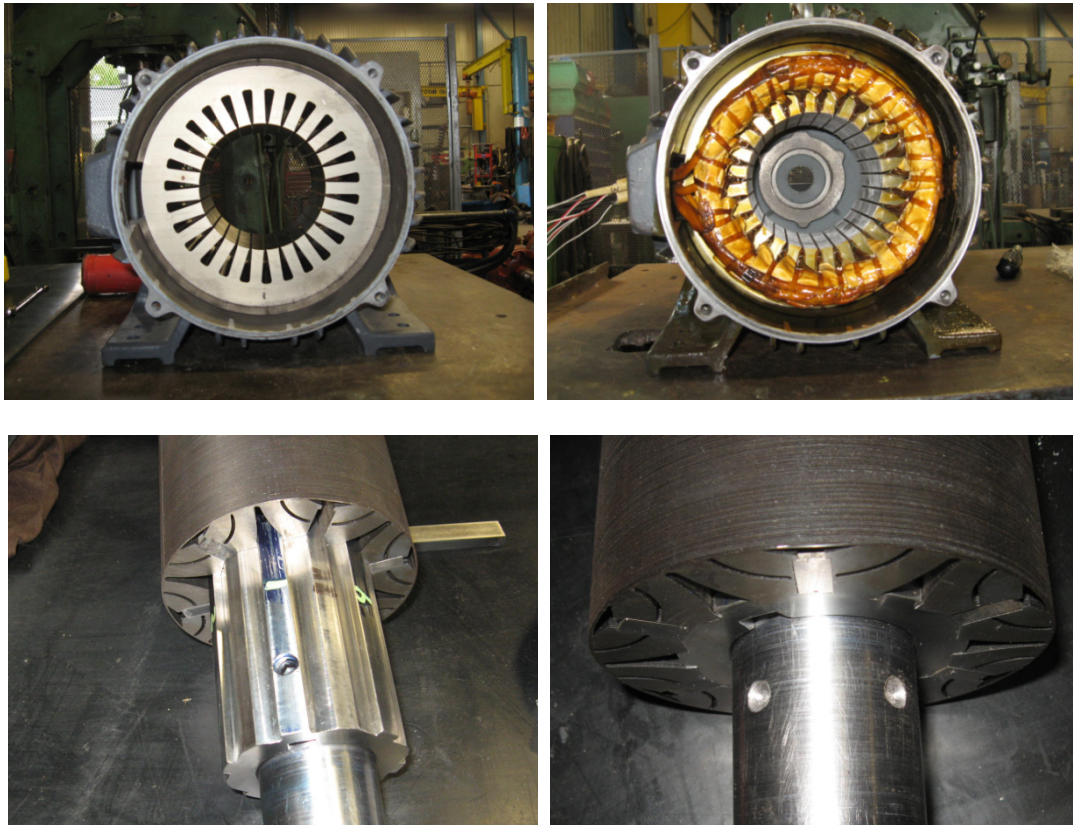


Fig. 3.60 Machine prototyping

The magnets are then magnetized by applying magnetizing  $d$ -axis current pulses. The back EMF is measured after each pulse is released in order to determine the machine flux linkage. The magnitude of the applied pulses is then increased until the magnets are saturated. Fig. 3.61 shows the changes in the magnet flux linkage with the magnetization pulse amplitude. It can be seen that full magnetization can be achieved with a magnetization current of about 25 A. The full magnetization current determined using FEA can allow the machine to reach about 95% of the full magnetization level. Fig. 3.62 compares the measured and FEA simulated back EMF when the magnets are fully magnetized. The measured back EMF waveform correlates well with the FEA predictions with a 6% reduction in the measured rms voltage. This deviation can be caused by the stresses introduced into the steel due to the lamination cutting. These stresses can affect the lamination properties and they were not considered in the FEA simulations. In addition, the reduction of the measured flux linkage can also be attributed to the actual magnet properties, which may differ from the simulated properties in FEA.

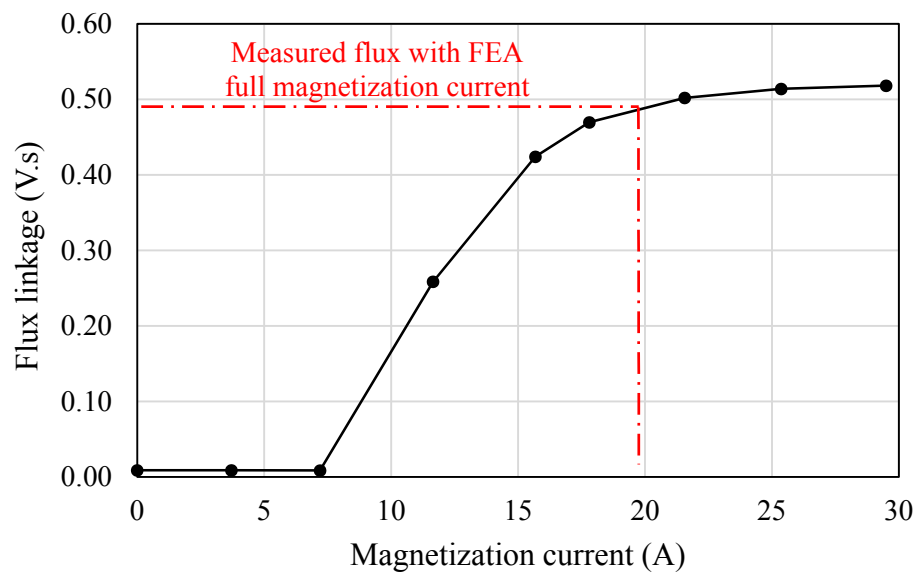


Fig. 3.61 Measured machine flux linkage after applying magnetizing current pulses

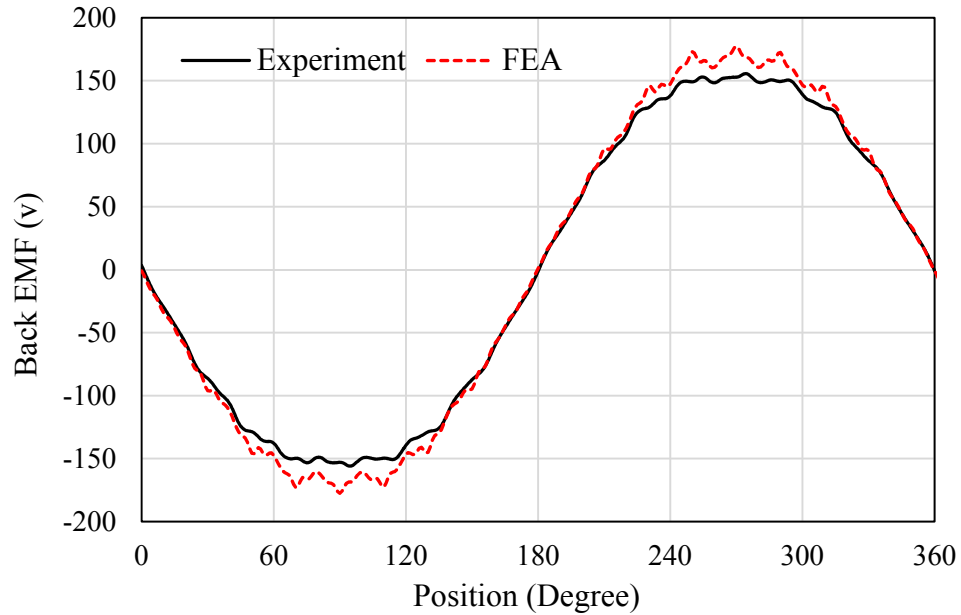


Fig. 3.62 Comparison of measured and simulated back EMF at 1000 rpm

Fig. 3.63 compares the measured and simulated machine output torque at different torque angles. The reduction of the magnet flux also led to a 6% reduction in the measured machine output torque compared to the FEA prediction. It can also be seen from Fig. 3.63 that the maximum torque is obtained at a torque angle around  $75^\circ$ . The applied magnetizing  $d$ -axis current component at this torque angle is utilized to produce a positive reluctance torque, as the machine is designed with inverted saliency ( $L_d > L_q$ ). This can be inferred from the PMSM torque components represented by equation (3.4). This magnetizing  $d$ -axis component also ensures stable operation of the permanent magnet even under high loading conditions.

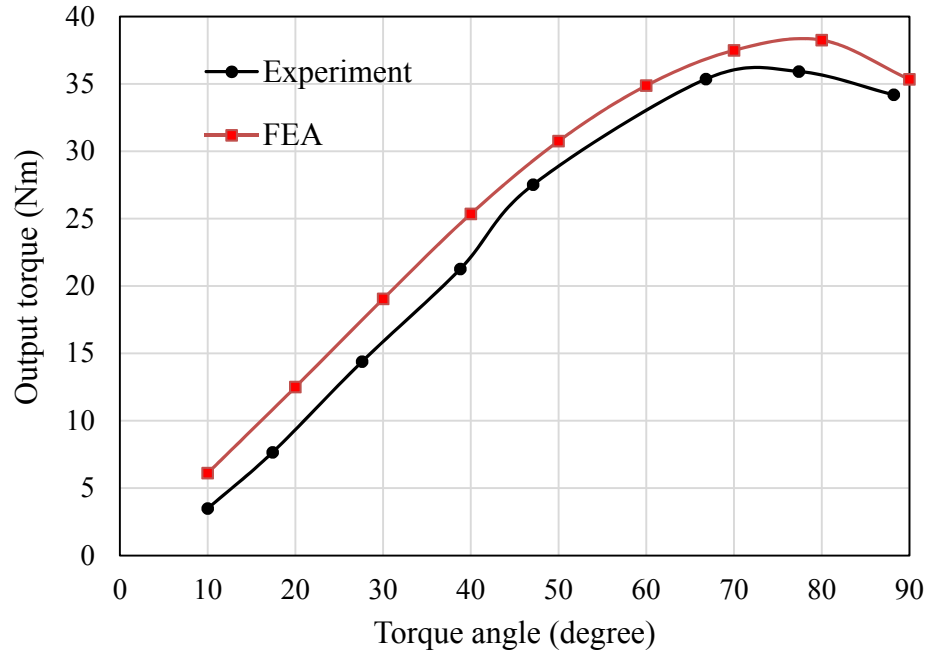


Fig. 3.63 Comparison of measured and simulated output torque at different torque angles

The current angle for maximum torque can be determined analytically by differentiating equation (3.4) [32]. However, the obtained analytical solution assumes that the machine inductances and flux linkages are constant, while the actual parameters depend on the armature current magnitude and phase angle. Therefore, it is more accurate to obtain the maximum torque angle using the simulated FEA results.

The demagnetization characteristics of the machine are then tested by applying demagnetizing current pulses of increasing magnitudes. The machine back EMF is measured after each pulse is released in order to evaluate the machine flux linkage. Fig. 3.64 compares the measured and FEA simulated demagnetization characteristics. It can be seen that the flux linkage of the tested machine can be controlled by changing the amplitude of the armature current pulse.

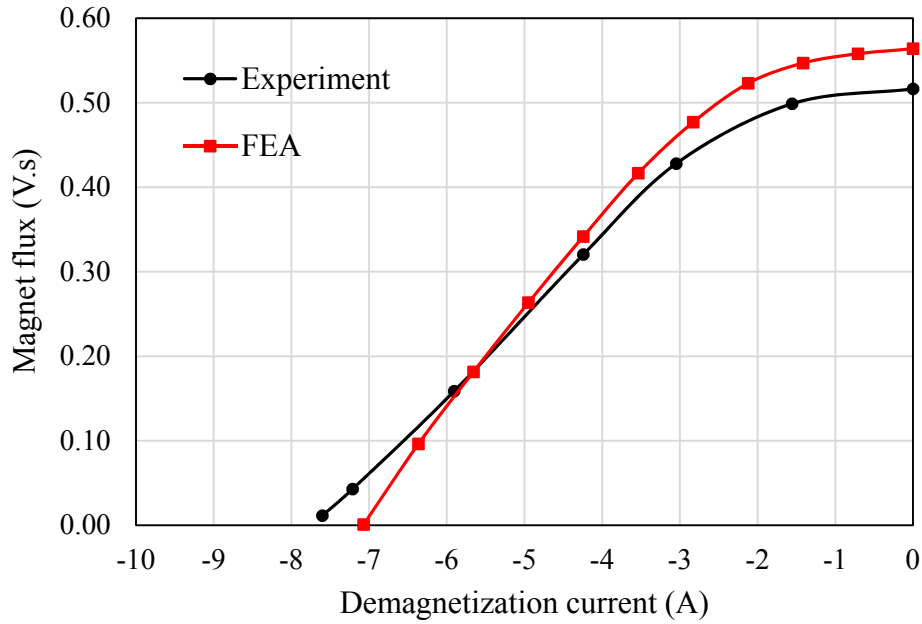


Fig. 3.64 Comparison of measured and simulated flux linkage after applying demagnetizing current pulses

### 3.6 Summary

A tangentially magnetized design for variable flux machines with Alnico magnets is proposed. The designed machine can deliver high torque density at the constant torque region, and it can achieve improved efficiency throughout a wide speed range by demagnetizing the magnets at high speeds by armature  $d$ -axis current pulses. The machine stator and rotor are also designed to reduce the magnetization current amplitude, thus reducing the machine inverter rating. A prototype of the designed machine is built, and the measured results confirm the validity of the machine design methodology.

## 4. HYSTERESIS LOSS PREDICTION IN ELECTRICAL MACHINES

### 4.1 Introduction

The design of high efficient electrical machines requires an optimization procedure for minimizing the machine losses. In order to achieve the optimum design, the machine core losses have to be calculated accurately for each candidate design. Therefore, it is essential to have an accurate and fast core loss model in order to optimize the machine within a convenient computation time.

One of the challenges of core loss prediction in electrical machines is the calculation of the hysteresis losses under distorted flux. The flux waveforms inside many machines, e.g., permanent magnet and switched reluctance machines are naturally non-sinusoidal and contain significant harmonic content and considerable DC component in some regions. Depending on the phase and magnitude of these harmonics, the resulting flux waveforms in the machine core may contain local flux reversals causing minor hysteresis loops to occur inside the main loop. The minor hysteresis loops can also be produced by the switching harmonics generated by power electronics inverters [20].

Many empirical formulas are presented in the literature to evaluate minor loop hysteresis losses [41]-[44]. These formulas can provide reasonable estimates for the hysteresis losses under certain conditions. However, they cannot be relied on to predict minor loop losses under a large variety of practically encountered flux waveforms in electrical machines. The only way these formulas can achieve accurate minor loop loss prediction

is to use variable coefficients based on a database of minor loop measurements [41], [45]. However, it is difficult to produce such a database experimentally, as the minor hysteresis loop losses are dependent on multiple factors. On the other hand, more accurate loss calculation can be achieved by simulating the hysteresis loop using advanced hysteresis models [20]. However, the use of these models may substantially increase the core loss computation time, as the hysteresis process has to be simulated for each of the machine mesh elements.

In this chapter, a hybrid model is proposed to calculate the hysteresis losses in electrical machines laminations exposed to non-sinusoidal flux waveforms. The model utilizes both analytical formulas and the Energetic hysteresis model to achieve accurate and computationally efficient hysteresis loss prediction.

## 4.2 Hysteresis Loss Measurement

Since it is practically impossible to predetermine the general properties of the minor loops generated in electrical machine laminations, the core loss model used should be able to calculate minor loop losses under all possible conditions. As illustrated in Fig. 4.1, the hysteresis loss caused by a minor loop in a certain magnetic material is dependent on four factors,

- 1) The magnitude of the minor loop  $\Delta B$ .
- 2) The position of the minor loop  $B_o$ .
- 3) The peak flux density of the major loop  $B_p$ .
- 4) The quadrant in which the minor loop occurs.

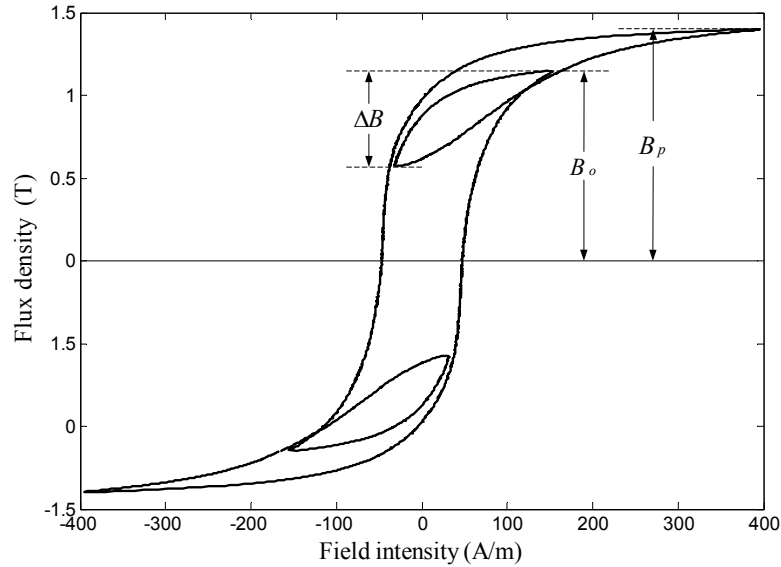


Fig. 4.1 Measured major and minor hysteresis loops

While the shape of the minor loop on the ascending part of the hysteresis loop is different from the minor loop shape on the descending part, it is observed from a series of minor loop measurements that the influence of the minor loop quadrant on the hysteresis loss is negligible. The same observation is also reported in [41]. Therefore, a series of minor loop measurements is performed with all combinations of various values of the first three parameters  $\Delta B$ ,  $B_o$  and  $B_p$ .

The minor loops can be generated in the laminations by imposing high frequency harmonics to the applied sinusoidal excitation waveform. The magnitude and position of the minor loop can be controlled by changing the magnitude and phase shift of the harmonic frequency. This method is used in [41-43] for minor loop measurements. However, the measured hysteresis loops with this method represents the dynamic hysteresis loops, which includes both the hysteresis and eddy current losses. Although the hysteresis loss component can still be separated from the total measured loss, the

separated minor loop hysteresis loss is less accurate, as it includes the core loss separation errors in addition to the measurement errors. In order to achieve accurate hysteresis loss measurements, the excitation waveform must have small magnetization rate, so that the measured loops would represent the quasi-static hysteresis losses.

Neglecting skin effect, the instantaneous eddy current loss in the lamination can be represented by,

$$P_e(t) = K_e \left( \frac{dB}{dt} \right)^2 \quad (4.1)$$

where  $K_e$  is dependent on the material electrical conductivity and the lamination thickness. In order to keep the instantaneous eddy current loss constant throughout the magnetization cycle, the measurements are performed under a controlled rate of change of magnetization. To generate a minor loop of a certain magnitude  $\Delta B$ , position  $B_o$  and peak flux density  $B_p$ , the flux reversal times are calculated based on a constant  $dB/dt$  and the corresponding flux waveform is generated in the laminations, as shown in Fig. 4.2. The applied voltage is then increased until the desired peak flux density  $B_p$  is reached. The hysteresis losses caused by the major and minor loops are then calculated by measuring the area enclosed by each loop.

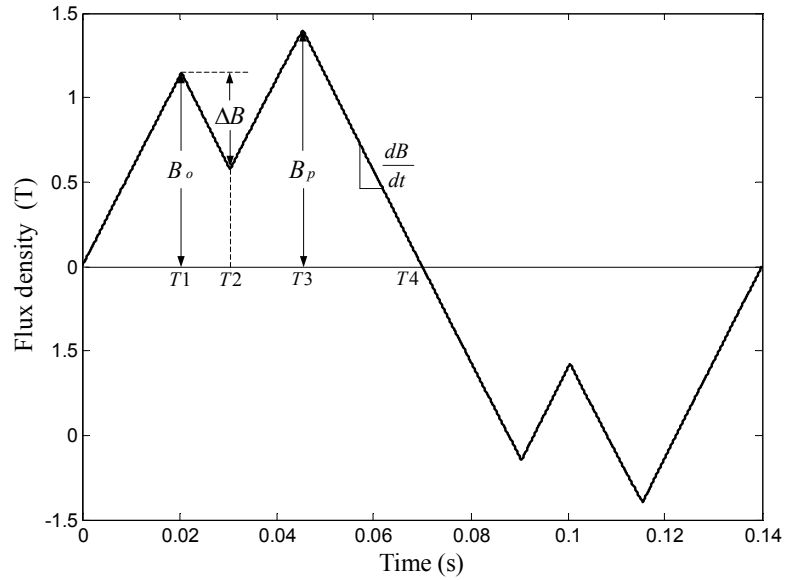


Fig. 4.2 The required flux density waveform to generate a certain minor loop

The measurements are performed using an Epstein frame test system. The system schematic diagram is shown in Fig. 4.3. The excitation signal is generated by Matlab Simulink interfaced with a dSPACE board, and applied to a high bandwidth amplifier, which excites the Epstein frame primary winding. The Epstein frame primary current and secondary voltage are measured and sent back to Matlab Simulink in order to calculate the hysteresis loops.

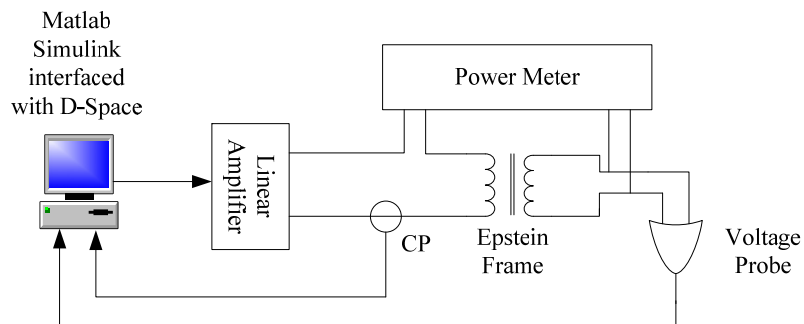


Fig. 4.3 Test system schematic diagram

### 4.3 Hysteresis Loss Modeling

Three methods for the prediction of hysteresis losses in electrical machines are presented. A conventional analytical model is first presented and its results are compared to the measured hysteresis losses. The Energetic hysteresis model is then adopted for improved minor loop hysteresis loss prediction. Then, a hybrid model that utilized both analytical and hysteresis models is proposed to achieve accurate and fast machine core loss prediction.

#### 4.3.1 Analytical Model

For the cases where the flux waveforms in the machine core are symmetric and contain only two flux reversals per cycle, the hysteresis energy loss can be represented by the modified Steinmetz equation [46] as,

$$W_h = K_h \hat{B}_p^{a+b\hat{B}_p+c\hat{B}_p^2} \quad (4.2).$$

The symmetric hysteresis losses for 0.5 mm-thick silicon iron (M45G26) are measured and the parameters  $K_h$ ,  $a$ ,  $b$  and  $c$  are then obtained from a curve fit of measured hysteresis loss data. The extracted parameters are shown in table 4.1. As shown in Fig. 4.4, the calculated hysteresis energy loss by equation (4.2) agrees well with the measured data. The total hysteresis loss is then calculated by simply multiplying the static hysteresis energy loss by the operating frequency. However, this simplification is only valid at lower frequencies, where skin effect is negligible, as skin effect causes the peak flux density to vary across the lamination causing the local hysteresis loops, and therefore the local hysteresis energy loss per cycle to differ at different points inside the

lamination. The hysteresis loss at high frequencies can be calculated by constructing the magnetic field distribution inside the lamination, as presented in [47]. However, this procedure is computationally intensive when the flux density waveforms are non-sinusoidal, as it becomes difficult to obtain the flux density distribution using the analytical models. Therefore, this method is not suitable for core loss determination in FEA machine design, which requires fast core loss calculations at each mesh element. Therefore, the total hysteresis energy loss is assumed to be only dependent on the flux density amplitude and the flux reversal points.

Table 4.1 Extracted coefficients for M45G26 steel

$K_h$	0.015
$a$	1.846
$b$	-0.585
$c$	0.480

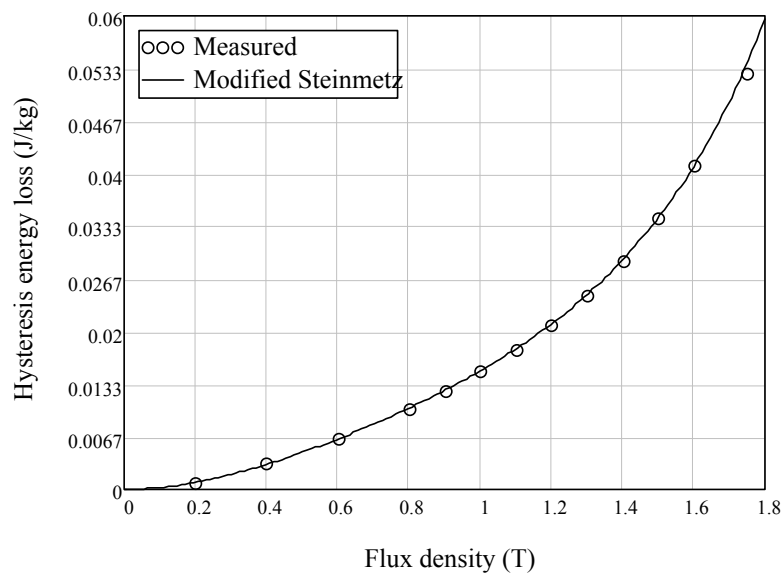


Fig. 4.4 Comparison between measured symmetric major loop hysteresis energy losses with the losses calculated by equation (4.2)

While equation (4.2) can calculate the symmetric major loop losses, the flux waveforms in many electrical machines may contain additional flux reversals and considerable DC components. The loss prediction in these machines requires a separate model for calculating minor hysteresis loop losses. A popular model for minor loop hysteresis loss prediction in electrical machine design is the model developed by Lavers [42]. According to the model, the hysteresis loss caused by a minor loop can be calculated by,

$$W_{hm} = W_h \Big|_{-B_p}^{B_p} \times \frac{k_m}{2} \times \frac{\Delta B}{B_p} \quad (4.3).$$

Lavers suggested that a value of the coefficient  $k_m$  between 0.6 and 0.7 is suitable for the cases where  $B_p$  is in the range of 1.0T to 2.0T and the ratio of  $\Delta B / B_p$  is relatively low. The hysteresis losses calculated by (4.3) with  $k$  equal to 0.65 are compared with the measured minor loop losses for various combinations of  $\Delta B$ ,  $B_o$  and  $B_p$ . As shown in Fig. 4.5, the model can provide a reasonable estimate of the hysteresis losses caused by relatively small minor loops occurring at the tip of the major loop. However, it underestimates the losses caused by larger minor loops. In addition, the formula does not account for the minor loop position  $B_o$ , which has a noticeable effect on the measured minor loop losses, as shown in Fig. 4.5. Figs. 4.6 and 4.7 show the errors of the calculated losses relative to the measured losses for  $B_p$  equal to 1.2T and 1.6T, respectively. It can be seen that the model results have acceptable errors for only a few cases of minor loops, and the prediction errors can be as high as 150% for minor loops with different positions and magnitudes. Therefore, the model cannot be relied on to

predict minor loop losses under a variety of possible encountered flux waveforms in electrical machines. Subsequently, an alternative method has to be implemented in order to achieve accurate hysteresis loss prediction.

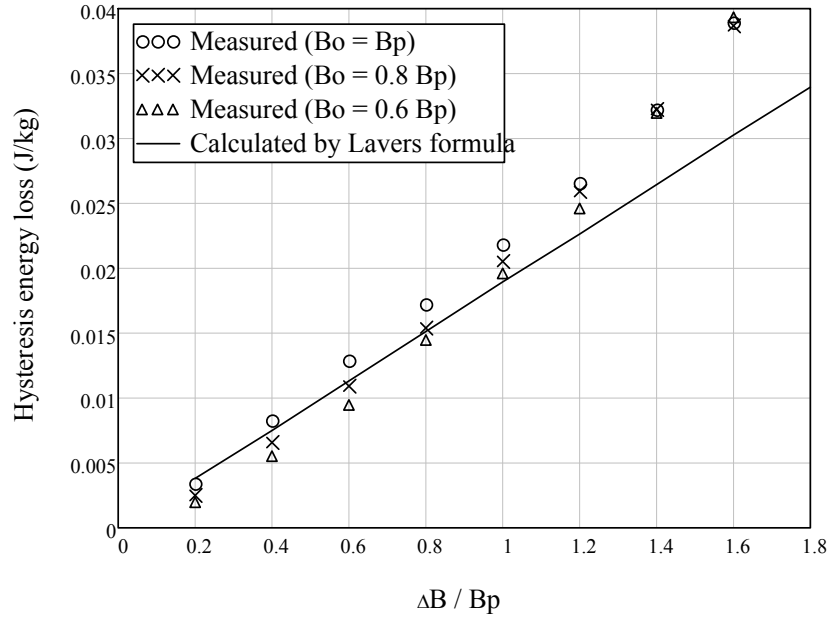


Fig. 4.5 Comparison between measured minor loop losses at different positions with the losses calculated by equation (4.3) for  $B_p = 1.4$  T

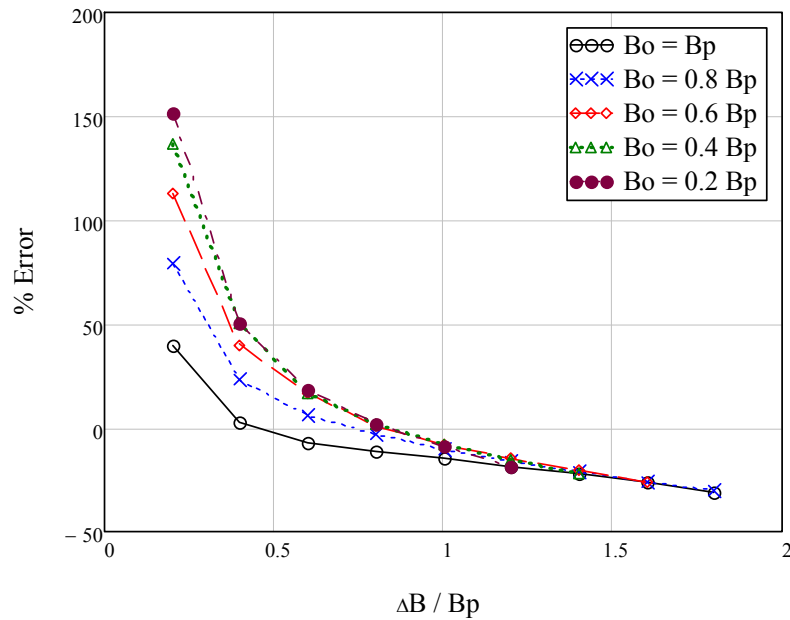


Fig. 4.6 Errors in the minor loop loss calculation using equation (4.3) for  $B_p = 1.2$  T

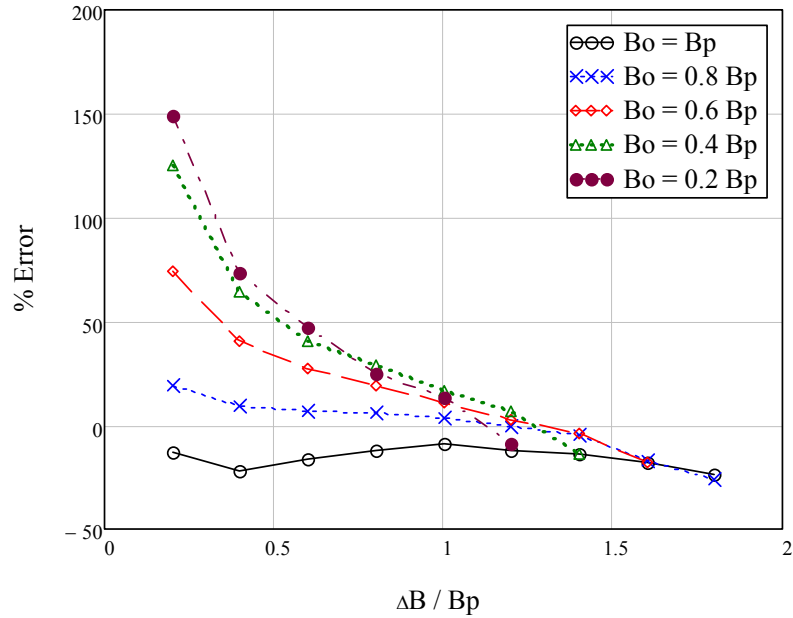


Fig. 4.7 Errors in the minor loop loss calculation using equation (4.3) for  $B_p = 1.6$  T

### 4.3.2 Energetic Model

The fundamental reason behind the failure of the analytical formulas to predict minor hysteresis loop losses is that the magnetic hysteresis process is such a complex phenomenon that it is very difficult to accurately predict its loss under any arbitrary flux waveform using a single empirical formula. Therefore, the hysteresis model has to be adapted in order to account for the non-linear behavior of the magnetic material under distorted excitations.

The suitable hysteresis model for core loss calculation in electrical machine FEA simulation should have two main features. Firstly, the model should be able to accurately simulate the major and minor hysteresis loops. Secondly, the hysteresis loop simulation should be computationally efficient, since the core loss has to be calculated in each mesh element. The Energetic model simulation of the hysteresis loops is suitable for fast core

loss calculations in electrical machine FEA simulations, as the magnetic field  $H$  at each time step can be calculated directly by only one equation from the flux density waveforms, which are available in the post-processing stage. The Energetic model is found to be capable of simulating the major hysteresis loops of electrical steels, as presented in [48]. In this section, the model capability to predict minor hysteresis loop losses is investigated.

In the Energetic model, the magnetic field  $H$  is calculated from the relative magnetization ( $m = M / M_s$ ) by,

$$H = N_e M_s m + \text{sgn}(m) h \left\{ \left[ (1+m)^{1+m} (1-m)^{1-m} \right]^{g/2} - 1 \right\} + \text{sgn}(m - m_0) \left( \frac{k}{\mu_0 M_s} + C_r H_r \right) \times \left[ 1 - \kappa \exp\left( -\frac{q}{\kappa} |m - m_0| \right) \right] \quad (4.4)$$

The first term of equation (4.4) represents the linear material behavior with  $N_e$ ,  $M_s$  being the demagnetization factor and saturation magnetization. The second term represents the non-linear material behavior with  $h$  and  $g$  relating to saturation field and anisotropy. The third term describes the hysteresis effects, with  $k$  relating to hysteresis loss,  $q$  to the pinning site density and  $C_r$  to the grain geometry. The reversible field function  $H_r$  is calculated by,

$$H_r = h \left\{ \left[ (1+m)^{1+m} (1-m)^{1-m} \right]^{g/2} - 1 \right\} \quad (4.5)$$

As suggested in [22], an improvement of minor loop representation can be achieved by modifying the hysteresis loss parameter  $k$  based on the peak magnetization  $M_p$  to,

$$k = k_0 \frac{(M_p / M_s) + 1}{2} \quad (4.6)$$

The function  $\kappa$  in equation (4.4) describes the influence of the total magnetic state at points of field reversals. The value of  $\kappa$  at the field reversal points is calculated based on its previous value  $\kappa_0$  from,

$$\kappa = 2 - \kappa_0 \exp\left(-\frac{q}{\kappa_0}|m - m_0|\right) \quad (4.7)$$

The model calculation starts with  $m_0 = 0$  and  $\kappa = 1$ ,  $m$  is then increased stepwise and the corresponding value of  $H$  at each step is calculated from equation (4.4). When  $m$  reaches the upper field reversal point,  $\kappa$  is calculated by equation (4.7) and  $m_0$  is set to the value of  $m$  at this point. Then  $m$  is decreased until the lower field reversal point is reached, and  $\kappa$  and  $m_0$  are recalculated. The same calculation procedure is executed for major and minor loop simulation. The only difference is that minor loop calculations are performed using the modified hysteresis loss parameter  $k$  in equation (4.6).

The Energetic model parameters are obtained using the measured static  $B-H$  loops according to the procedure described in [22]. The following parameters are first extracted from the major hysteresis loop; relative remnant magnetization  $m_r = M_r / M_s$ , coercive magnetic field intensity  $H_c$ , slope of the initial magnetization curve  $X_0$ , slope of the hysteresis loop at coercivity  $X_c$ , maximum measured relative magnetization and magnetic field intensity ( $m_m$  and  $H_m$ ) and finally the relative magnetization and magnetic field intensity of an arbitrary point at the knee of the major loop ( $m_g$  and  $H_g$ ).

Using the measured hysteresis loop parameters, the Energetic model parameters  $N_e$ ,  $k$

and  $q$  can be directly obtained by,

$$N_e = \frac{1}{X_c} \quad (4.8)$$

$$k = \mu_0 M_s H_c \quad (4.9)$$

$$q = \frac{M_s (1 - N_e X_0)}{H_c X_0} \quad (4.10)$$

The parameter  $g$  is then calculated from the numerical solution of the following transcendental equation,

$$\frac{[(1 + m_g)^{1+m_g} (1 - m_g)^{1-m_g}]^{g/2} - 1}{[(1 + m_m)^{1+m_m} (1 - m_m)^{1-m_m}]^{g/2} - 1} = \frac{H_g - H_c - N_e M_s m_g}{H_m - H_c - N_e M_s m_m} \quad (4.11)$$

$C_r$  and  $h$  can then be calculated directly using equations (4.12) and (4.13), respectively.

$$C_r = \frac{\frac{H_s - H_c - N_e M_s}{M_s \exp(g \ln 2)} [(1 + m_r)^{1+m_r} (1 - m_r)^{1-m_r}]^{g/2} - 1 - \left[ 1 - 2 \exp\left(q \frac{m_r - m_m}{2}\right) \right] \frac{H_c}{M_s} + N_e m_r}{\left\{ \frac{H_s - H_c - N_e M_s}{M_s \exp(g \ln 2)} [(1 + m_r)^{1+m_r} (1 - m_r)^{1-m_r}]^{g/2} - 1 \right\} + \frac{H_c}{M_s}} \left[ 1 - 2 \exp\left(q \frac{m_r - m_m}{2}\right) \right] - N_e m_r} \quad (4.12)$$

$$h = \frac{H_s - H_c - N_e M_s}{(C_r + 1)(\exp(g \ln 2) - 1)} \quad (4.13)$$

The extracted Energetic model parameters for M45 steel are shown in table 4.2.

Table 4.2 Extracted Energetic model parameters for M45G26 steel

$N_e$	$1.189 \times 10^{-5}$
$M_s$	$1.432 \times 10^6$
$h$	7.332
$g$	9.957
$k$	82.800
$q$	35.110
$C_r$	0.342

Figs. 4.8-4.11 compare the measured and simulated hysteresis loops for different minor loop magnitudes  $\Delta B$ , positions  $B_o$  and peak flux densities  $B_p$ . It is can be seen that the simulated loops agree well with the measured data, qualitatively. The minor loop hysteresis losses are then calculated for numerous minor loops of different  $\Delta B$ ,  $B_o$  and  $B_p$ . Figs 4.12 and 4.13 show the errors of the calculated losses by the Energetic model compared to the measured losses for  $B_p$  equal to 1.2T and 1.6T, respectively. It is clear that the Energetic model can achieve improved minor loop loss prediction compared to the analytical model with maximum error lower than 25%.

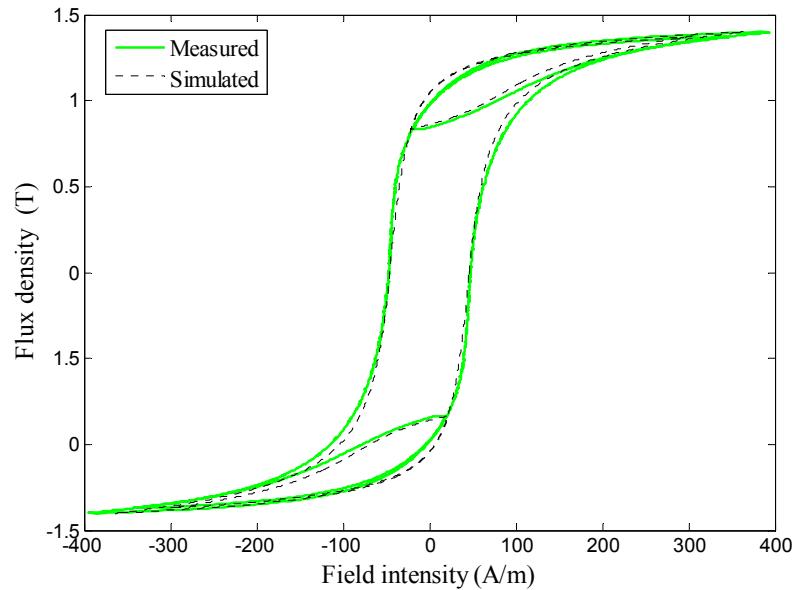


Fig. 4.8 Comparison of measured and simulated loops for  $\Delta B = 0.4B_p$ ,  $B_o = B_p$  and  $B_p = 1.4T$

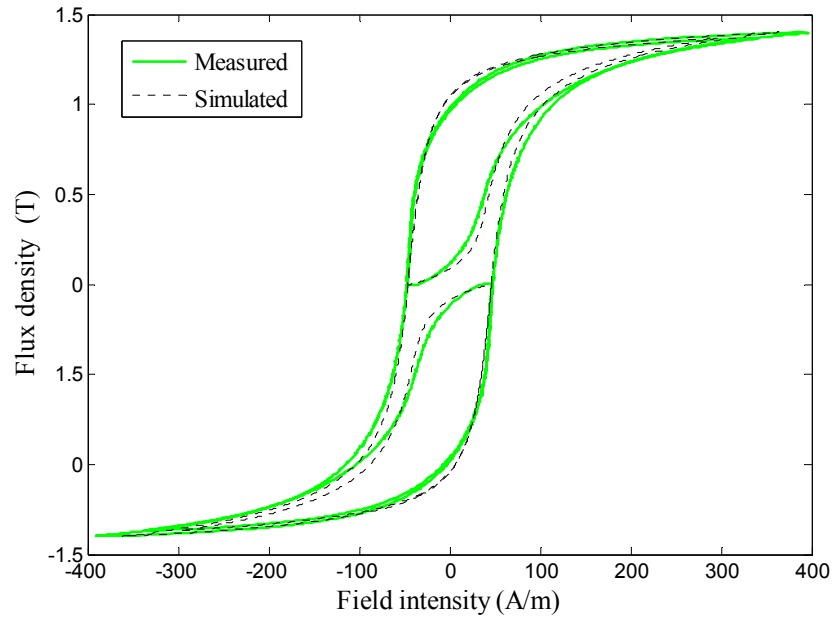


Fig. 4.9 Comparison of measured and simulated loops for  $\Delta B = B_p$ ,  $B_o = B_p$  and  $B_p = 1.4T$

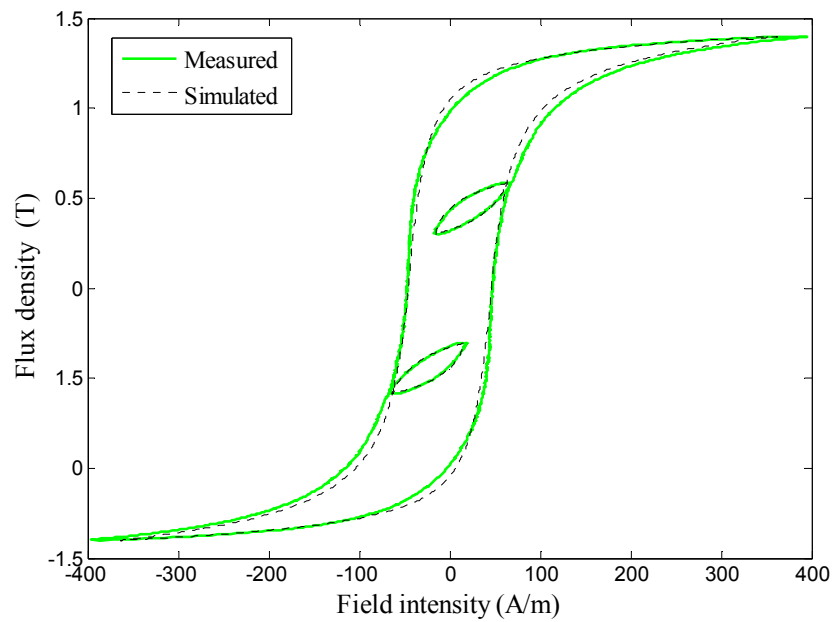


Fig. 4.10 Comparison of measured and simulated loops for  $\Delta B = 0.2B_p$ ,  $B_o = 0.4B_p$  and  $B_p = 1.4T$

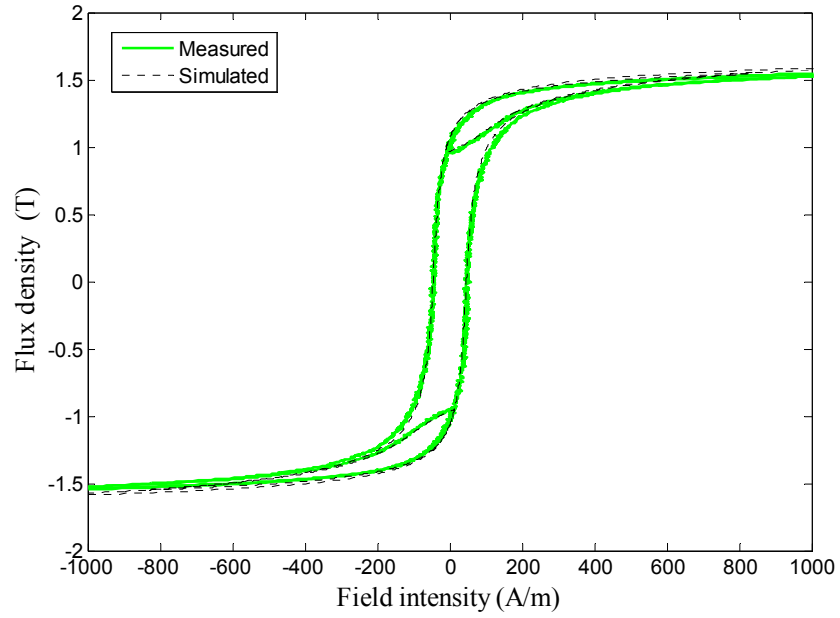


Fig. 4.11 Comparison of measured and simulated loops for  $\Delta B = 0.4B_p$ ,  $B_o = B_p$  and  $B_p = 1.6T$

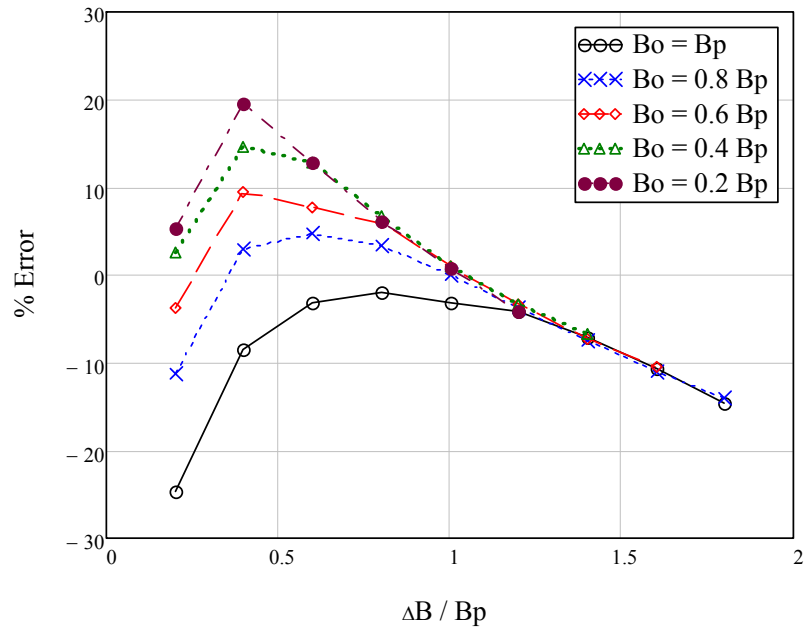


Fig. 4.12 Errors in the minor loop hysteresis losses calculation using the Energetic model for  $B_p = 1.2 T$

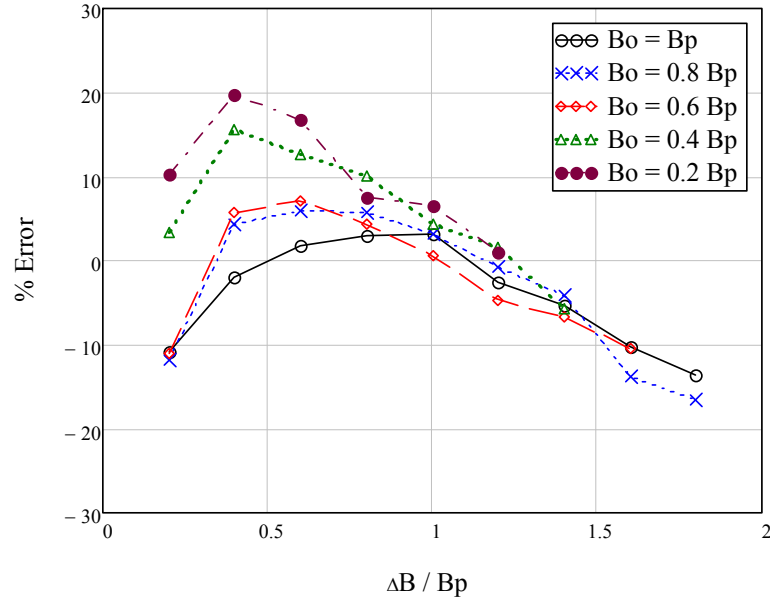


Fig. 4.13 Errors in the minor loop hysteresis loss calculation using the Energetic model for  $B_p = 1.6$  T

### 4.3.3 Hybrid Model

Although the Energetic model is capable of simulating the major hysteresis loops, the model results are not as accurate as the calculated losses by the modified Steinmetz equation. Fig. 4.14 compares the errors of the calculated loss by the Energetic model with equation (4.2) errors. It can be seen that precise symmetric major loop loss prediction can be achieved by the analytical formula without the need for the multiple iterations required for simulating the hysteresis loop by the Energetic model. On the other hand, when it comes to minor loop loss prediction, it is obvious that the Energetic model errors in Figs 4.12 and 4.13 are much lower than the analytical model errors in Figs. 4.6 and 4.7. Therefore, it is important to use a hysteresis model in order to achieve accurate minor loop loss prediction, as the analytical model can only predict minor loop losses for some specific cases of minor loops, and it cannot be relied on to predict minor loop losses under a large variety of possible flux waveforms in electrical machines.

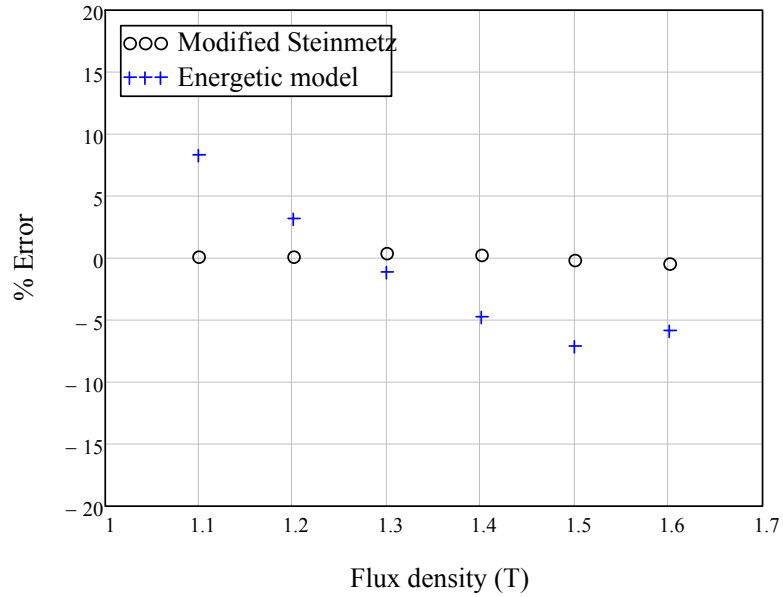


Fig. 4.14 Comparison of the errors of symmetric major hysteresis loop calculation by the energetic model and the modified Steinmetz equation

A hybrid model is developed to achieve accurate hysteresis loss prediction in electrical machines. The model flow chart is shown in Fig. 4.15. From the flux density waveform, the model first extracts the major loop and minor loop flux reversals. The symmetric major loop hysteresis losses are then calculated by the modified Steinmetz equation and the minor loop losses are calculated using the Energetic model. However, in some cases, the machine can experience particular cases of major loops with large DC component, e.g. the unidirectional flux in a SRM stator pole. The hysteresis losses under these waveforms cannot be predicted by the modified Steinmetz equation, and accurate loss prediction requires simulating the hysteresis loops by the Energetic model. On the other hand, having a small DC component in the flux waveform might not also justify using the Energetic model for the hysteresis loss calculation.

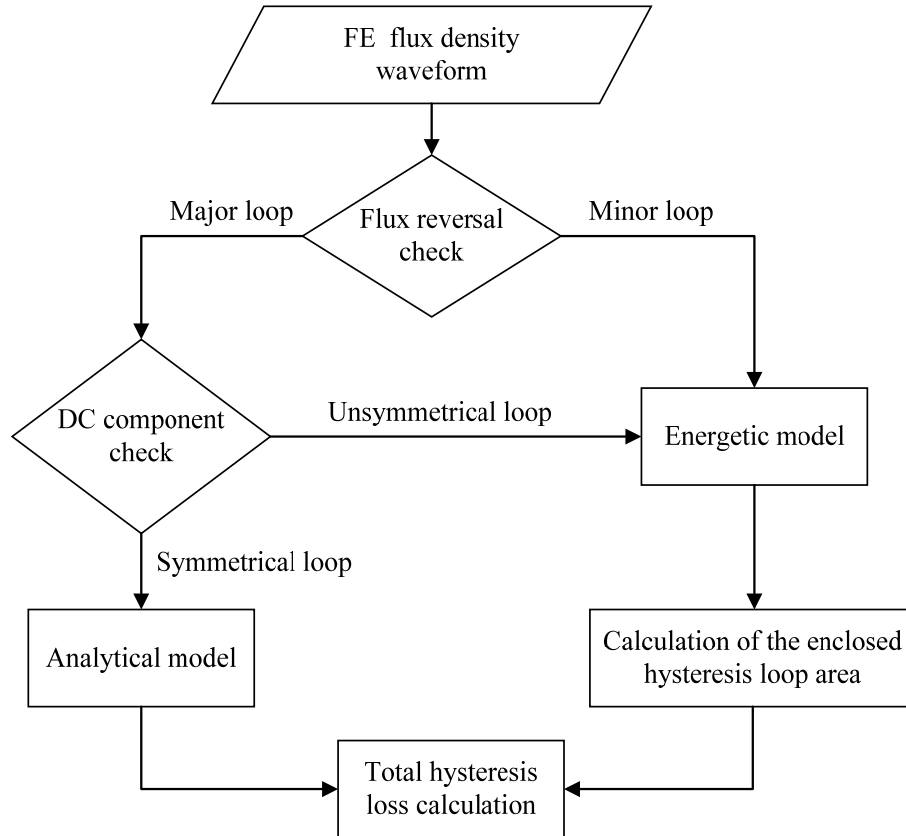


Fig. 4.15 Hybrid model flow chart

In order to find out the DC component at which the hybrid model should switch from the analytical to the Energetic model in the major loop loss calculation, the hysteresis loops with different DC components are measured and compared to the calculated losses by the Energetic model and the modified Steinmetz equation. It can be inferred from the errors, shown in Fig. 4.16, that improved major loop prediction for the tested material is achieved by the Energetic model for hysteresis loops with DC components larger than 0.34T. Therefore, the hybrid model generally uses the analytical equation for calculating the major loop losses, except in the cases where the DC component exceeds 0.34T, as the hybrid model switches from the analytical to the Energetic model for improved major loop loss determination.

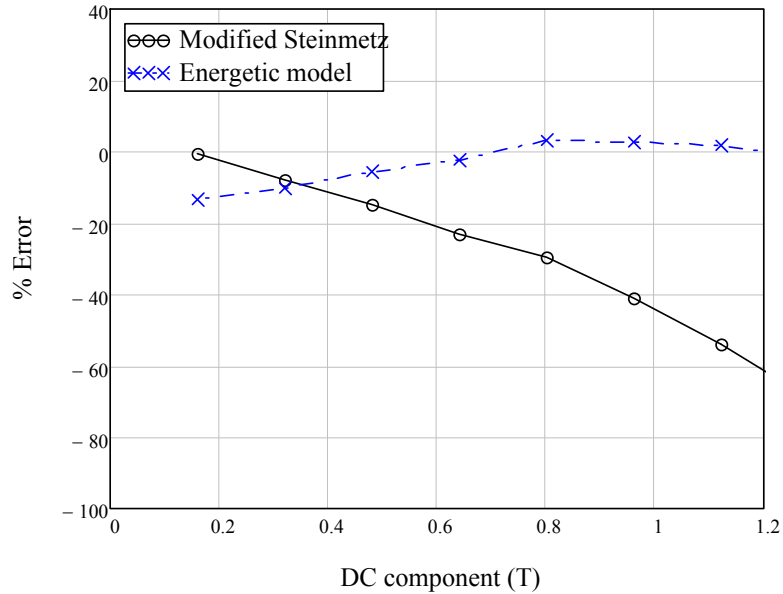


Fig. 4.16 Comparison of the errors of the Energetic model and the modified Steinmetz equation for different DC components

#### 4.4 Prediction of Hysteresis Loss in Switched Reluctance Machines

Switched reluctance machines are increasingly being adopted in high speed applications, due to their drive reliability and robust rotor construction. In high speed application of SRMs, core losses become the dominant loss component. Therefore, the machine optimization requires having a model that can provide accurate core loss prediction. The difficulty of core loss prediction in SRMs is attributed to the nature of the machine flux, as the flux waveforms are naturally non-sinusoidal and vary in different parts of the machine core [49-52]. In this section, the three previously discussed models are applied to predict the hysteresis losses of a 6/4 SRM.

The flux density waveforms of the 6/4 SRM in Fig. 4.17 are obtained by FEA simulation. Figs. 4.18-4.21 show the calculated flux density waveforms at different parts of the machine core. The Energetic model is then used to simulate the hysteresis loops under

these waveforms. It can be seen from the simulated hysteresis loops in Figs. 4.22-4.25 that the machine core experiences unsymmetrical major loops as well as a variety of minor loops of different magnitudes and positions.

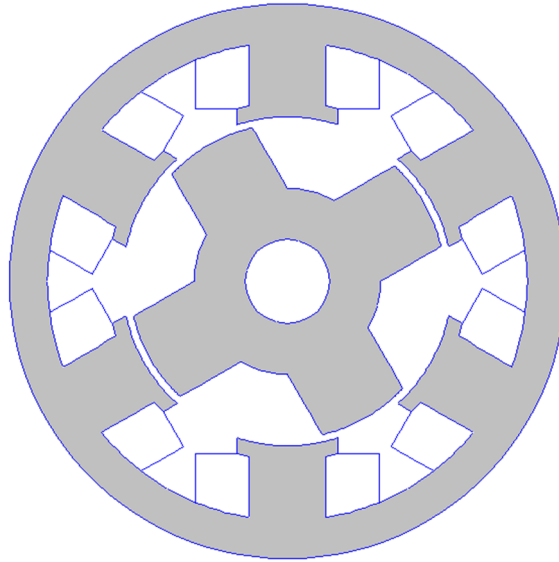


Fig. 4.17 Cross section of the simulated 6/4 SRM

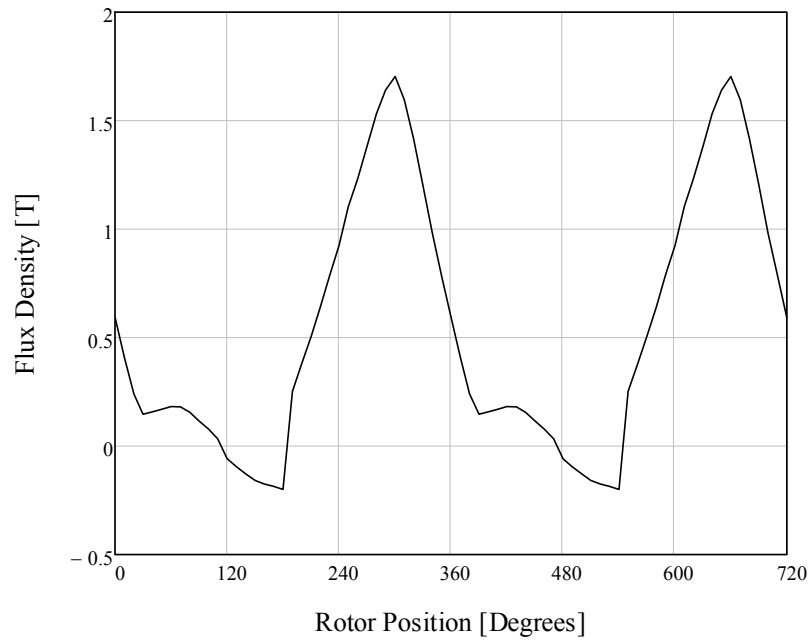


Fig. 4.18 Simulated flux density waveform in the stator pole of the SRM

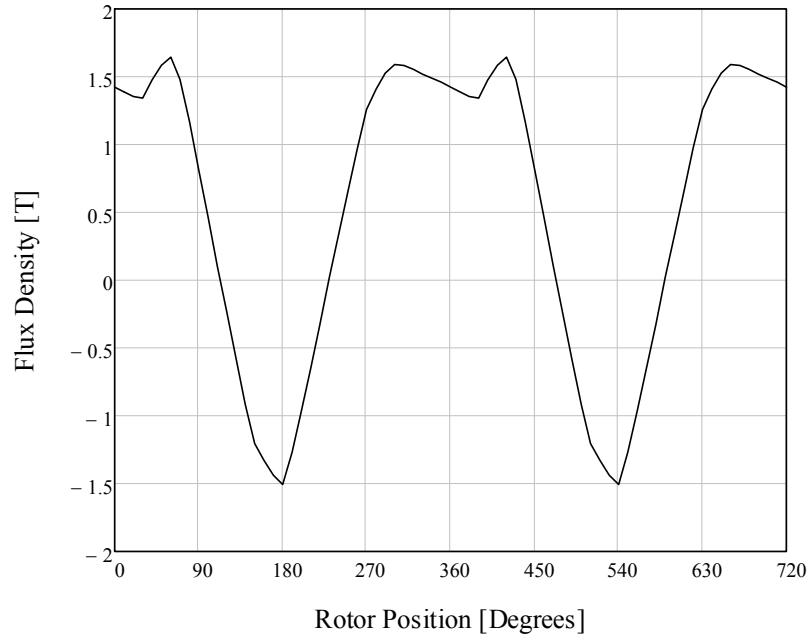


Fig. 4.19 Simulated flux density waveform in the stator core of the SRM

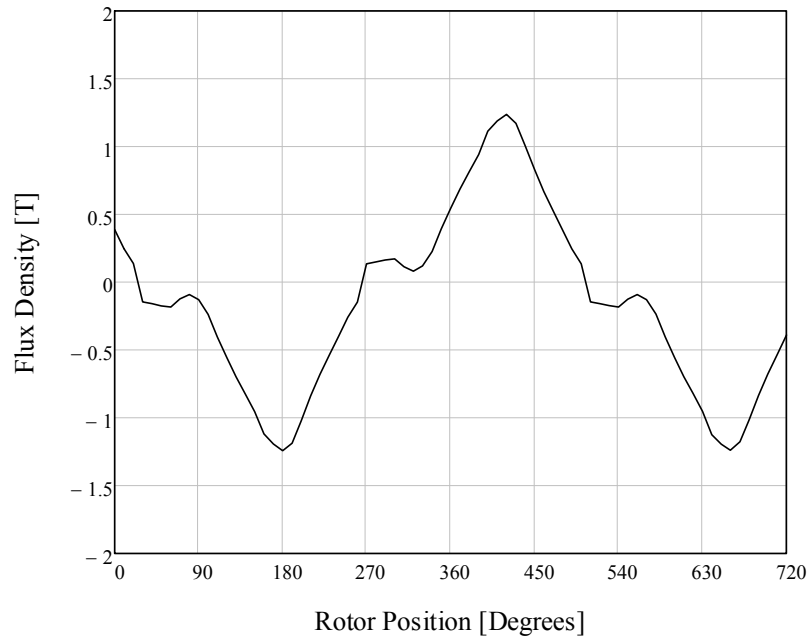


Fig. 4.20 Simulated flux density waveform in the rotor pole of the SRM

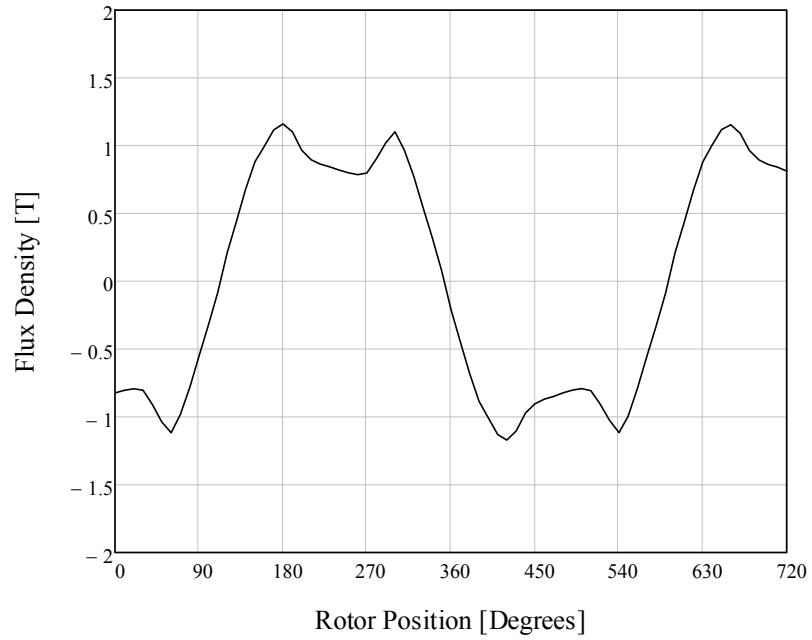


Fig 4.21 Simulated flux density waveform in the rotor core of the SRM

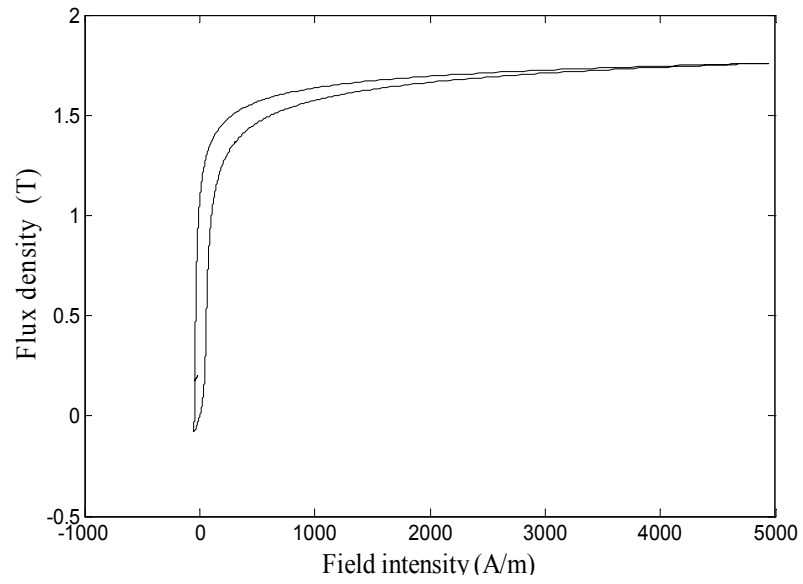


Fig. 4.22 Simulated hysteresis loop in the stator pole of the SRM

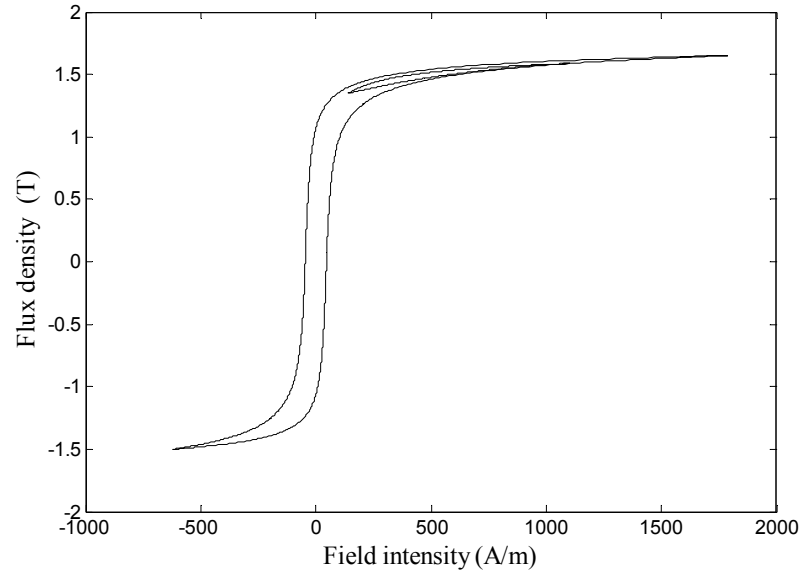


Fig. 4.23 Simulated hysteresis loop in the stator yoke of the SRM

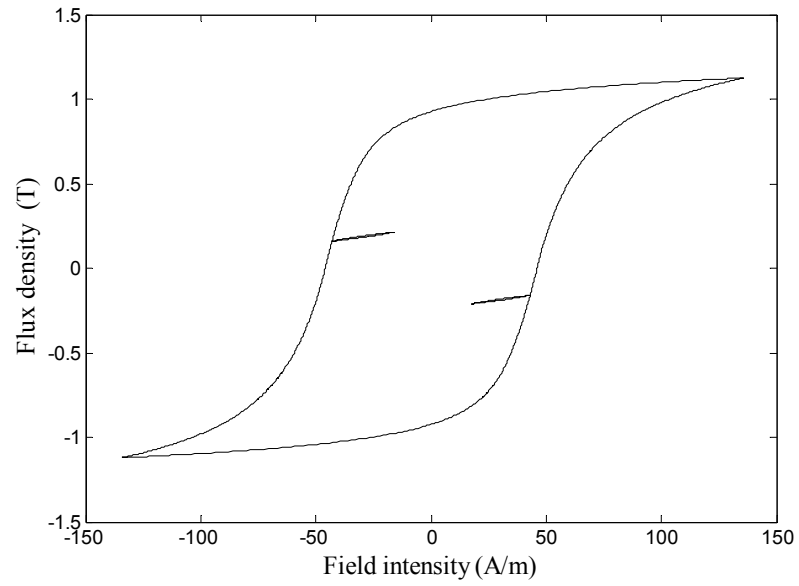


Fig. 4.24 Simulated hysteresis loop in the rotor pole of the SRM

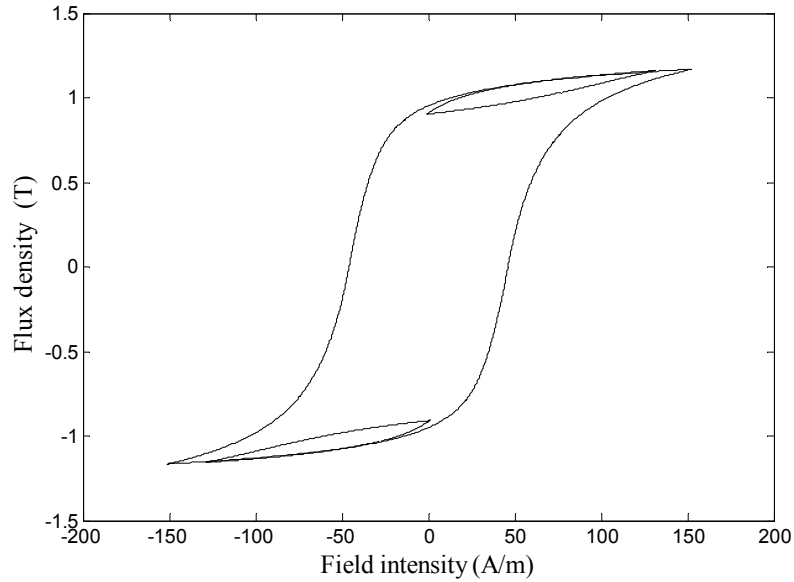


Fig. 4.25 Simulated hysteresis loop in the rotor core of the SRM

The hybrid model is then applied to calculate the machine hysteresis losses. Fig. 4.26 shows the regions at which the hybrid model switches from using the analytical equations to the Energetic model or uses both of them for hysteresis loss calculation. It can be seen from Fig. 4.26 that part of the rotor pole uses only the modified Steinmetz equation as the flux waveform in this region is symmetric and the minor hysteresis loop losses are negligible. On the other hand, in the stator pole, the hybrid model uses only the Energetic model for simulating both major and minor hysteresis loops as the major loop contains significant DC component. The rest of the machine uses the Energetic model for calculating the minor loop losses and uses the modified Steinmetz equation for the major loop losses, as the major loop DC component is lower than 0.34T.

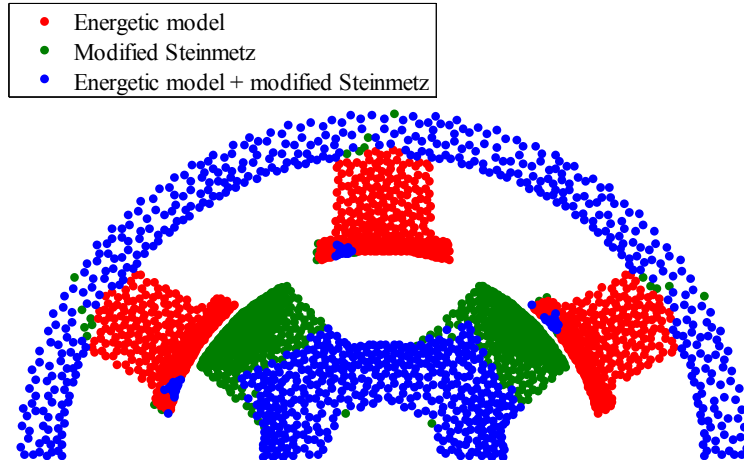


Fig. 4.26 Spatial distribution of different calculation techniques used by the hybrid model

Table 4.3 compares the machine hysteresis losses calculated by the three models described in section 4.3. The hybrid model results are considered the base for the loss comparison, as its calculated losses are closest to the measured major and minor loop hysteresis losses. The machine hysteresis losses calculated by the analytical model are about 6.5% lower than the hybrid model losses. The main reason of this divergence is that the analytical model underestimates the hysteresis losses of the unipolar flux waveforms in the stator pole. It can also be observed from table 4.3 that the machine losses calculated by using only the Energetic model are higher than the hybrid model losses, as analytical prediction of major loop losses is found to be more accurate than the Energetic model simulations.

Table 4.3 Comparison between the machine hysteresis losses calculated by the analytical, Energetic and hybrid models

	Stator loss (W)	Rotor loss (W)	Total loss (W)
Hybrid model	6.8412	1.7705	8.6118
Analytical model	6.2585	1.8298	8.0883
Energetic model	7.0937	1.9940	9.0878

#### 4.5 Summary

A series of minor hysteresis loops of different magnitudes, positions, and major loop peak flux densities are measured. The measured hysteresis losses are then compared to the losses calculated by an analytical model. The model is able to accurately predict the symmetrical major loop losses. However, it can only predict minor loop losses under particular conditions. Therefore, the Energetic model is implemented in order to predict the minor loop losses. While the Energetic model can achieve considerable improvement of minor loop loss prediction, the symmetric major loop losses calculated analytically are found to be more accurate. Consequently, a hybrid model is developed to calculate the hysteresis losses using both the analytical equations and the Energetic model. The hybrid model is then applied to calculate the hysteresis losses in a SR machine. The results show that having a model that is capable of calculating the hysteresis losses under a variety of minor loops is essential for precise machine core loss prediction.

## 5. HYSTERESIS DEPENDENT MODEL FOR THE BRUSHLESS EXCITER OF SYNCHRONOUS GENERATORS

### 5.1 Introduction

During the past four decades, brushless excitation of synchronous generators has replaced the classical excitation systems in many applications, as they offer increased reliability and reduced maintenance of the generator system [53]. In the brushless excited generator system shown in Fig. 5.1, the exciter armature feeds the main generator field winding through a rectifier mounted on the generator shaft. The generator output voltage is regulated by controlling the exciter field voltage.

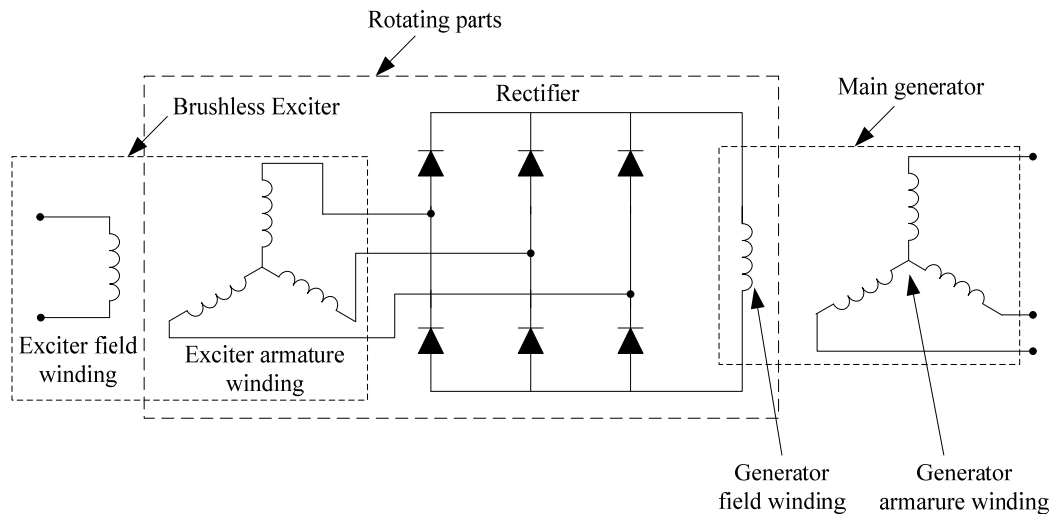


Fig. 5.1 Schematic diagram of a brushless synchronous generator system

In order to accurately represent synchronous machines in power system stability studies, their excitation system has to be modeled in sufficient detail. The widely used transfer function for the brushless exciter proposed by the IEEE [54] is found to be approximate. An alternative approach for representing the brushless excitation system is to model the

exciter using a synchronous generator  $dq$ -axes model in conjunction with a rectifier model [55-58]. This approach offers improved simulation of the brushless excitation system compared to the classical IEEE model. However, the variation of the exciter magnetization inductance due to the hysteresis effects is found to cause a deviation between the measured and simulated generator transient response [56, 57]. Therefore, accurate simulation of the power system dynamics requires incorporating the hysteresis effects into the brushless exciter model. In [57], a hysteretic model is proposed to incorporate the magnetic hysteresis effects into the magnetization inductance of the exciter  $dq$ -axes model using Preisach theory. The model simulation results are found to be in good correlation with the measured response of a brushless excited synchronous generator system [57]. However, the identification of the model parameters, in particular the hysteresis model parameters, requires a quite complex procedure. A genetic algorithm (GA) is proposed in [58] to determine the model parameters. In addition to the parameter identification complexity, the incorporation of the Preisach hysteresis model into the time-domain simulation of the power system substantially increases the simulation time.

In this chapter, a simple method is developed to incorporate the magnetic hysteresis effects into the magnetization branch of the brushless exciter  $dq$ -axes model. The developed method utilizes the Energetic hysteresis model to achieve computationally efficient simulation, and its identification only requires a few measured parameters. While the method is applied here to predict the transient response of the brushless excitation system, it can also be utilized to incorporate the hysteresis effects into any electrical machine model.

## 5.2 Hysteresis Effect on the Brushless Exciter Transient Response

The brushless exciter machine can be viewed as a synchronous machine with the field winding placed on the stator side and the armature winding on the rotor. Fig. 5.2 shows a simplified representation of a two pole brushless exciter [57].

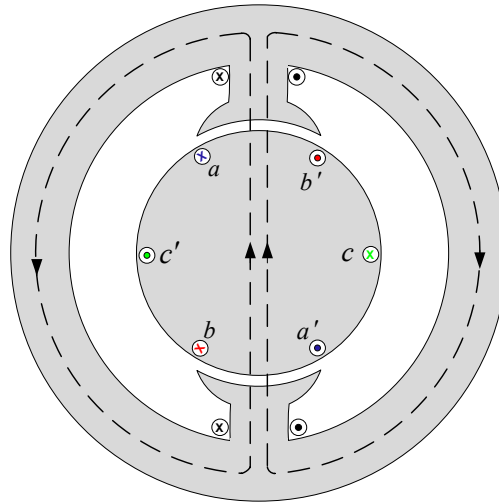


Fig. 5.2 Simplified construction of a 2-pole brushless exciter

At steady state, the exciter stator field current is constant and since the rotor current fundamental frequency is equal to the machine rotational electrical frequency, the rotor flux can be considered time invariant from the stator point of view. Therefore, the machine stator core mostly experiences DC flux at steady state. However, when a change in the generator voltage is commanded, the corresponding variation in the exciter field voltage causes fluctuations in the magnetization flux linkage, as illustrated in Fig. 5.3. This causes the exciter steel to follow different hysteresis curves during transients. The variation of the steel operating point changes the exciter magnetization inductance, which can be defined as the local slope of the magnetization flux linkage-current loops. Fig. 5.4

shows the simulated magnetization flux linkage-current loops due to the flux linkage transient in Fig. 5.3. It is clear that the local slope of these loops is changing in time. Therefore, in order to accurately simulate the machine transient response, the value of the magnetization inductance in the exciter model should be dependent on the flux linkage-current trajectory.

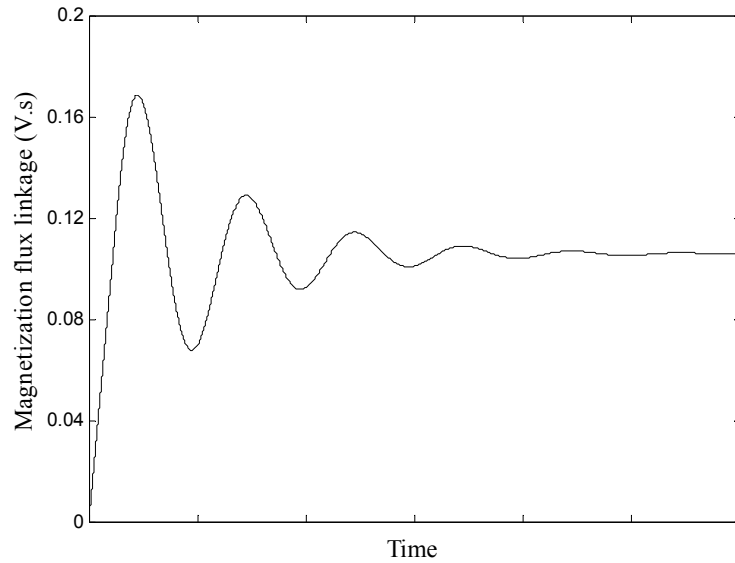


Fig. 5.3 Illustration of the exciter flux linkage variation during transient

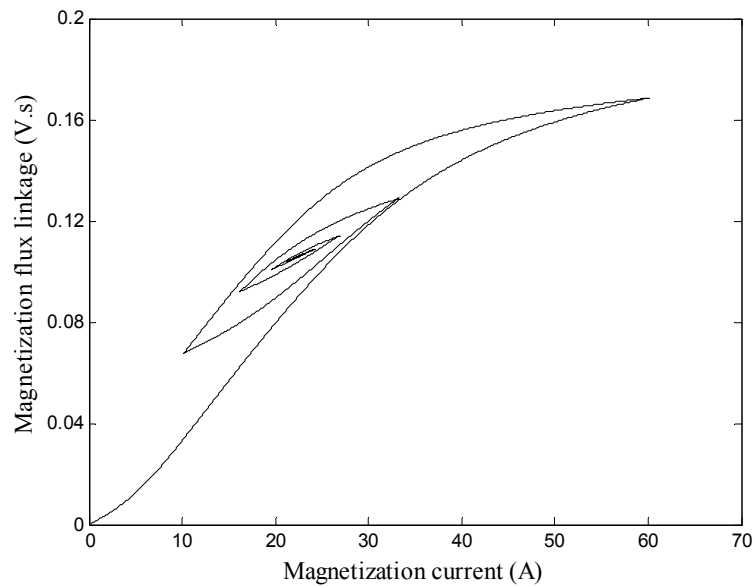


Fig. 5.4 Illustration of magnetization flux linkage - current loops during transient

In addition to the magnetization inductance variation, using a static magnetization inductance implies that when no voltage is applied to the exciter, the magnetization flux and the exciter output voltage should be zero, which is not correct, as the remnant flux in the exciter steel core can still generate some voltage in the generator field winding even if there is no voltage applied to the exciter field. This phenomenon is utilized in the self-starting of brushless synchronous generators in case there is no other power source available at the voltage regulator.

### 5.3 Hysteretic Model

A hysteretic model is developed to simulate the magnetization flux linkage-current characteristics of the brushless exciter machine. The model derivation is based on the fact that the flux path reluctance of any electric machine can be broken down to a linear reluctance in the air gap  $R_a$  and a non-linear reluctance introduced by the steel core  $R_s$ . According to this simple concept, the machine magnetization can be represented by the electric circuit shown in Fig. 5.5, where the total magnetization current  $i_m$  is the addition of the current required to overcome the air gap reluctance  $i_a$  and the current required to overcome the steel reluctance  $i_s$ . Accordingly, the total magnetization current can be represented by,

$$i_m = \frac{\lambda_m}{L_a} + i_s(\lambda_m) \quad (5.1)$$

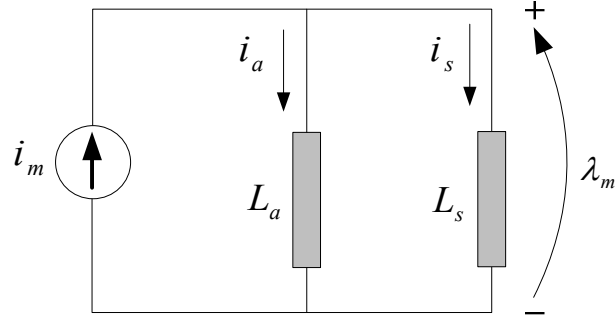


Fig. 5.5 Simplified machine magnetic equivalent circuit

$L_a$  is the air gap inductance, and  $i_s(\lambda_m)$  represents the steel hysteretic flux linkage-current characteristics, which is calculated here by,

$$i_s(\lambda_m) = K_H H_e(K_B \lambda_m) \quad (5.2)$$

The Energetic function  $H_e$  calculates the steel magnetic field using equation (4.4) from the flux density, which is represented by the multiplication of the flux linkage  $\lambda_m$  with a constant  $K_B$ . The constant  $K_H$  is the ratio between the steel magnetization current and the steel magnetic field. From equations (5.1) and (5.2), the magnetization flux linkage-current loops can be simulated by,

$$i_m = \frac{\lambda_m}{L_a} + K_H H_e(K_B \lambda_m) \quad (5.3)$$

#### 5.4 Identification of the Hysteretic Model parameters

The parameters  $L_a$ ,  $K_H$  and  $K_B$  in equation (5.3) depend on the detailed machine design configuration, which is not available for commercial generators. Therefore, the following

procedure is developed to determine these parameters from the steel  $B-H$  loops and the measured flux linkage-current loops of the brushless exciter.

1) *Air gap inductance ( $L_a$ )*

From the steel and air gap flux linkage-current characteristics shown in Fig. 5.6, it clear that the steel inductance at coercivity  $L_{cs}$  is much larger than  $L_a$ , and since the magnetization inductance  $L_m$  is equivalent to  $L_a$  in parallel with  $L_s$ , the air gap inductance  $L_a$  is approximately equal to the magnetization inductance at coercivity  $L_{cm}$ , which can be found from the measured magnetization flux linkage-current loop, as shown in Fig. 5.7.

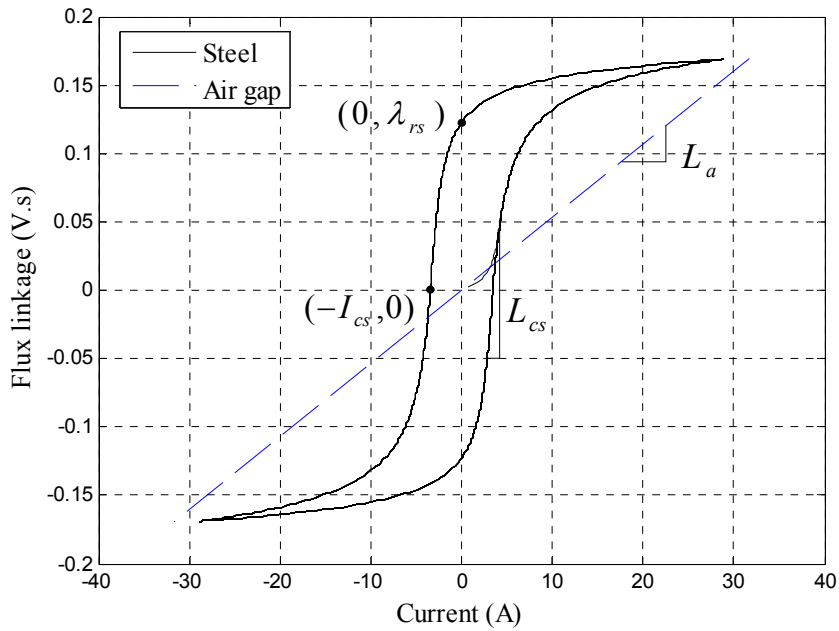


Fig. 5.6 Flux linkage-current characteristics for the steel and air gap

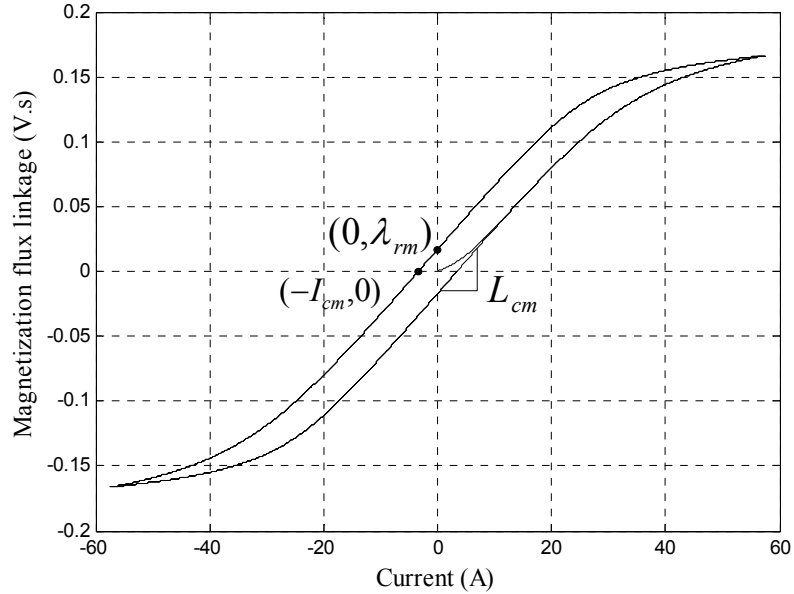


Fig. 5.7 Typical magnetization flux linkage-current loop

2) *Current – field ratio ( $K_H$ ):*

The ratio between the steel magnetization current  $i_s$  to its electrical field  $H_s$  can be determined using the measured magnetization flux linkage-current loop of the exciter and the measured steel  $B$ - $H$  loop, as the current required to bring the magnetization flux down to zero  $I_{cm}$  can be found experimentally, as illustrated in Fig. 5.7. The ratio between this current and the steel coercive magnetic field  $H_c$  is the constant  $K_H$ .

3) *Flux linkage – flux density ( $K_B$ ):*

The constant  $K_B$  can be calculated from the analysis of the magnetic circuit at remnance. However, the simple magnetic circuit in Fig. 5.5 assumes linear reluctance elements, which cannot account for the steel remnant flux. Therefore, the linear steel reluctance is replaced by the equivalent circuit of a permanent magnet, which is a voltage source

representing the steel coercive force  $F_c$  in series with the steel reluctance. Fig. 5.8 shows the modified magnetic equivalent circuit at remnance. The constant  $K_B$  is determined from the ratio between the measured flux linkage at zero current  $\lambda_{rm}$  and the steel flux density at zero current  $B_m$ , which differs from the steel remnant flux density  $B_r$  when an air gap is present in the magnetic circuit.

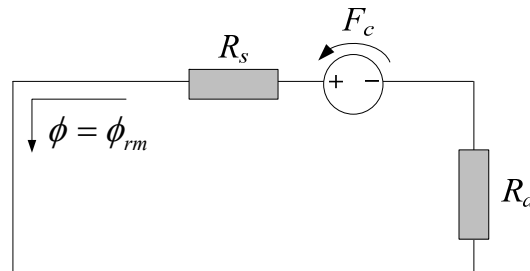


Fig. 5.8 Modified magnetic equivalent circuit at remnance

The employed permanent magnet equivalent circuit in Fig. 5.8 assumes a linear demagnetization curve, and the corresponding magnet operating point occurs at the intersection of the linear demagnetization curve with the air gap line. On the other hand, the demagnetization curve of the steel is non-linear, as it has a knee near the remnance point, as shown in Fig. 5.9. However, due to the narrow steel  $B-H$  loop, the air gap line always meets the steel demagnetization curve at the linear region near coercivity, as shown in Fig. 5.9. Therefore, this type of analysis can still be applied to predict the operating point of the steel by using a fictitious linear demagnetization curve that is extended from coercivity to a fictitious remnant flux density  $B_r'$  with a slope of steel permeability at coercivity ( $\mu_0 X_c$ ), as  $\mu_0$  is the free space permeability and  $X_c$  is the steel susceptibility at coercivity. The intersection between this fictitious line and the air gap line represents the steel operating point at zero current.

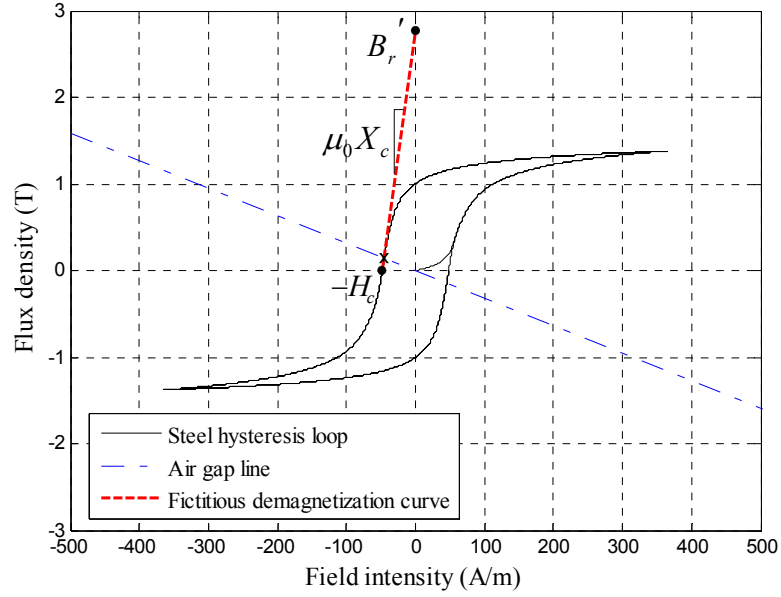


Fig. 5.9 Illustration of the steel operating point at zero current

From the analysis of the magnetic circuit at remnance in Fig. 5.8, the steel flux can be calculated by,

$$\phi_m = \frac{Fc}{R_s + R_a} \quad (5.4)$$

The steel operating flux density at zero current can then be calculated by,

$$B_m = B_r' \frac{R_s}{R_s + R_a} \quad (5.5)$$

The air gap and steel reluctances can be expressed as,

$$R_a = \frac{1}{L_a} \quad (5.6)$$

$$R_s = \frac{\Delta I}{\Delta \lambda} = \frac{\Delta H}{\Delta B} \frac{\Delta B}{\Delta \lambda} \frac{\Delta I}{\Delta H} = \frac{1}{\mu_0 X_c} \frac{K_H}{K_B} \quad (5.7)$$

Substituting (5.6) and (5.7) into (5.5), the steel flux density can be represented by,

$$B_m = \frac{B_r'}{1 + \frac{\mu_0 X_c K_B}{L_a K_H}} \quad (5.8)$$

From the measured flux linkage at zero current, the steel flux density can also be represented as,

$$B_m = \frac{\lambda_{rm}}{K_B} \quad (5.9)$$

By solving (5.8) and (5.9),  $K_B$  can be determined by,

$$K_B = \frac{1}{\left( \frac{X_c H_c}{\lambda_{rm}} - \frac{\mu_0 X_c}{K_H L_a} \right)} \quad (5.10)$$

## 5.5 Brushless Exciter Model

The developed hysteretic model is integrated into the  $dq$ -axes model of a brushless exciter machine. The  $d$ -axis magnetization inductance is replaced by the hysteretic model, as shown in Fig. 5.10. The machine model is then implemented in Matlab Simulink, where the hysteretic magnetization branch is represented by a controlled current source, as shown in Fig. 5.11. The magnetization  $d$ -axis voltage  $v_{md}$  is measured and integrated to obtain the magnetization flux linkage  $\lambda_{md}$ , which is fed to the hysteretic model in order to calculate the  $d$ -axis magnetization current  $i_{md}$ . The calculated  $i_{md}$  is then applied as a control signal for the magnetization current source.

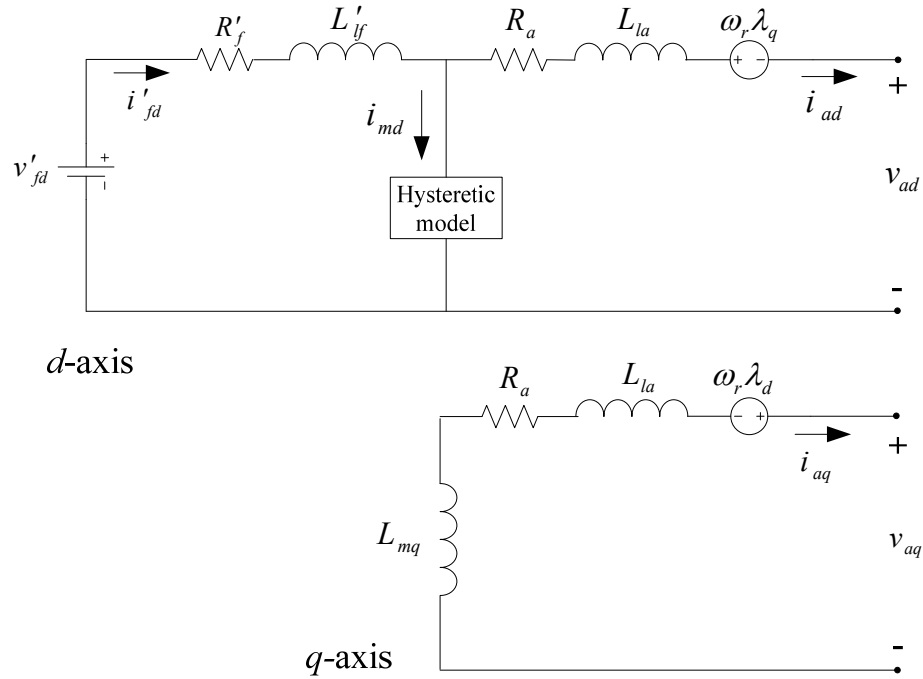


Fig. 5.10 Brushless exciter  $dq$ -axes model

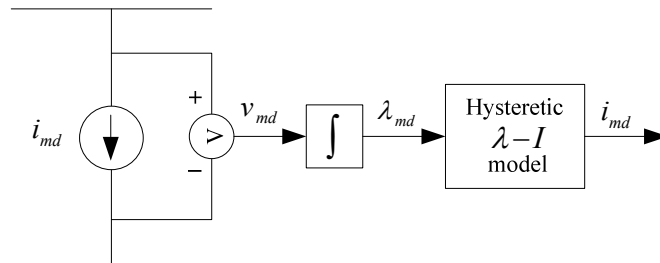


Fig. 5.11 Implementation of the hysteric magnetization branch

As shown in Fig. 5.10, the cross coupling terms in the exciter armature branch contains the total  $d$  and  $q$  axes flux linkages ( $\lambda_d$  and  $\lambda_q$ ), which can be calculated by,

$$\lambda_d = -(L_{la} + L_{md})i_{ad} + L_{md}i'_{fd} \quad (5.11)$$

$$\lambda_q = -(L_{la} + L_{mq})i_{aq} \quad (5.12)$$

Equation (5.11) can be rewritten as,

$$\lambda_d = \lambda_{md} - L_{la}i_{ad} \quad (5.13)$$

Using equation (5.13) for  $\lambda_d$  calculation along with the hysteretic model in the magnetization branch eliminates the need for performing local flux linkage-current differentiation to calculate the magnetization inductance. This reduces the model computational burden.

The exciter model output is represented in the  $dq$ -axes reference frame. In order to connect it to the three phase diode rectifier, the model output has to be converted from the  $dq$  to the  $abc$  reference frame. This transformation is implemented by the circuit shown in Fig. 5.12. The exciter output is connected to two controlled voltage sources, and the rectifier input is implemented with three controlled current sources [59].

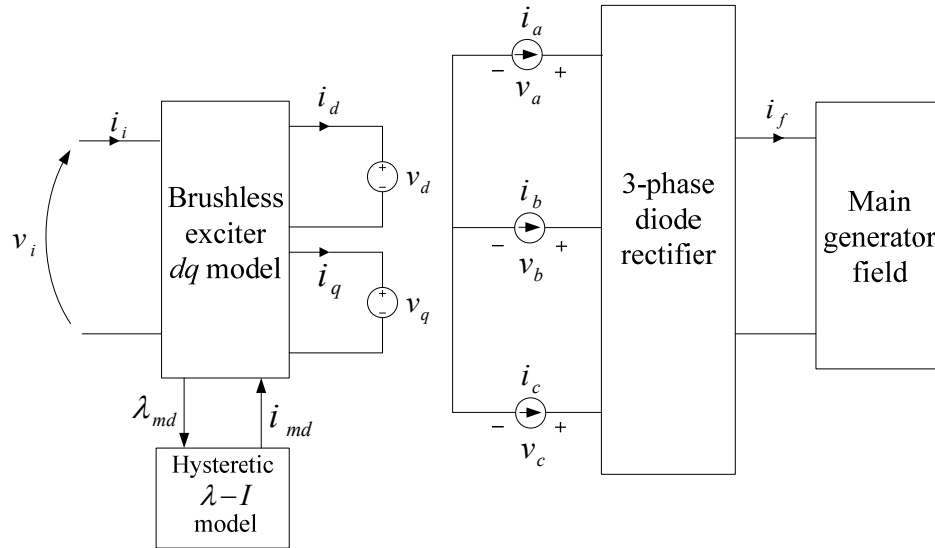


Fig. 5.12 Implementation of the brushless exciter model

The measured currents in the  $dq$  reference frame induce respective currents in the  $abc$  reference frame through the  $dq$  to  $abc$  transformation matrix ( $K^{-1}$ ) by,

$$\begin{bmatrix} i_a \\ i_b \\ i_c \end{bmatrix} = K^{-1} \begin{bmatrix} i_q \\ i_d \end{bmatrix} \quad (5.14)$$

Where,

$$K^{-1} = \begin{bmatrix} \cos(\theta_r) & \sin(\theta_r) \\ \cos(\theta_r - \frac{2\pi}{3}) & \sin(\theta_r - \frac{2\pi}{3}) \\ \cos(\theta_r + \frac{2\pi}{3}) & \sin(\theta_r + \frac{2\pi}{3}) \end{bmatrix} \quad (5.15)$$

Similarly, the measured voltages in the  $abc$  reference frame induce respective voltages in the exciter  $dq$  model output through,

$$\begin{bmatrix} v_q \\ v_d \end{bmatrix} = K \begin{bmatrix} v_a \\ v_b \\ v_c \end{bmatrix} \quad (5.16)$$

Where,

$$K = \frac{2}{3} \begin{bmatrix} \cos(\theta_r) & \cos(\theta_r - \frac{2\pi}{3}) & \cos(\theta_r + \frac{2\pi}{3}) \\ \sin(\theta_r) & \sin(\theta_r - \frac{2\pi}{3}) & \sin(\theta_r + \frac{2\pi}{3}) \end{bmatrix} \quad (5.17)$$

The rotor position  $\theta_r$  is calculated from the rotor speed  $\omega_r$  by,

$$\theta_r = \int \omega_r dt \quad (5.18)$$

The rectifier load is represented by the impedance of the main generator field winding.

The generator field current is then used as an input to the synchronous generator model.

## 5.6 Measurements of the Exciter Parameters

The brushless exciter parameters of a synchronous generator system are obtained through measurements performed at standstill. The main synchronous generator has four poles and rated at 13 kVA, while the brushless exciter is an 8-pole machine.

### 1) Resistances

The armature and field winding resistances can be directly measured at the exciter terminals using the four-wire method. The resistances are measured at room temperature, and the effect of temperature variation is not included in the model.

### 2) Turns-ratio

The exciter turns-ratio is calculated by the method described in [58]. The armature MMF is first aligned with the exciter field winding by applying DC current through the armature  $b$  and  $c$  terminals with phase  $a$  is left open. When a DC current is applied to the field winding, the rotor MMF aligns with the field MMF in the  $d$ -axis. The rotor is then locked at this position, and the  $d$ -axis magnetization flux linkage-current loops are first measured from the stator side by exciting the field terminals with an AC source and measuring the induced voltage across the armature  $b$  and  $c$  terminals. The same measurements are then performed from the rotor side by exciting the armature  $b$  and  $c$  terminals, and measuring the induced voltage across the field winding. For each set of measurements, the applied current and the induced voltage are used to construct the magnetization flux linkage-current loops. Each experiment has one parameter that can be measured directly and one parameter that depends on the exciter turns-ratio. The flux

linkage-current loops measured from the stator and rotor sides are compared and the turns-ratio is adjusted until the measured loops from both sides coincide. Fig. 5.13 compares the magnetization flux linkage-current loops measured from the stator and rotor sides when a turns-ratio of 0.02 is used.

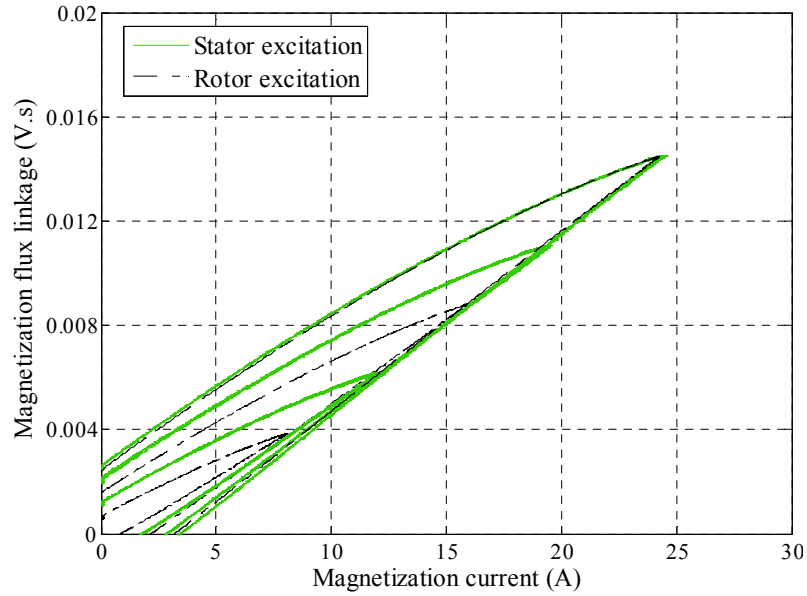


Fig. 5.13 Comparison of the flux linkage - current loops measured from the stator and rotor sides with a turns-ratio of 0.02

### 3) *d-q model inductances*

From the previous set of measurements, the static *d*-axis magnetization inductance ( $L_{md}$ ) can be calculated from the stator side excitation by,

$$L_{md} = \frac{\sqrt{3}}{2} \frac{\lambda_{bc}}{TR \times I_f} \quad (5.19)$$

The same measurements can also be performed from the rotor side by,

$$L_{md} = \frac{2}{\sqrt{3}} \frac{TR \times \lambda_f}{I_{bc}} \quad (5.20)$$

When the exciter armature is excited and the field circuit is left open, the measured input impedance ( $Z_i$ ) can be represented by,

$$Z_i = \frac{V_i}{I_i} = 2[R_a + j\omega(L_{la} + L_{md})] \quad (5.21)$$

The armature leakage inductance ( $L_{la}$ ) can then be obtained from,

$$L_{la} = \frac{\sqrt{\frac{|Z_i|^2}{4} - R_a^2}}{\omega} - L_{md} \quad (5.22)$$

Similarly, the field leakage inductance ( $L_{lf}$ ) can be obtained from the field side measurements with the armature circuit left open by,

$$L_{lf} = \frac{\sqrt{|Z_i|^2 - R_f^2}}{\omega} - L'_{md} \quad (5.23)$$

Where  $L'_{md}$  is the  $d$ -axis magnetization inductance referred to the field side through the turns ratio. The measurements of the  $q$ -axis parameters can be performed while the rotor is locked at the same position by connecting  $b$  and  $c$  terminals and applying an AC voltage across terminal  $a$  and the joint  $b$  and  $c$  connection. The armature MMF generated with this configuration is aligned with the field  $q$ -axis [60]. When the armature circuit is excited and the field terminals are left open, the input impedance can be calculated by,

$$Z_i = \frac{V_i}{I_i} = \frac{3}{2}[R_a + j\omega(L_{la} + L_{mq})] \quad (5.24)$$

The  $q$ -axis magnetization inductance ( $L_{mq}$ ) can then be obtained from,

$$L_{mq} = \frac{\sqrt{\left(\frac{2|Z_i|}{3}\right)^2 - R_a^2}}{\omega} - L_{la} \quad (5.25)$$

The measured parameters for the brushless exciter machine are listed in table 5.1.

Table 5.1 Measured exciter parameters

$R_a$ ( $\Omega$ )	0.06
$R_f$ ( $\Omega$ )	17.5
$L_{la}$ (mH)	0.0858
$L_{lf}$ (mH)	220
$L_{md}$ (mH)	0.557
$L_{mq}$ (mH)	0.433

#### 4) Hysteretic model parameters

The hysteretic model parameters  $L_a$ ,  $K_H$  and  $K_B$  are obtained from the measured  $d$ -axis magnetization flux linkage-current loops by the method described in section 5.4. The magnetization flux linkage-current loops of the exciter are then reconstructed with the Energetic model using equation (5.3). Fig. 5.14 compares the measured and simulated loops. It is clear that the developed model can simulate the hysteretic magnetization characteristics well, while only utilizing a few measured parameters.

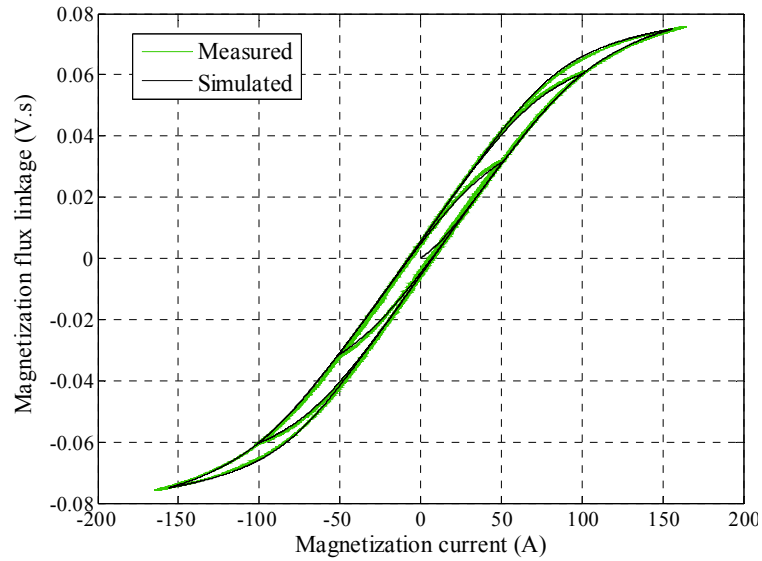


Fig. 5.14 Comparison of the measured and simulated flux linkage -current loops

## 5.7 Experimental Validation

In order to verify the validity of the developed model, transient measurements are performed on the 13 kVA brushless excited synchronous generator. The generator is driven to synchronous speed by a shunt DC motor. A step change in the excitation voltage is then applied to the brushless exciter field winding through a linear amplifier. The exciter field current and main generator output voltage are measured and compared to the simulated results with the developed model.

Figs. 5.15 and 5.16 show the measured and simulated field current during transient. The ripples in the exciter field current are attributed to the commutation of the rectifier diodes. However, these switching ripples do not appear in the generator output voltage as they are filtered by the large inductance of the main generator field winding.

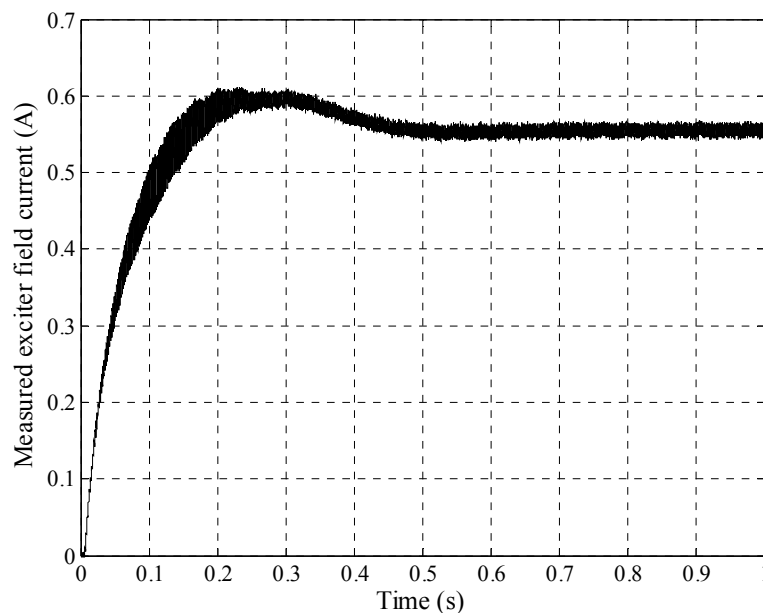


Fig. 5.15 Measured exciter field current after a step change in the excitation voltage

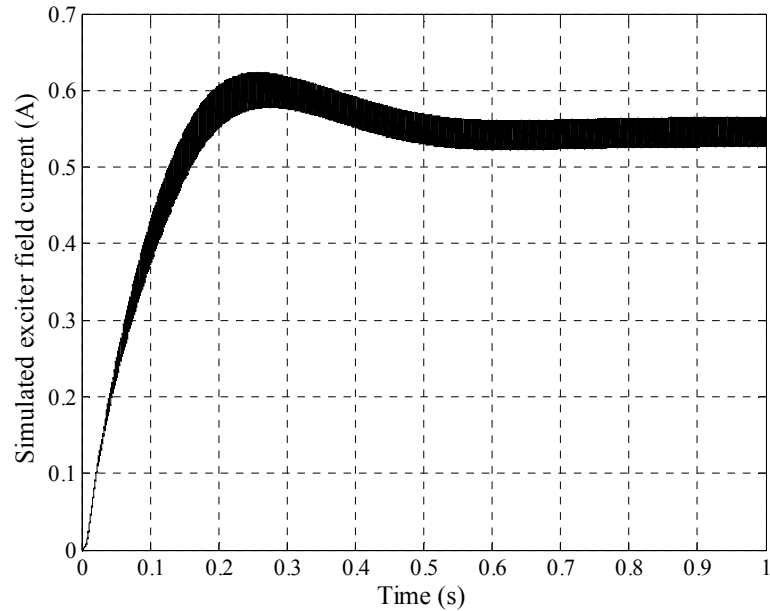


Fig. 5.16 Simulated exciter field current after a step change in the excitation voltage

The measured and simulated generator output voltages during transient are shown in Fig. 5.17. It is clear that the hysteretic system model is able to predict the generator voltage variation during transient. On the other hand, the simulated voltage using a constant  $d$ -axis magnetization inductance deviates from the measurements when the generator voltage begins to decrease, as the model cannot capture the variation of the magnetization inductance after the flux reversal. Fig. 5.18 shows the simulated magnetization flux linkage-current plot during transient. As the magnetization current decreases after reaching its peak value, the flux linkage follows different trajectory from the ascending branch. The corresponding inductance variation cannot be simulated with a static magnetization inductance model, and it requires incorporating the hysteretic characteristics of the brushless exciter machine. In addition, the hysteretic system model requires 131 sec for simulation, which is only 10% more than the simulation time required for the constant inductance model.

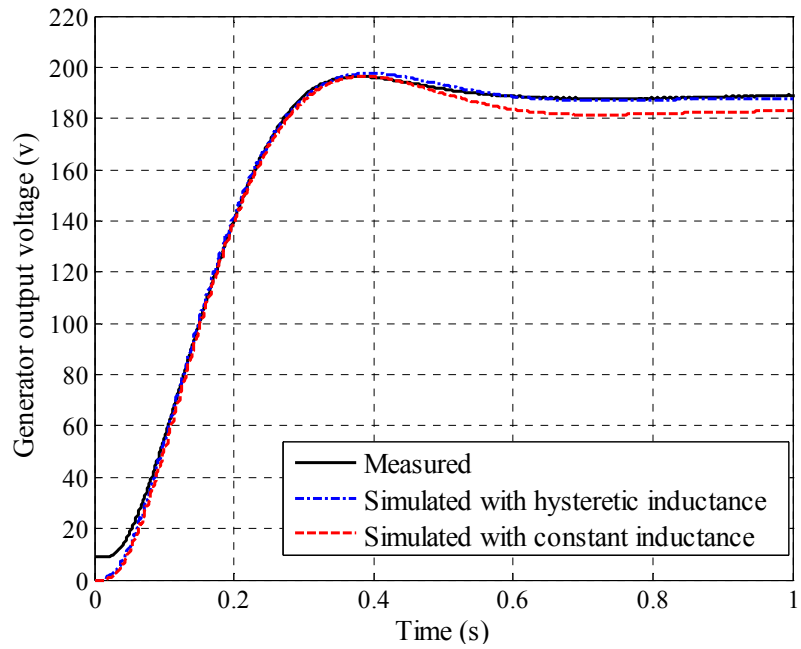


Fig. 5.17 Comparison of the measured and simulated generator output voltage after a step change in the excitation voltage

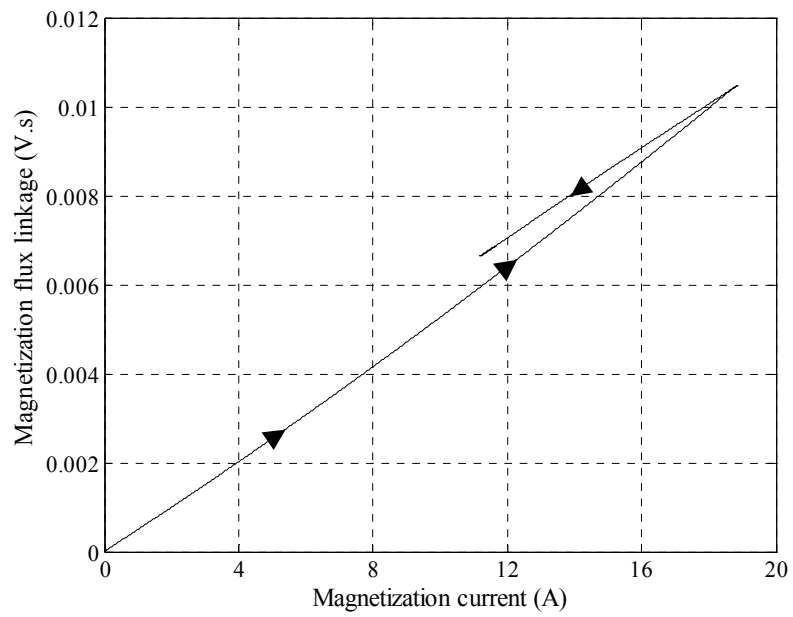


Fig. 5.18 Simulated flux linkage-current trajectory during transient

## 5.8 Summary

A model is developed to simulate the magnetization flux linkage-current loops in electric machines using the Energetic model. The developed model only requires few parameters from the measurements, and can achieve computationally efficient hysteresis simulation. The hysteretic model is then incorporated into the brushless exciter model of a synchronous generator system. The model results are then verified experimentally with transient measurements on a brushless excited synchronous generator. The comparison between measured and simulated results shows that accurate prediction of the system transient response requires considering the hysteretic characteristics of the brushless exciter machine.

## 6. CONCLUSIONS AND RECOMMENDATIONS

### 6.1 Conclusions

#### Variable Flux Machine Design

- It is essential for electric vehicle industry to find alternative technologies to rare-earth PMSMs, as there is a possibility of uneconomical magnet prices in the future.
- An Alnico permanent machine can theoretically provide a torque density comparable to a rare-earth PMSM, and it can achieve high efficiency at a wide speed range, as the flux weakening can be performed by armature current pulses that dissipate negligible losses.
- A tangentially magnetized design for variable flux machines with Alnico magnets is developed. The proposed design can provide high air gap flux densities at no-load, and the applied armature current at full load tends to stabilize the magnet operating point.
- The demagnetization and magnetization characteristics of the machine are analyzed using hysteresis dependent FEA simulations. The results show that the magnet flux can be controlled by armature current pulses. However, the required current to magnetize the magnets is larger than the machine rated current, which may lead to oversizing the machine converter.
- The effect of different machine design parameters on the magnetization current as well as the machine performance are evaluated and the following design considerations are proposed for the magnetization current reduction,

- The magnetization current can be reduced by using integral stator windings with low number of stator slots per pole. However, these machines have large torque ripple. Therefore, they are not suitable for applications that require smooth output torque.
  - Skewing is an effective method for reducing the torque ripple, but it is not preferable for variable flux machines with low coercive field magnets, as it may cause irreversible magnet demagnetization in part of the machine axial length.
  - Variable flux machines with fractional windings can achieve low torque ripple and low magnetization current compared to the integral winding designs.
  - For reduced magnetization current, the steel saturation has to be limited by using high slot fill factor and optimizing the ratio between the stator tooth and yoke width.
  - The required magnetization current can be effectively controlled by changing the length of the rotor magnets.
  - The issue of oversizing the inverter is less likely to be found in variable flux machines with improved cooling techniques.
- The Efficiency maps of the designed machine are simulated for different magnetization levels. It is found that reducing the magnet flux at high speeds can lead to huge energy savings, especially at the low torque region. This can be utilized in the traction motor of electric vehicles, which operates for long periods at high speeds and low torque conditions.

- A prototype of the designed machine is manufactured, and the experimental results confirm the validity of the proposed machine design concept.

### **Hysteresis Loss Prediction**

- The optimization of modern electrical machines requires having a model that can accurately predict the machine hysteresis losses under distorted flux waveforms.
- Experimental hysteresis loss measurements are performed on electrical steels exposed to various flux waveforms.
- The analytical models for hysteresis loss calculations can only predict minor loop hysteresis losses under certain conditions, but they cannot be relied on to predict the hysteresis losses under a large variety of possible encountered flux waveforms in electrical machines.
- A hybrid model is developed to achieve accurate and computationally efficient hysteresis loss calculation. The model utilizes the modified Steinmetz equation to calculate the symmetric loop hysteresis losses, and it utilizes the Energetic hysteresis model for the calculation of hysteresis losses under minor loops and unsymmetrical flux waveforms.
- The hybrid model is then applied to calculate the hysteresis losses of a switched reluctance machine. The results show that having a model that is capable of calculating the hysteresis losses under a variety of flux waveforms is essential for precise machine core loss prediction.

## Brushless Exciter Modeling

- The steel hysteresis characteristics of the brushless exciter of synchronous generators are found to be responsible for the deviation between the measured generator transient response and the simulated results with the conventional  $dq$ -axes model.
- A hysteretic model is developed to integrate the machine flux linkage-current characteristics into the  $dq$ -axes model of the brushless exciter. The developed model requires few measured parameters, and can achieve computationally efficient hysteresis simulation by utilizing the Energetic hysteresis model for the steel  $B-H$  loop modeling.
- The developed model is then used to predict the transient response of a 10 kVA brushless excited synchronous generator. The measured generator transient response agrees well with the model simulation results, confirming the validity of the proposed model.

## 6.2 Proposed Future Research

- Improvements in the performance and magnetization requirements of the proposed Alnico variable flux machine can be achieved by using GA (Genetic Algorithm) based optimization techniques.
- An Alnico variable flux machine should be designed for an actual electric vehicle traction drive. Such a machine can be designed so that the magnetization current

is lower than the machine rated current, as the improved machine cooling can allow the stator windings to operate with higher current densities.

- Intensive research work has to be done on the drive of variable flux machines in order to develop a reliable control technique for magnetizing and demagnetizing the magnets under different operating conditions.
- An efficient dynamic hysteresis model should be developed to include the steel lamination eddy current losses into the simulated static hysteresis loops. Not only this model can provide improved machine core loss prediction, but it can also allow the machine FEA simulations to be performed using the actual steel hysteresis characteristics, which are varying with the machine speed.

### **6.3 Contributions**

The followings are the technical output of the presented research work in this thesis:

#### **Journal Papers**

1. M. Ibrahim and P. Pillay, "Core Loss Prediction in Electrical Machine Laminations Considering Skin Effect and Minor Hysteresis Loops," *IEEE Transactions on Industry Applications*, vol.49, no.5, pp. 2061 - 2068, Sept.-Oct. 2013.
2. M. Ibrahim and P. Pillay, "A Hybrid Model for Improved Hysteresis Loss Prediction in Electrical Machines," *IEEE Transactions on Industry Applications*, vol.50, no.4, pp. 2503 - 2511, July-Aug. 2014.
3. M. Ibrahim and P. Pillay, "Hysteresis Dependent Model for the Brushless Exciter of Synchronous Generators," in the second round of the review process, *IEEE Transactions on Energy Conversion*.

4. M. Ibrahim and P. Pillay, "Design of High Torque Density Variable Flux Permanent Magnet Machine Using Alnico Magnets," submitted to *IEEE Transactions on Industry Applications*.
5. M. Ibrahim and P. Pillay, "Design of Variable Flux Permanent Magnet Machine for Reduced Inverter Rating," submitted to *IEEE Transactions on Industry Applications*.

### **Conference Papers**

1. M. Ibrahim and P. Pillay, "Core Loss Prediction in Electrical Machine Laminations Considering Skin Effect and Minor Hysteresis Loops," Energy Conversion Congress and Exposition conference (ECCE), Raleigh, North Carolina, USA, Sept. 2012.
2. M. Ibrahim and P. Pillay, "A Hybrid Model for Improved Hysteresis Loss Prediction in Electrical Machines," Energy Conversion Congress and Exposition (ECCE), Denver, Colorado, USA, Sept. 2013.
3. M. Ibrahim and P. Pillay, "Modeling of Hysteresis Dependent Magnetization Inductance for a Brushless Exciter Model," Electric Machines and Drives Conference (IEMDC), Chicago, Illinois, USA, May 2013.
4. M. Ibrahim and P. Pillay, "Design of Variable Flux Permanent Magnet Machine for Reduced Inverter Rating," International Conference on Electrical Machines (ICEM), Berlin, Germany, Sept. 2014.
5. M. Ibrahim and P. Pillay, "Design of High Torque Density Variable Flux Permanent Magnet Machine Using Alnico Magnets," Energy Conversion Congress and Exposition conference (ECCE), Pittsburg, Pennsylvania, USA, Sept. 2014.

## REFERENCES

- [1] M. Olszewski, "Final report on assessment of motor technologies for traction drives of hybrid and electric vehicles", A Report submitted to Energy Efficiency and Renewable Energy Vehicle Technologies Program, Mar. 2011.
- [2] S. Taghavi and P. Pillay, "A Sizing Methodology of the Synchronous Reluctance Motor for Traction Applications," *IEEE Journal of Emerging and Selected Topics in Power Electronics*, vol.2, no.2, pp. 329-340, June 2014.
- [3] I. Boldea, L.N. Tutelea, L. Parsa and D. Dorrell, "Automotive Electric Propulsion Systems With Reduced or No Permanent Magnets: An Overview," *IEEE Transactions on Industrial Electronics*, vol.61, no.10, pp. 5696-5711, Oct. 2014.
- [4] A. Vagati, A. Fratta, G. Franceschini and P. Rosso, "AC motors for high-performance drives: a design-based comparison," *IEEE Transactions on Industry Applications*, vol.32, no.5, pp. 1211-1219, Sep/Oct 1996.
- [5] T. A. Lipo, "Synchronous reluctance machines: A viable alternative for A.C. drives," *Electric Machines and Power Systems*, pp. 659-671, 1991.
- [6] M.R. Harris and Miller, T.J.E., "Comparison of design and performance parameters in switched reluctance and induction motors," *Fourth International Conference on Electrical Machines and Drives (ICEM)*, pp. 303-307, 13-15 Sep. 1989.
- [7] F. Sahin, H. B. Ertan, and K. Leblebicioglu, "Optimum geometry for torque ripple minimization of switched reluctance motors," *IEEE Transactions on Energy Conversion*, vol. 15, no. 1, pp. 30-39, Mar. 2000.
- [8] Z. Tang, P. Pillay, Y. Chen and A.M. Omekanda, "Prediction of electromagnetic forces and vibrations in SRMs operating at steady-state and transient speeds," *IEEE Transactions on Industry Applications*, vol.41, no.4, pp.927-934, July-Aug. 2005.
- [9] R. Mikail, I. Husain, Y. Sozer, M.S. Islam and T. Sebastian, "Torque-Ripple Minimization of Switched Reluctance Machines Through Current Profiling," *IEEE Transactions on Industry Applications*, vol.49, no.3, pp.1258-1267, May-June 2013.
- [10] A. Vagati, B. Boazzo, P. Guglielmi, G. Pellegrino, "Design of Ferrite-Assisted Synchronous Reluctance Machines Robust Toward Demagnetization," *IEEE Transactions on Industry Applications*, vol.50, no.3, pp.1768-1779, May-June 2014.
- [11] M. Barcaro, N. Bianchi, F. Magnussen, "Permanent-Magnet Optimization in Permanent-Magnet-Assisted Synchronous Reluctance Motor for a Wide Constant-Power Speed Range," *IEEE Transactions on Industrial Electronics*, vol.59, no.6, pp.2495-2502, June 2012.

- [12] M. Barcaro, N. Bianchi, "Interior PM machines using Ferrite to substitute rare-earth surface PM machines," *International Conference on Electrical Machines (ICEM)*, pp.1339-1345, Sep. 2012.
- [13] D. G. Dorrell, M. Hsieh and A. M. Knight, "Alternative Rotor Designs for High Performance Brushless Permanent Magnet Machines for Hybrid Electric Vehicles," *IEEE Transactions on Magnetics*, vol.48, no.2, pp.835-838, Feb. 2012.
- [14] M. R. Mohammad, K. Kim and J. Hur, "Design and Analysis of a Spoke Type Motor With Segmented Pushing Permanent Magnet for Concentrating Air-Gap Flux Density," *IEEE Transactions on Magnetics*, vol.49, no.5, pp.2397-2400, May 2013.
- [15] H. Kim, K. Kim, Y. Jo and J. Hur, "Optimization Methods of Torque Density for Developing the Neodymium Free SPOKE-Type BLDC Motor," *IEEE Transactions on Magnetics*, vol.49, no.5, pp.2173-2176, May 2013.
- [16] G. A. McCo et al, "Energy-efficient electric motor selection handbook," Revision 3, Jan. 1993.
- [17] B. D. Cullity and C. D. Graham, "Introduction to magnetic materials," 2nd ed. John Wiley & Sons, 2009.
- [18] M.L. Hodgdon, "Mathematical theory and calculations of magnetic hysteresis curves", *IEEE Transactions on Magnetics*, vol. 24, no. 6, pp. 3120-3122, Nov 1988.
- [19] F. Preisach, "Uber die magnetische nachwirkung," *Zeitschrift fur Physik*, vol. B 94, pp. 277-302, 1935.
- [20] I. D. Mayergoyz, "Mathematical models of hysteresis," New York: Springer-Verlag, 1991.
- [21] D.C Jiles and D.L. Atherton, "Theory of ferromagnetic hysteresis," *Journal of Applied Physics* , vol. 55, no. 6, pp. 2115-2120, Mar 1984.
- [22] H. Hauser, "Energetic model of ferromagnetic hysteresis: Isotropic magnetization," *Journal of Applied Physics*, vol.96, no.5, pp.2753-2767, Sep 2004.
- [23] E. Barbisio, F. Fiorillo, and C. Ragusa "Predicting loss in magnetic steels under arbitrary induction waveform and with minor hysteresis loops," *IEEE Transactions on Magnetics*, vol.40, no.4, pp.1810-1819, July 2004.
- [24] V. Ostovic, "Memory motors," *IEEE Industry Applications Magazine*, vol.9, no.1, pp.52,61, Jan/Feb 2003.
- [25] H. Liu, H. Lin, F. Shuhua and X. Huang, "Investigation of influence of permanent magnet shape on field-control parameters of variable flux memory motor with FEM," *Proceedings of the Automation Congress Conference*, Sept. 2008.

- [26] C.Yiguang, P. Wei, et al., "Interior composite-rotor controllable-flux PMSM - memory motor," *Proceedings of the International Conference on Electrical Machines and Systems (ICEMS)*, pp. 446-449, Sept. 2005.
- [27] K. Sakai, K.; K. Yuki, K., et al., "Principle of the variable-magnetic-force memory motor," *Proceedings of the International Conference on Electrical Machines and Systems (ICEMS)*, pp.1-6, Nov. 2009.
- [28] Z. Changqing, W. Xiuhe and W. Bei, "Study of a novel permanent magnet synchronous motor with composite-rotor," *Proceedings of the International Conference on Electrical Machines and Systems (ICEMS)*, pp.1044-1047, Oct. 2010.
- [29] G. Zhou, T. Miyazaki, et al. "Development of variable magnetic flux motor suitable for electric vehicle," *Proceedings of the International Power Electronics Conference (IPEC)*, pp. 2171-2174, Jun. 2010.
- [30] N. Limsuwan, T. Kato, K. Akatsu and R.D. Lorenz, "Design and Evaluation of a Variable-Flux Flux-Intensifying Interior Permanent-Magnet Machine," *IEEE Transactions on Industry Applications*, vol.50, no.2, pp.1015-1024, March-April 2014.
- [31] H.C. Lai and D. Rodger, "Modelling rotor skew in induction machines using 2D and 3D finite element schemes," *Proceedings of IEEE International Electric Machines and Drives Conference (IEMDC)*, May 1997.
- [32] J. Hendershot and T. Miller, "Design of brushless permanent magnet machines," 2nd ed. Motor Design Books, 2010.
- [33] N. Limsuwan, T. Kato, K. Akatsu and R. D. Lorenz, "Design methodology for variable-flux, flux-intensifying interior permanent magnet machines for an electric-vehicle-class inverter rating," *Proceedings of Energy Conversion Congress and Exposition conference (ECCE)*, pp.1547-1554, 15-19 Sept. 2013.
- [34] H. Kyu-Yun, S. Rhee, Y. Byoung-Yull and B. Kwon, "Rotor Pole Design in Spoke-Type Brushless DC Motor by Response Surface Method," *IEEE Transactions on Magnetics*, vol.43, no.4, pp.1833-1836, Apr. 2007.
- [35] P. Zheng, Y. Liu, T. Wang and S. Cheng, "Pole optimization of brushless DC motor," *Proceedings of Industry Applications Conference (IAS)*, pp. 1062-1067, 3-7 Oct. 2004.
- [36] K. Y. Hwang, J. H. Jo and B. I. Kwon, "A Study on Optimal Pole Design of Spoke-Type IPMSM With Concentrated Winding for Reducing the Torque Ripple by Experiment Design Method," *IEEE Transactions on Magnetics*, vol.45, no.10, pp. 4712-4715, Oct. 2009.
- [37] E.C. Lovelace, T.M. Jahns, T.M., T.A. Keim and H. Lang, "Mechanical design considerations for conventionally laminated, high-speed, interior PM synchronous machine rotors," *IEEE Transactions on Industry Applications*, vol.40, no.3, pp.806,812, May-June 2004.

- [38] Z. Han, H. Yang and Y. Chen, "Investigation of the rotor mechanical stresses of various interior permanent magnet motors," *International Conference on Electrical Machines and Systems (ICEMS)*, 15-18 Nov. 2009.
- [39] J. Jung, B. Lee, et al., "Mechanical Stress Reduction of Rotor Core of Interior Permanent Magnet Synchronous Motor," *IEEE Transactions on Magnetics*, vol.48, no.2, pp.911-914, Feb. 2012.
- [40] Z. Gmyrek, A. Boglietti, A. Cavagnino, "Iron Loss Prediction with PWM Supply Using Low- and High-Frequency Measurements: Analysis and Results Comparison," *IEEE Transactions on Industrial Electronics*, vol.55, no.4, pp.1722-1728, Apr. 2008.
- [41] T. Nakata, Y. Ishihara, and M. Nakano, "Iron losses of silicon steel core produced by distorted flux," *Electrical Engineering in Japan*, vol. 90, pp. 10–20, 1970.
- [42] J. D. Lavers, P. P. Biringer, and H. Hollitscher, "A simple method of estimating the minor loop hysteresis loss in thin laminations," *IEEE Transactions on Magnetics*, vol. 14, pp. 386–388, Sept. 1978.
- [43] P. Rupanagunta, J. S. Hsu, and W. F. Weldon, "Determination of iron core losses under influence of third-harmonic flux component," *IEEE Transactions on Magnetics*, vol. 27, pp. 768–777, Mar. 1991.
- [44] C. Cho, D. Son, and Y. Cho, "Core loss analysis of nonoriented electrical steel under magnetic induction including higher harmonics," *Journal of Magnetics*, vol. 6, p. 66, 2001.
- [45] S.D. Calverley, G.W. Jewell and R.J. Saunders, "Prediction and Measurement of Core Losses in a High-Speed Switched-Reluctance Machine," *IEEE Transactions on Magnetics*, Vol. 41 , pp. 4288 – 4298, Nov. 2005.
- [46] Y. Chen and P. Pillay, "An improved formula for lamination core loss calculations in machines operating with high frequency and high flu density excitation," *proceedings of IEEE 37th IAS Annual Meeting*, vol. 2, pp. 759– 766, 13-18 Oct 2002.
- [47] M. Ibrahim and P. Pillay, "Advanced Testing and Modeling of Magnetic Materials Including a New Method of Core Loss Separation for Electrical Machines," *IEEE Transactions on Industry Applications*, vol.48, no.5, pp.1507,1515, Sept.-Oct. 2012.
- [48] Y. Zhang, M. Cheng, P.Pillay and B. Helenbrook, "High order finite element model for core loss assessment in a hysteresis magnetic lamination," *Journal of Applied Physics*, vol.106, no.4, pp. 043911-043911-7, Aug 2009.
- [49] Y. Hayashi and T. J. E. Miller, "A new approach to calculating core losses in the SRM," *IEEE Transactions on Industry Applications*, vol. 31, no. 5, pp. 1039–1046, Sep./Oct. 1995.
- [50] P. Materu and R. Krishnan, "Estimation of switched reluctance motor losses," *IEEE Transactions on Industry Applications*, vol.28, no.3, pp.668-679, May/Jun 1992.

- [51] J. Faiz and M. B. B. Sharafin, “Core losses estimation in a multiple teeth per stator pole switched reluctance motor”, *IEEE Transactions on Magnetics*, vol. 30, no. 2, pp. 189–195, Mar. 1994.
- [52] T. L. Mthombeni and P. Pillay, “Lamination core losses in motors with nonsinusoidal excitation with particular reference to PWM and SRM excitation waveforms”, *IEEE Transactions on Energy Conversion*, vol. 20, pp. 836 – 843, Dec. 2005.
- [53] T. Zouaghi, M. Maguiraga and M. Poloujadoff, “Brushless Exciter Dynamic Model Including Saturation and Multiple Commutation Overlapping Effects”, *proceeding of the Fifth International Conference on Electrical Machines and Systems (ICEMS)*, pp. 444 – 447, 2001.
- [54] Recommended Practice for Excitation System Models for Power System Stability Studies, *IEEE Standard 421.5*, Mar. 1992.
- [55] M. A. Abdel-Halim and C. D. Manning, “Modeling a laminated brushless exciter-alternator unit in all modes of operation,” *IEE Proceedings on Electric Power Applications*, vol.138, no.2, pp.87-94, Mar 1991.
- [56] S. M. L. Kabir and R. Shuttleworth, “Brushless exciter model,” *IEE Proceedings on Generation, Transmission and Distribution*, vol.141, no.1, pp.61-67, Jan 1994.
- [57] D. C. Aliprantis, S. D. Sudhoff, and B. T. Kuhn, “A brushless exciter model incorporating multiple rectifier modes and Preisach’s hysteresis theory,” *IEEE Transactions on Energy Conversion*, Vol. 21, pp. 136-147, Mar 2006.
- [58] D. C. Aliprantis, S. D. Sudhoff, and B. T. Kuhn, “Genetic Algorithm-Based Parameter Identification of a Hysteretic Brushless Exciter Model”, *IEEE Transactions on Energy Conversion*, Vol. 21, pp. 148-154, Mar 2006.
- [59] I. Jadric, D. Borojevic, and M. Jadric, “Modeling and control of a synchronous generator with an active dc load,” *IEEE Transactions on Power Electronics*, vol. 15, no. 2, pp. 303-11, March 2000.
- [60] I. Jadric “Modeling and control of a synchronous generator with electronic load,” *M.s. dissertation*, Virginia Polytechnic Institute and State University, Blacksburg, VA, Jan. 1998.